



UNIVERSITÀ DEGLI STUDI DI MILANO
FACOLTÀ DI SCIENZE E TECNOLOGIE

CORSO DI LAUREA MAGISTRALE IN FISICA

**REALIZATION OF AN ACTIVELY STABILIZED
OPTICAL CAVITY FOR THE MARIX PROJECT**

Relatore: Dott. Simone Cialdi

Correlatore: Dott. Gianluca Galzerano

Tesi di Laurea di
Francesco CANELLA
Matr. 902350

ANNO ACCADEMICO 2017 - 2018

Contents

1	Introduction	1
2	Introduction to the MariX project	3
2.1	The MariX project	3
2.1.1	General overview	3
2.1.2	MariX Photonic Machine	6
3	Theoretical concepts: <i>active optical stabilization</i>	15
3.1	Power Spectral Density and noise	15
3.2	General scheme of the feedback	18
3.2.1	Barkhausen stability criterion	21
3.2.2	Pound-Drever-Hall technique	22
3.3	Source: optical cavities	26
3.4	Reference: mode locking laser	30
3.5	Discriminator and Servo: electronic concepts	35
3.5.1	Signal filtering	35
3.5.2	Circuits with operational amplifiers	37
3.6	Actuator: harmonic oscillator model	40
4	Experimental setup	45
4.1	Global layout	45
4.2	Laser source	48
4.2.1	Spectral and temporal properties	48
4.2.2	Laser intensity noise	50
4.2.3	Laser beam features	53
4.3	Optical cavity	54
4.3.1	Cavity modes	55
4.3.2	Cavity alignment and mode-matching procedure	55

4.3.3	Cavity Finesse	60
4.3.4	Spot and Waist dimension	64
5	Feedback system and noise suppression	69
5.1	Feedback characterization	69
5.1.1	Discriminator	69
5.1.2	Servo	72
5.1.3	Actuator	78
5.2	Stabilization procedure	81
5.3	Noise of stabilized cavity-laser system	87
5.4	Low frequency noise measurements	95
6	Conclusions	99
	Bibliography	101

Chapter 1

Introduction

MariX project has the ambition of join together two different X-rays sources, namely a Free Electron Laser and an Inverse Compton Scattering source (named BriXs), with the aim of creating an innovative scientific tool able to go beyond the limits of actual technologies [1]. The possible applications of MariX are very wide and range from the chemistry to biology, from medicine to solid state physics and cultural heritage research [2][3]. Since very high light power is required by Compton scattering, laser pulses will be amplified and sent to a resonant high Finesse Fabry-Perot cavity actively stabilized in order to reach about 500 kW or more. One of the first steps in R&D program is the realization of prototypes of the stabilized optical cavity that will be present in BriXs in order to study and characterize its features and individuate the most important implementation problems. With this objective, we realized a 2D four mirror bow-tie Fabry-Perot cavity and we characterized its most important features. We also characterized the laser source properties and we implemented a feedback able to stabilize the cavity-laser coupled system. Active stabilization has been performed exploiting the so called Pound-Drewe-Hall technique [4]. The study of an actively stabilized system is interesting not also for BriXs cavity stabilization, but also for its great scientific and importance. Indeed, active stabilization is applied in field of great interest as for example frequency comb technology, quantum optics, quantum information and gravitational waves detection [5][6][7].

The first chapter of this work is an introduction to MariX project and its laser part, the so called Photonic Machine. In the second chapter a theoretical introduction will be provided in order to better comprehend the experimental results we reached. The third chapter exposes the experimental setup realized during this work and its detailed characterization, while the fourth chapter is focused on the feedback system, its characterization and mathematical modelization and finally on the stabilization performances experimentally obtained. At the

end of such chapter, very important considerations on next steps to improve MariX optical cavity are exposed.

Chapter 2

Introduction to the MariX project

The purpose of this chapter is to present the main aspects of the MariX project with its so called "Photonic Machine" (the project part concerning lasers and optical cavities) and recall the theoretical concepts necessary to understand the exposed experimental results.

2.1 The MariX project

MariX is the name of a combined radiation source capable of delivering ultra-high flux, coherent, femto second X-rays in a wide range of photon energy (300 eV-180 keV), projected to be installed in the future Scientific Campus of Università degli Studi di Milano, in the now called Milano Innovation District (MIND). The expected time of development is about 5-6 years [1].

2.1.1 General overview

MariX is designed to be a scientific facility with wide range applications and fields of interest. In particular, there is a multitude of research fields involved in MariX project and the most important are: femto-second time resolves linear spectroscopy, nano-object imaging at nano-scale resolution, advanced radiological imaging with multi-color X-rays and innovative radio-therapy techniques based on tunable mono-chromatic hard X-rays. Thanks to its key-features, MariX can be considered as an unique bridge between different generations of radiation sources and we can resume the most important features as:

- Combination of two different radiation sources, a Free Electron Laser and Compton-Back-Scattering and the consequent wide range photon energy spanning from 0.3 keV to 10 keV (FEL) and from 20 keV to 180 keV (Compton). The two main blocks are merged together to form a unique accelerator ensemble.

- Operation in continuous wave mode at high repetition rate, from 1 MHz to 100 MHz.

The general layout of MariX and its logo are shown in Figure 2.1. The first radiation source in MariX is the Free Electron Laser. Despite the great success of Synchrotrons in the last 30 years, the use of a FEL is strategically important to permit experiments intrinsically forbidden by storage rings technology. In particular, two parameters of FEL source are important to go beyond storage rings limits: the brilliance and the coherence of the produced beam. High peak brilliance is important in time-resolved experiments and in studies that require multi-photon processes, while coherence permits to control over the phase of scattering photons, removing some ambiguities typical of normal diffraction experiments. The lasing phenomenon of a FEL allows to have ultra-short pulses, high coherence and high average flux. FEL pulses are of the order of 10-100 fs, about three orders of magnitude lower than synchrotron pulses. In terms of coherence, the FEL performances are 10 to 100 times better than in storage rings and average flux can also be higher, depending on the repetition rate of the Free Electron Laser. Time resolved diffraction, spectroscopy and imaging obtained at MariX would provide new tools in a very wide areas of scientific research such as: chemistry, material science, surface physics, structural biology, quantum materials and more. MariX FEL features could be exploited especially for biologically relevant applications (X-ray spectroscopies and X-ray serial crystallography), thanks to low number of photons for pulse (compared to actual FELs) and working regime at high repetition rate. The accelerator complex of MariX FEL is a two-pass recirculated Linac equipped with a bubble-arc compressor able to re-inject the electron beam leaving the Linac in order to boost it a second time. The bubble-arc compressor is very important in order to reduce the Linac size, without lowering electron energy.

The second X-rays source is Inverse Compton Scattering between electrons and laser photons in a Fabry-Perot optical cavity. In MariX this kind of radiation is produced by a compact machine called BriXS (Bright Compact X-rays Source), that is expected to work in synergy with the Free Electron Laser. As written above, monochromatic X-rays have been proven to be of great interest for medical research, in particular for radiology and radiotherapy, but transfer innovative technologies to everyday users is often hard due to the huge cost of Synchrotron-like facilities. From this point of view, is clear that a compact (laboratory sized) and affordable source, providing a beam with synchrotron-like features, would open the way to a wide range of clinical application and medical/scientific research.

A compact source with performances comparable with synchrotrons in terms of monochromaticity, tunability and intensity does not exist yet and a goal of MariX project is its realization with the development of BriXS. The BriXS performances will be comparable to those of modern synchrotron sources, though its reduced dimensions and costs (from 100x100 m² to 10x10 m² in dimension and hundreds of millions euros to tens of millions euros in

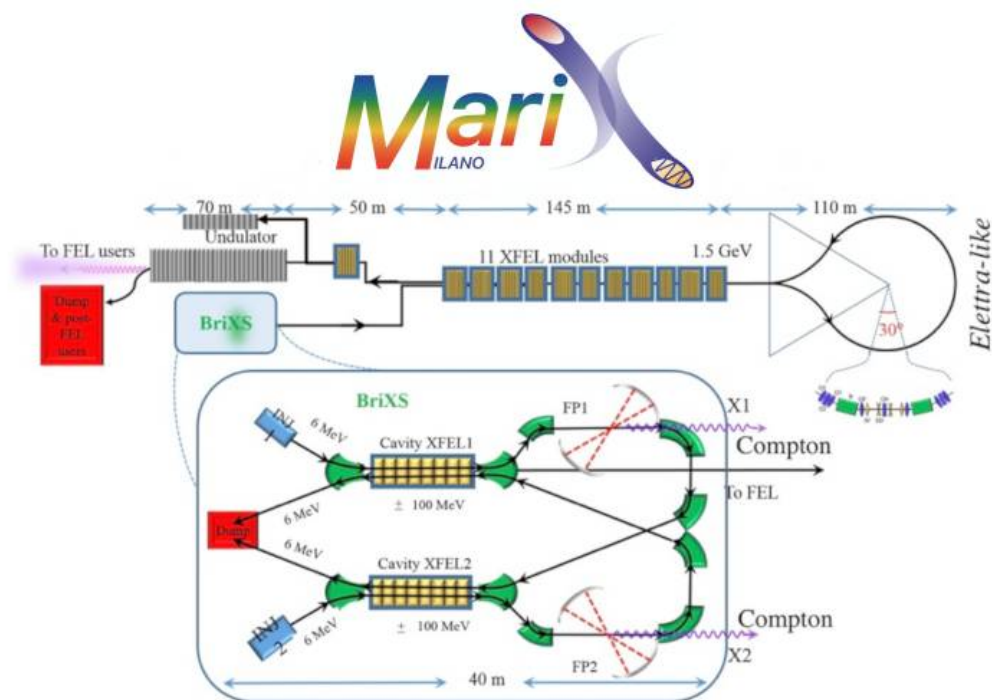


Figure 2.1 MariX layout and logo (picture from [1]).

costs). Such reductions make BriXS available for universities, museums, hospitals and other mid-sized research infrastructures. BriXS will provide an X-ray beam with average energy tunable in the range of 20-180 keV, intensities of $10^{11} - 10^{13}$ photons with a relative energy bandwidth $\Delta E/E = 1 - 10\%$ and good transverse coherence. Another unique feature of BriXS will be the possibility to perform a switch between two colors, then two energies, without changing the working point of the machine. The broad range of applications of BriXS includes K-edge subtraction imaging (particularly important for mammographies), Phase Contrast Imaging, breast cancer rotational radiotherapy, micro-biological studies, crystallography and museology for cultural heritage investigations.

Research and Development program is divided essentially into two main lines: the realization of a ICS-ERL demonstrator and the detailed study of the laser system. In particular, the realization of a demonstrator is fundamental in order demonstrate the theoretical and computational predictions on BriXS properties and feasibility, because many aspects of the project are completely new and never experimentally tested (the modified push-pull layout, as an example). The dedicated test-bench small scale demonstrator will be realized at LASA laboratories with the name BriXSino. The main issues to be addressed by BriXSino are: to reach the requested electron beam quality preserved with and without Energy Recovery Linac, to maintain right stability of RF system, to have the possibility of generating 100 MHz

electron beams, to realize options of two-color ICS generation and to evaluate radio-protection risks related to the beam recovery. The study of the laser system, will be treated in the next section both from the technical point of view and for what concerns the related R&D line.

2.1.2 MariX Photonic Machine

With the term *Photonic Machine* we refer to the MariX optical system, which is designed to drive both the FEL and the Compton sources. The synchronization of the whole system is performed using a single laser oscillator, yielding an advantageous intrinsic synchronization between electron bunches and laser pulses in MariX. In the Inverse Compton Scattering source, the weak Compton cross section requires high photon intensities (on the order of magnitude of hundreds of Watts) in order to obtain the designed X-ray photon flux. The required power can be reached using a pulsed laser instead of a continuous-wave oscillator and injecting its light beam after a preliminary amplification into an high Finesse Fabry Perot (FP) cavity, that by superposing incoming pulses achieves a passive gain of 3-4 orders of magnitude. Moreover, lowering the high repetition rate, it is possible to use the same laser to generate the electrons for the FEL source.

An Yb-fiber mode-locking laser operating at 100 MHz repetition rate on the carrier wavelength 1030 nm has been chosen as laser oscillator for the Photonic Machine. The outgoing radiation is divided in three output lines that deliver different average powers. The first line is dedicated to the Inverse Compton Scattering source, with an average power of 100 mW, the about 100 mW second exit is exploited to produce electron bunches at the RF-guns, while the third output line is used for the Free Electron Laser source. The last output presents characteristics that are different from the other two, because the repetition rate is only 1 MHz (This reduction of a factor of 100 is performed by a Mach-Zender amplitude modulator) and the average power is one order of magnitude higher.

The laser beams coming from the mode-locking oscillator are then amplified in three similar fiber amplifiers stages. After amplifiers the average power is about 200 W for the Fabry-Perot Cavity and RF-guns path, while on the FEL line the power reaches 1 W. The Fabry-Perot cavity consists of four mirror bow-tie cavity stabilized against the laser via Pound-Drever-Hall technique. Here the power raises allowing the scattering between photons and electron bunches. In the photoemission process generating electrons for the RF-guns and the FEL output line, the amplified laser light is converted in the 4th harmonic (so 257.5 nm) via non-linear processes and both temporal and spatial shaped to reach the optimal condition of emittance for the electron bunches.

A key-point for the entire functioning are system stability and synchronization. The laser stabilization network is based on two feedback systems, where the first one stabilizes the laser

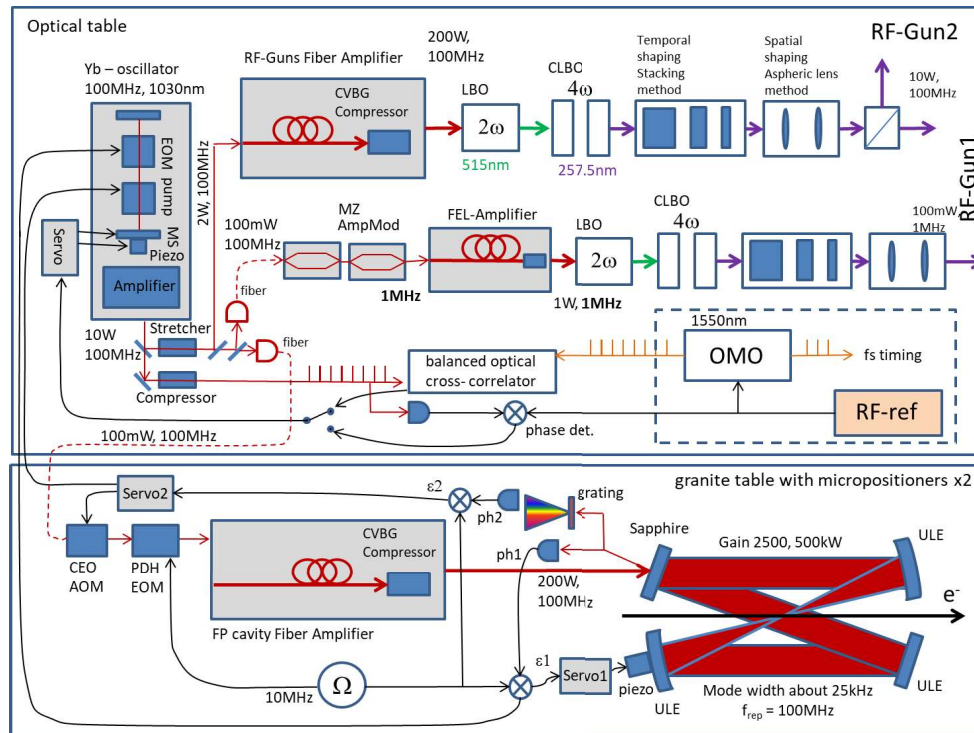


Figure 2.2 MariX Photonic Machine general scheme (picture from [1]).

repetition rate against an external reference while the second system synchronizes the laser and Compton Fabry-Perot cavity against each other. The general scheme of the Photonic Machine is shown in Figure 2.2, while in the following sub-sections the most important components of the MariX Photonic Machine and a summary of the related R&D line will be treated.

Laser oscillator

The laser oscillator must meet some important requirements to achieve the efficient coupling needed in the Fabry-Perot cavity. In fact, the laser beam has to be well coupled to the cavity fundamental mode (TEM_{00}). Another factor to take in account is the necessity of avoiding self-phase modulation effects in the amplification process that lead to amplitude-phase coupling which can disturb the coupling with the optical cavity. These elements establish stringent requirements on the beam spatial profile and degree of polarization, pointing and pulse to pulse stability and finally the possibility to limitate nonlinear optical effects in the amplification stage. The chosen laser is a Yb-fiber mode-locking laser available on the market (produced by Menlo company and One Five company). Such laser operates at 100 MHz repetition rate on the carrier wavelength 1030 nm, with a typical pulse length of

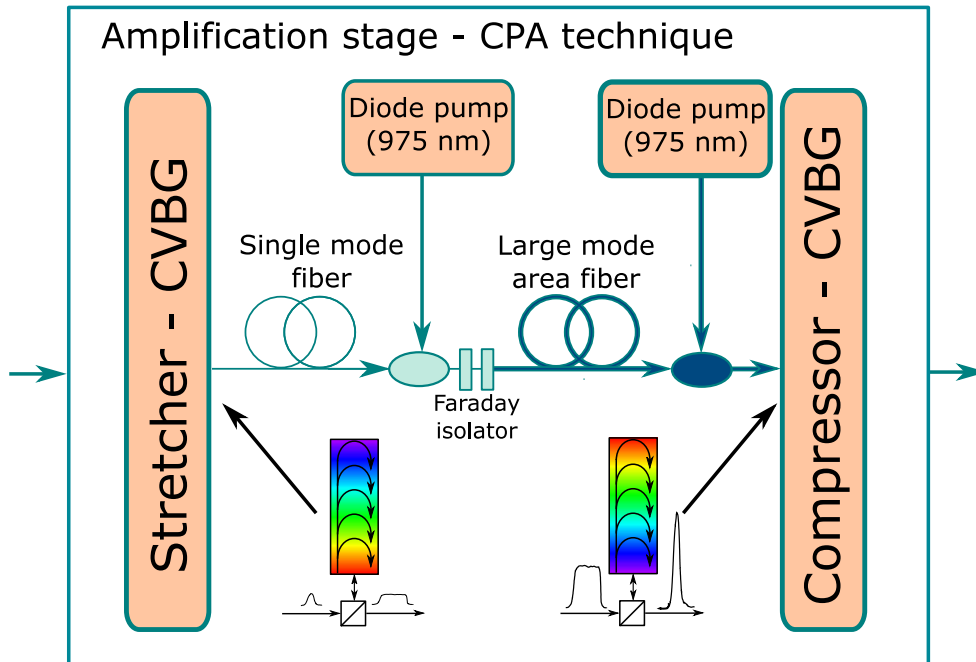


Figure 2.3 Architecture for CPA by means of CVBG and fiber amplification in fibers designed for MariX. Picture taken from [1].

100-200 fs. It is worth to note that the oscillator needs to be controlled in order to stabilize both the repetition rate frequency f_{rep} and the carrier envelope offset f_{CEO} (for more details, see section 3.4), because f_{rep} is fundamental in synchronization of the laser against an external reference, while f_{CEO} has to be removed to overlap laser modes to the FP cavity ones.

Amplification system

The amplifiers will exploit the famous Chirped Pulse Amplification (CPA) method [8] to drastically reduce nonlinear effects during the amplification process and avoiding optical fiber damaging due to the excessive power injected. The signal pulse is initially stretched in time domain up to few hundreds of picoseconds, thus reducing its intensity in the waveguide, where it is amplified, and finally re-compressed. The amplification system is implemented by the use of commercial available Chirped Volume Bragg Gratings - CVBG (for the CPA) and a large mode area double clad Yb-doped fiber (for the amplification) disposed in many stages at increasing power. The whole amplification system has to be designed in order to reach the best compromise between high output power and low noise, given by non-linear effects and amplified spontaneous emission, that is a key-point especially for the beam coupled with the Fabry-Perot cavity. The amplification conceptual scheme is exposed in Figure 2.3, while examples of the amplifier fiber systems and CVBGs are shown in Figure 2.4. The

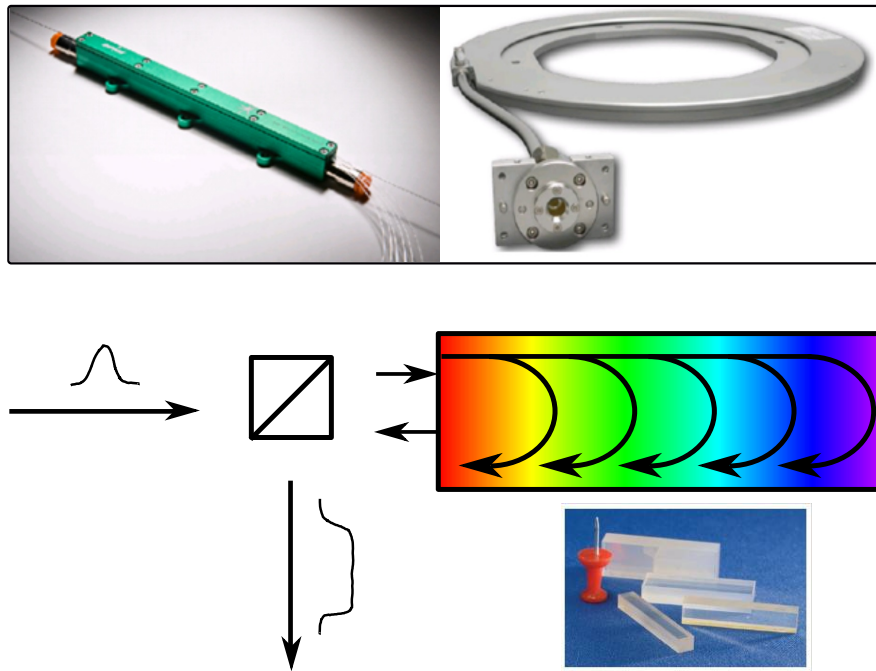


Figure 2.4 *Above*: Two implementable high power amplifier fiber system. On the left, Nfern connectorized coupling system; on the right, NKT's free-space coupling LMA fiber. *Below*: example of a Chirp Volume Bragg Grating. Pictures readapted from [1].

amplification system has to be capable of yielding 200 W at 1030 nm starting from 100 mW. The first stage can be based on a 15 μm core LMA fiber, 5 m long and characterized by 7 dB/m at 975 nm absorption. The reachable output power is 2 W when pump diodes emit 3.3 W. The second stage permits to reach a power of ≈ 60 W using a 40 μm core, 1.8 m long LMA fiber pumped with 100 W. Non-linear effects are reduced by the use of CVBG mirrors that stretch the pulse up to 500 ps. In the last stage the 200 W goal is reached by the use of 1 m long 85 μm rod fibers with a 15dB/m absorbance at 975 nm.

Fabry-Perot cavity (ICS line)

The designed Fabry-Perot cavity for the ICS source is a four mirror (two flat and two curved) a bow-tie cavity in the near confocal configuration. The one that better matches our technical requirement, also thanks to its mechanical stability and good flexibility in adjustments of cavity round trip frequency and of the laser beam waist. In order to obtain an efficient Compton source the aim is maximizing the X-ray flux reaching the best interaction point overlap between laser and electrons. To obtain this the laser spot at the interaction point with electrons should be around the 2σ focal spot size of the electrons bunches. Moreover, the spot size on the mirrors has to be as large as possible in order to reduce thermal effects

related to the high incident powers [9]. The chosen geometric configuration allows to have largest spots at the mirrors and the smaller waist at the focus at the same time when the cavity is in a configuration near the stability edge. The 2D planar nature of the cavity introduces an astigmatism between the horizontal and the vertical axis, then in near-confocal configuration, the spot is elliptical and not circular¹. Obviously, the Finesse of the cavity is a fundamental parameter in our apparatus, because it is strictly related to the power of the resonant radiation, according to:

$$P_{cav} = \frac{2F}{\pi} P_{in}$$

It is evident that the equation above can be satisfied by the combination of large Finesse and low input power and viceversa and find out the best compromise is a key-point in the development of the Compton source. Indeed, working with a very high Finesse cavity involves a very narrow line of cavity modes which on the practical point of view implies a very precise stabilization between the laser and the cavity, without which it is impossible to obtain high power in cavity. On the other hand, a low Finesse lead to the need of amplifier system able of delivering high power with low phase noise.

Many factors has to be take in account to individuate the best configuration. One of the most important is surely how cavity with different Finesse reacts to the mode degeneracy phenomena occurring during the allignement procedure and consequent thermal deformations of mirrors [10]. In this situation the fundamental mode can be degenerate in frequency with a higher order mode, causing additional losses in cavity due to the transfer of a part of the energy to the higher order modes, bigger than the mirror size and unable to resonate. A Finesse and power lowering then occur, but when the mirror shape is replaced, the cycle restarts. Here a low Finesse seems to be advantageous, because in an high Finesse cavity the oscillation are more strong and could not be compensate by the feedback system. On the other hand, an high power third stage of amplification is not particularly advantageous in terms of reliability especially for certain elements like the injector. Currently, the chosen solution is to adopt an amplifier capable of delivering 65 W and a cavity with an intermediate Finesse of about 12000².

4th harmonic generation and beam shaping (RF-guns line)

The laser light for the RF-Guns has to be threatred before reaching the photocatodes and generating electron bunches. In particular, both 4th harmonic generation and tempo-

¹more details on the used optical cavity will be provided in next Chapters

²This value can be compared with the extreme cases of ThomX experiment [11] and Max Planck Insitute [9]. The ThomX cavity is extremely high, about 46000, while the cavity used at Max Plank Institute is lower and it is about 5000

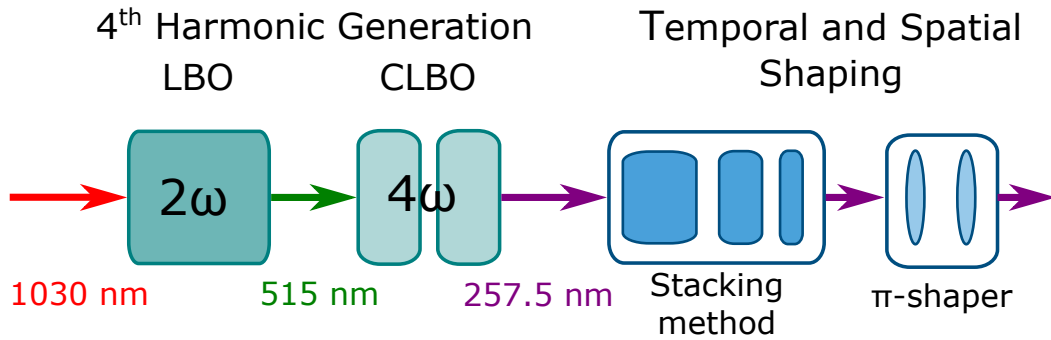


Figure 2.5 Scheme of the 4th harmonic generation and temporal/spatial shaping from [1]. Firstly the beam encounters the nonlinear crystals that generates the 4th harmonic, then the beam is manipulated in order to change its temporal and spatial shape.

ral/spatial shaping have to be performed, as schematized in Figure 2.5. The first stage after amplification is the 4th harmonic generation to obtain suitable photons for the photoemission. This task is experimentally performed using non-linear crystals like Lithium triborate and CLBO. The 4th harmonic at 257.5 nm is generated in two different stages: in the first one Lithium triborate is used to generate the 2nd harmonic from the output of amplifiers, while in the second stage a CLBO crystal generate the 4th harmonic starting from the 2nd. In general, harmonic conversion processes can occur when a laser light goes through a non-linear crystal while the so called phase-matching condition is satisfied. Both the LBO and the CLBO are nonlinear and birefringent crystals, with uniaxial symmetry that can be exploited to satisfy the phase-matching. In LBO, the extraordinary refraction index is strongly dependent on the crystal temperature, allowing the noncritical phase-matching condition at a certain temperature. In this case, the generated photons travel parallel to the incoming beam. A critical phase-matching can be instead obtained using a CLBO crystal, choosing the right incidence angle of the beam. In this configuration the incoming beam and the higher order harmonic are affected by walkoff, that must be compensate by an analogue crystal rotating in the opposite direction.

The 4th harmonic photons then undergo an intensity profile shaping both in temporal and spatial domain, exploiting birefringent crystals for the temporal shaping and the so called π -Shaper for the spatial shaping. Temporal shaping based on birefringent crystals presents some important advantages in terms of stability and simplicity respect to conventional delay lines. For a linearly polarized laser beam incident on the birefringent crystal travelling on the z axis, if the refractive index of such crystal are different for the x and y axes, the two filed components will move at different group velocities, presenting a temporal separation of $t_d = |n_{g,o}L - n_{g,e}L|/c$. Further replicas are generable adding a crystal of $L/2$ lenght at the end of the first. Then, using n crystals it is possible to generate $2n$ replicas that can be

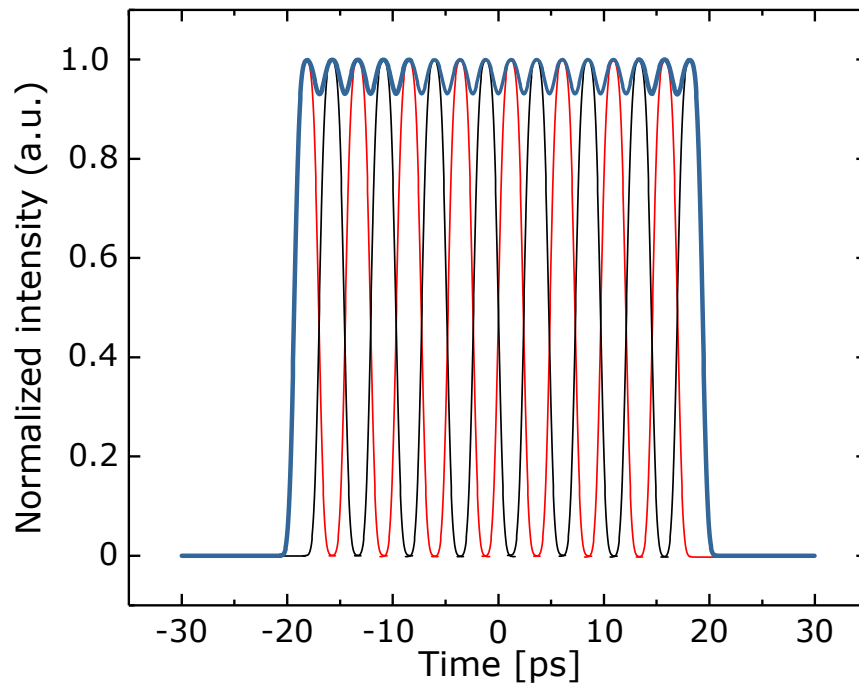
summed together to obtain one rectangular-shaped pulse as represented in Figure 2.6a. As written above, spatial shaping is performed by a π -Shaper. This kind of device involves aspherical lenses that rearrange the Gaussian intensity profile of the incoming laser pulse, in order to obtain a rectangular intensity distribution (Figure 2.6b). Such rectangular profile is finally reproduced on the photocatode by lens system.

Amplitude modulator (FEL line)

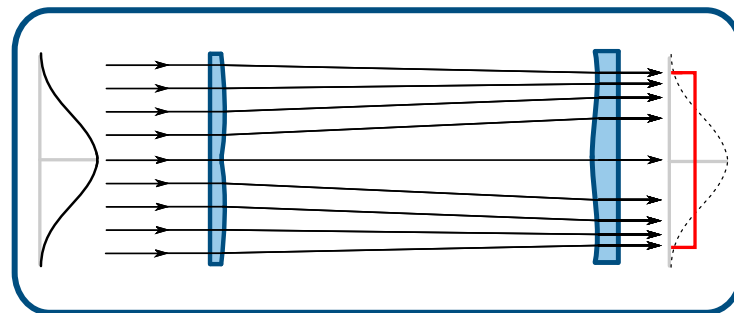
As previously written, the laser pulse is used to generate electrons for the Free Electron Laser, but with a repetition rate of 1 MHz, 100 lower than the laser one. In order to reduce the repetition rate, it is possible to use a Mach-Zender amplitude modulator (which is shown in Figure 2.7). This kind of amplitude modulator exploits induced modifications of the refraction index of the laser pulse path material. Using two different arms and three different electrodes (used to control the electric field inside the arms material) it is possible to create a phase difference between the pulses passing through the arms, leading to an interference phenomenon. With a properly choice of the introduced phase delay, it is possible to induce destructive interference and control the output power. Repetition rate reduction is obtained if only one pulse in a hundred can leave the modulator.

Photonic Machine R&D program

R&D program on the "Photonic Machine" has been started in dott.Cialdi's laboratory at Physics Department and aims to define and test all the main components of the laser system and to make the completion of the BriXSino demonstrator possible. The three main parts of the laser system on which the R&D activities will be performed are: the Fabry-Perot cavity, the amplifier and the lines for the RF-guns. At the moment, an Orange Yb fiber-doped oscillator by Menlo is in use, with a repetition rate of 100 MHz and 200 mW of amplification stage. The Fabry Perot cavity in use is a bow-tie type with 4 mirrors (two flat and two concaves, with a radius of curvature of 750 nm) such as the one provided for MariX. The development of this system is of fundamental importance for many aspects such the development of the stabilization system, the definition of the final geometry with respect to the angles of impact and also to develop the alignment and measurement techniques of the spot size in the focus point and on the mirrors of the cavity. As already written in the introduction of this work, this thesis has been developed in this framework.



(a)



(b)

Figure 2.6 (a): Simulation of a 40 ps pulse which temporal shape has been elongated by the use of 4 α -BBO birefringent crystal. (b): Scheme of a π -Shaper. It can be noted that the initial gaussian shape has changed into a rectangular profile (drawn in red). Figures from [1].

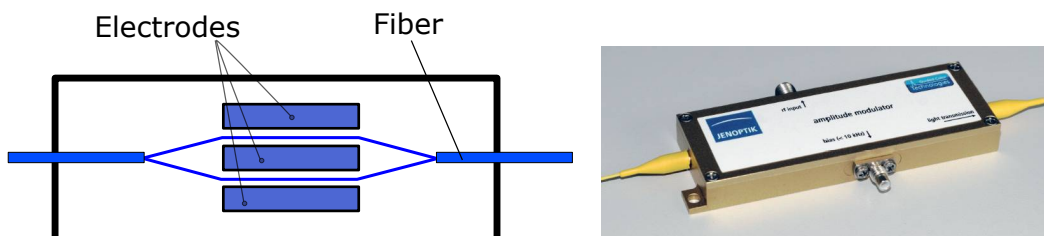


Figure 2.7 Example of Mach-Zender amplitude modulator. Picture from [1].

Chapter 3

Theoretical concepts: *active optical stabilization*

A good matching between the Fabry-Perot cavity and the laser source can be reached only with an appropriate optical stabilization on the system. In order to understand the theory behind this key-topic, the useful concept of Power Spectral Density will be firstly introduced. After this, we will introduce the basic concepts of mode-locking lasers and optical cavities. Then we will deal with the modeling of a stabilization system like the one used during this thesis work, introducing the theory necessary to understand and describe each of its parts.

3.1 Power Spectral Density and noise

An introduction about Power Spectral Density and its application in quantifying noise in a physical system is necessary to better understand the work done in this thesis. In particular, we are interested in the noise of the cavity-laser system that we have to stabilize using the external reference laser. In order to define what is a noise in a signal, we first introduce a generic ideal time-dependent sine wave signal [12]:

$$v_{\text{ideal}}(t) = V_0 \cos(2\pi\nu_0 t + \phi_0) \quad (3.1)$$

Where V_0 is the amplitude, ν_0 is the frequency and ϕ_0 is a constant phase in radians. In a system where some noise is present, the signal has to be re-written as

$$v_{\text{noisy}}(t) = [V_0 + \varepsilon(t)] \cos[2\pi\nu_0 t + \phi(t)] \quad (3.2)$$

Two new terms have been introduced: amplitude noise $\varepsilon(t)$ and phase noise $\phi(t)$. Amplitude noise is such that $\overline{\varepsilon(t)} = 0$ and $|\varepsilon(t)| \ll |V_0|$, while phase noise is such that $\overline{\phi(t)} = 0$ and $|\phi(t)| \ll 2\pi\nu_0$. We can then introduce the concept of *instantaneous frequency* from the cosine argument in $\nu_{\text{noisy}}(t)$ formula.

$$\nu(t) = \frac{1}{2\pi} \frac{d}{dt} [2\pi\nu_0 t + \phi(t)] = \nu_0 + \frac{1}{2\pi} \frac{d\phi(t)}{dt} \quad (3.3)$$

Frequency noise of a signal refers to random fluctuations of the *instantaneous frequency* [13]. We can hence define frequency fluctuations from Equation 3.3, subtracting ν_0 from $\nu(t)$ and obtaining

$$\Delta\nu(t) = \nu(t) - \nu_0 = \frac{1}{2\pi} \frac{d\phi(t)}{dt} \quad (3.4)$$

As for amplitude and phase noise, $\overline{\Delta\nu(t)} = 0$ and we can also see that frequency noise is related to phase noise simply by a temporal derivative (and by a multiplicative constant). A concept strictly related to noise is the *Power Spectral Density*, because PDS describes how the power of a noisy signal is distributed over the frequencies. In order to find out about its mathematical definition, we can take a generic signal x , which is variable in time. Then we have $x = x(t)$ and its Fourier transform over the time interval $[0, T]$ is defined as

$$x(f) = \frac{2}{T} \int_{-T/2}^{T/2} x(t) e^{-i2\pi ft} dt$$

Such definition has been chosen in order to be coherent with the FFT function calculated by the oscilloscope we used in our experimental setup. This Fourier transform definition can be also advantageous because so calculated values are independent from the selected integration time T . The Power Spectral Density of $x = x(t)$ is defined as the squared modulus of its continuous Fourier transform, but the straightforward approach does not work in case of fluctuation around a long term mean value. For this reason, another definition can be used:

$$S(f) = \lim_{T \rightarrow \infty} \frac{T}{2} |x(f)|^2 \quad (3.5)$$

Here the integral in the continuous Fourier transform is restricted to a finite time interval, in order to avoid problems of convergence. Then, the limit permits to calculate the value for large time intervals.

Another definition takes as a starting point the Wiener-Khinchin theorem and this is convenient in certain situations. The Wiener-Khinchin theorem (or Wiener-Khintchin

theorem) links the Power Spectral Density to the autocorrelation function of $x(t)$:

$$S(f) = \int_{-\infty}^{\infty} R(\tau) e^{-i2\pi f\tau} d\tau$$

The autocorrelation function of $x(t)$ is generally defined as $R(\tau) = \langle x(t)x(t+\tau) \rangle$, where $\langle \cdot \rangle$ indicates the ensemble average.

It is worth to note that for stationary and ergodic systems the ensemble average is equal to time average, so when $\tau = 0$ this second definition of Power Spectral Density equals to the first written above. Moreover, when a PSD is taken in account, it is important to check if the *one sided* definition or the *two sided* definition has been chosen. In *one sided* PSD only positive frequencies are taken in account but with double contribution, like in Equation 3.5, while in *two sided* PSD negative frequencies occur in the calculation. The presence of a factor 2 can help in the distinction, sometimes hard.

The variance of x in a certain range of noise frequencies is given as an integral over the one sided PSD:

$$\sigma_x^2|_{[f_1, f_2]} = \int_{f_1}^{f_2} S_x(f) df$$

Using Power Spectral Density we can quantify the noise in our experimental setup. In the coupled cavity-laser system, frequency fluctuations can lead to loss of resonance. For this reason, frequency noise suppression is a key-point of our work (stabilization method will be widely explained in next sections and chapters). Fluctuations in frequency can be caused essentially by mechanical vibrations that change the cavity length and laser frequency instabilities. One sided Power Spectral Density of frequency noise is

$$S_v(f) = \lim_{T \rightarrow \infty} \frac{2}{T} \left\langle \left| \int_{-T/2}^{T/2} \Delta v(t) e^{-i2\pi ft} dt \right|^2 \right\rangle$$

that is measured in H_z^2/H_z [12]. The variance of frequency noise due to the frequency range $[f_1, f_2]$ is easily obtained as

$$\sigma_v^2|_{[f_1, f_2]} = \int_{f_1}^{f_2} S_v(f) df$$

Frequency Noise PSD is linked to the Phase Noise PSD by

$$S_v(f) = \frac{|i2\pi f|^2}{(2\pi)^2} S_\phi(f) = f^2 S_\phi(f)$$

then

$$S_\phi(f) = \frac{1}{f^2} S_v(f)$$

that trivially follows from the relation between $\phi(t)$ and $\nu(t)$ in instantaneous frequency formula. Phase Noise PSD is measured in $[rad^2/Hz]$

Deviation from maximum power in cavity could be caused either by frequency fluctuations over the resonance frequency or by change in laser intensity, that is why the concept of Relative Intensity Noise will be briefly treated. Intensity noise describes fluctuations in the laser output power[14] and it is usually quantified using the so called RIN, Relative Intensity Noise. Such kind of noise is due to many factors that depend, for example, on the typology of laser used. The RIN can be obtained starting from the autocorrelation function $C_{PP}(\tau)$ of power fluctuations δP around the average laser power $\langle P \rangle$.

$$C_{PP}(\tau) = \langle \delta P(t) \delta P(t + \tau) \rangle / \langle P \rangle^2$$

The Fourier Transform of $C_{PP}(\tau)$ is the RIN.

$$RIN(\omega) = \int_{-\infty}^{\infty} C_{PP}(\tau) \exp(i\omega\tau) d\tau$$

RIN is usually dBc/Hz (where dBc are dB below carrier). At last, it is important noting that intensity and frequency can be related by non-linear phenomena like Self-Phase-Modulation that make noise stabilization harder so it is important avoiding such effect especially in amplification stages.

3.2 General scheme of the feedback

The feedback system used to perform active stabilization in this thesis work can be schematized as in Figure 3.1 and consists of the following parts:

- a *Reference*, in this case the optical frequency ν_r of the mode-locking laser;
- a *Source* that we want to lock to the Reference and which in our case is the frequency of the Fabry Perot cavity ν_s ;
- a *Discriminator*, which reads the frequency difference $\Delta\nu = \nu_r - \nu_s$ between the Reference and the Source, generating an error signal V_D according to it;
- a *Servo*, which elaborates the Discriminator signal and send an output signal in turn to the last stage;
- an *Actuator*, which reads the Servo signal and applies to the Source changing the frequency ν_s of $\delta\nu$.

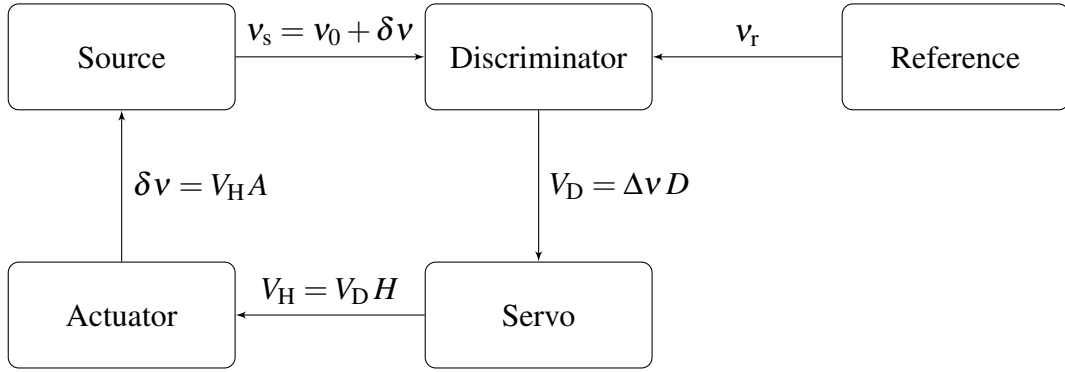


Figure 3.1 Conceptual scheme of the feedback used for the stabilization of the system. Here D , H and A are the complex transfer functions of discriminator, servo and actuator respectively and $\Delta v = v_r - v_s$.

Discriminator, servo and actuator are representable by three complex transfer functions $D(f)$, $H(f)$ and $A(f)$, depending on the frequencies f at which Δv fluctuates due to noise. D links the input and the output of the discriminator, H of the servo and A of the actuator. When we consider the closed loop as shown in the scheme, then we have a global transfer function $G(f)$ given by the product of the three single contribution

$$G(f) = D(f) H(f) A(f) \quad (3.6)$$

Because $G(f)$ is a complex function (product of complex functions), both amplitude and phase are to take in account.

The output signal of feedback element can be written as follows. The discriminator produces a voltage signal according to $\Delta v = v_r - v_s$, thus

$$V_D(f) = [v_r(f) - v_s(f)] D(f)$$

The servo elaborates the error signal, then we obtain

$$V_H(f) = V_D(f) H(f)$$

The last block is the actuator that reads the output of the servo and corrects the source. In particular it adds the following quantity to the source frequency

$$\delta v(f) = V_H(f) A(f)$$

After servo operates on the source

$$\nu_s(f) = \nu_0(f) + \delta\nu(f) = \nu_0(f) + V_H(f) A(f)$$

where ν_0 is the initial optical frequency of the source. Closing the loop we have

$$\nu_s(f) = \nu_0(f) + \Delta\nu(f) D(f) H(f) A(f) = \nu_0(f) + \Delta\nu(f) G(f)$$

Using equations written above it is simple obtain that

$$\nu_s(f) = \frac{1}{1+G(f)} \nu_0(f) + \frac{G(f)}{1+G(f)} \nu_r(f) \quad (3.7)$$

If $G(f)$ is real and $G(f) \rightarrow \infty \forall f$, we have $\nu_s(f) = \nu_r(f)$, which means that the cavity follows the reference frequency fluctuations: they are perfectly locked.

We can then calculate the Power spectral density of the frequency noise, assuming that the fluctuations of the cavity frequency $\nu_0(f)$ and the reference frequency $\nu_r(f)$ are uncorrelated and so leading to a great simplification, because mixed terms referred to ν_0 and ν_r cancel, then

$$S_s(f) = \frac{1}{|1+G(f)|^2} S_0(f) + \frac{|G(f)|^2}{|1+G(f)|^2} S_r(f) \quad (3.8)$$

The perfect locking is reached when because of $|G(f)| \rightarrow \infty$ we obtain $S_s(f) = S_r(f)$. It is clear that the most important term is not the source frequency $\nu_s(f)$, but the difference between reference and source frequencies $\Delta\nu(f) = \nu_r(f) - \nu_s(f)$: as our aim is to lock the source and the reference, $\Delta\nu$ has to ideally vanish. We can write the expression of $\Delta\nu(f)$ Power Spectral Density starting from

$$\begin{aligned} |\Delta\nu(f)|^2 &= |\nu_r(f) - \nu_s(f)|^2 = \\ &= |\nu_r(f)|^2 + |\nu_s(f)|^2 - 2\text{Re} [\nu_s(f) \nu_r(f)^*] = \\ &= |\nu_r(f)|^2 + \left| \frac{1}{1+G(f)} \nu_0(f) + \frac{G(f)}{1+G(f)} \nu_r(f) \right|^2 + \\ &\quad - 2\text{Re} \left[\left(\frac{1}{1+G(f)} \nu_0(f) + \frac{G(f)}{1+G(f)} \nu_r(f) \right) \nu_r^*(f) \right] \end{aligned}$$

Deletin mixed terms, we finally have

$$\begin{aligned}
 S_{\Delta v}(f) &= S_r(f) + \frac{1}{|1+G(f)|^2} S_0(f) + \frac{|G(f)|^2}{|1+G(f)|^2} S_r(f) - 2\text{Re} \left[\frac{G(f)}{1+G(f)} S_r(f) \right] = \\
 &= \frac{1}{|1+G(f)|^2} S_0(f) + \left| 1 - \frac{G(f)}{1+G(f)} \right|^2 S_r(f) = \\
 &= \frac{1}{|1+G(f)|^2} S_0(f) + \frac{1}{|1+G(f)|^2} S_r(f)
 \end{aligned}$$

so

$$S_{\Delta v}(f) = \frac{S_0(f) + S_r(f)}{|1+G(f)|^2} \quad (3.9)$$

$S_0(f)$ and $S_r(f)$ have non-negligible values for many frequencies, because of noise in the Fabry-Perot cavity and the laser (for example mechanical vibrations or air turbolences) that is directly transferred to Δv . Such noise can be suppressed (as shown in the last equation) maximizing $|1+G(f)|^2$. It is important notice that the phase of $G(f)$ takes a fundamental role, especially when $|G(f)| \approx 1$.

3.2.1 Barkhausen stability criterion

Spontaneous oscillations of a system are typically damped by dissipative phenomena and do not propagate. However, when the so called Barkhausen criterion is satisfied [15] self-oscillations could occur in a system with feedback and can disturb the correct operation of the system. The Barkhausen criterion can be easily understood taking a simple system with two blocks represented by complex transfer functions $A(f)$ and $B(f)$ and connected in a loop as shown in Figure 3.2 and with a negative feedback (discussion for positive feedback is trivial), we have a global transfer function [15]

$$T(f) = \frac{A(f)}{1+A(f)B(f)}$$

Oscillation results when the feedback system is not able to find a stable state because its transfer function cannot be satisfied, namely when $1+G(f) = 0$ with $G(f) = A(f)B(f)$, that is $|G(f)| = 1$ and at the same time the phase of $G(f)$ equals $\pi + 2k\pi$. When a negative feedback system is in such condition, it is satisfying the Barkhausen criterion (it occurs for positive feedback if the phase is null). Spontaneous oscillation frequency f_{osc} is the frequency at which the Barkhausen criterion is satisfied. Since the exact theoretical Barkhausen criterion is hard to satisfy in a real apparatus, we have to consider the experimental conditions in which self-oscillations could occur without having exactly $|G(f)| = 1$ and phase $\phi(f) = \pi$.

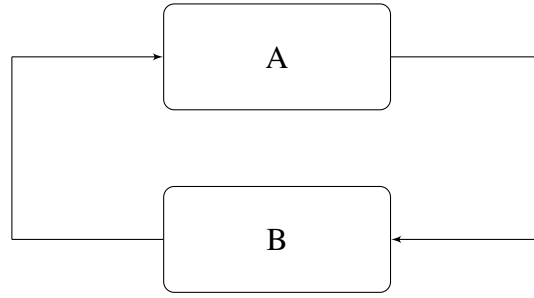


Figure 3.2 A simple scheme of a system with feedback.

Such experimental condition corresponds to having a slope of $|G(f)|$ greater in modulus than 20dB per decade¹ when $|G(f)| = 1$ and an high phase slope $\frac{d\phi}{df}$ when the phase is closer than 45 degrees from 180° [16]. In fact, if the value of phase or amplitude is near its critical value, but the other quantity varies quickly (then they span a wide range of phase and amplitude values around π and 1 respectively), we have high possibilities to matching an instability point. This suggests for example that we will have to use single pole filters in the system, because their slope is -20 dB per decade and their phase slope is enough low.

3.2.2 Pound-Drever-Hall technique

The frequency locking of a Fabry-Perot optical cavity to an external laser reference can be performed using the so called Pound-Drever-Hall technique [4]. The idea behind this method is simple: it is possible to create an error signal that allows to discriminate if the cavity has to be lengthened or shortened in order to be in resonance with the external laser, decoupling frequency instabilities from laser intensity fluctuation. The error signal in PDH technique is obtained starting from the reflected beam of the cavity. The reflection coefficient for a symmetric cavity can be written as [17][4]

$$F(\omega) = \frac{E_{\text{reflected}}}{E_{\text{input}}} = \frac{(1 - \Delta) r \left(e^{-i\frac{\omega - \omega_0}{FSR}} - 1 \right)}{1 - (1 - \Delta) r^2 e^{-i\frac{\omega - \omega_0}{FSR}}} \quad (3.10)$$

where Δ represents the internal losses of the cavity for the single round-trip, r is the amplitude reflection coefficient of each mirror, ω_0 is the resonance frequency so that $\delta\omega = \omega - \omega_0$ is the detuning between the cavity and the external source and FSR is its free spectral range. The beam that reflects from Fabry-Perot cavity consists of a coherent sum of two different beams: the *promptly reflected beam* which is directly reflected by the first mirror and does not enter in the cavity and the *leakage beam* which is the small part of radiation inside the cavity

¹Note that the slope is negative, since the phase is π .

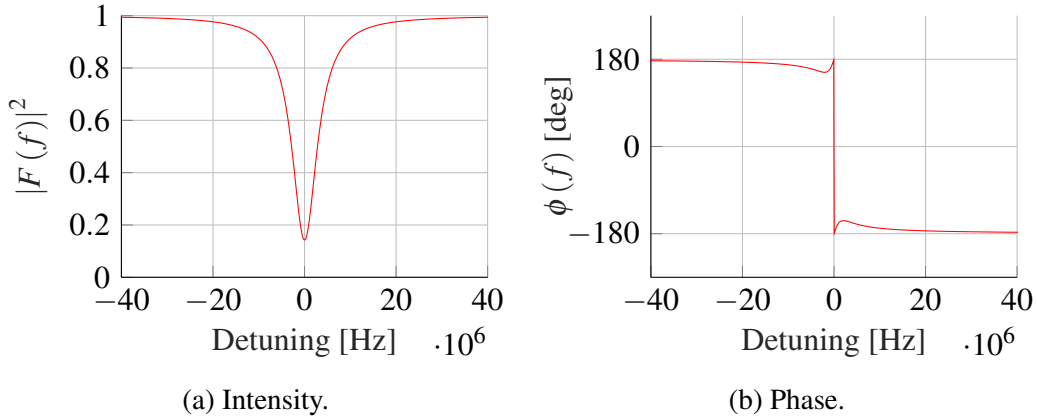


Figure 3.3 Example of intensity and phase of the cavity reflectivity $F(f)$ in function of the detuning between input beam and cavity resonance frequency.

that escapes from the first mirror. Their relative phase depends on the detuning between the laser and the cavity. When the cavity is perfectly resonant with the laser the promptly reflected beam and the leakage beam are 180° , so they interfere destructively. If the cavity is not perfectly resonant, the phase difference is less than 180° so the reflected signal is higher than in the perfect resonance condition. The intensity $|F(\omega)|^2$ and the phase $\phi(\omega)$ are shown in Figure 3.3. As we already noted is fundamental that the error signal needed to stabilize the cavity must be able to discriminate whether the resonance frequency is too high or too low. Thus, we cannot use the intensity signal, because it is an even function around the resonance $\delta\omega = 0$ and it is impossible to determine in which direction the cavity frequency has to be moved. However, the phase function is odd around the resonance, and it could be used as error signal. Unfortunately we do not have direct access to it, because the light signals detection is performed via photodiodes, which read intensity signal only. PDH technique permits to bypass this problem, permitting to sample the phase signal of the reflected beam indirectly. A phase modulator, typically a non linear crystal, is placed before the cavity and fed with a sinusoidal voltage, which creates an electric field according to it, as shown in Figure 3.4. This field changes the refraction index of the crystal as

$$n(t) = n_e - \frac{1}{2} n_e^3 r_{33} E \quad (3.11)$$

where n_e is the extraordinary index of refraction of the crystal, r_{33} is the element (3,3) of the electro-optical tensor of the crystal and E is the electric field applied in n_e direction. If we generate a sinusoidal electric field by applying a voltage $V(t) = V_0 \sin \Omega t$ so that $E = \frac{V(t)}{d}$ with d thickness of the crystal, then Equation 3.11 allows us to write the field out of the

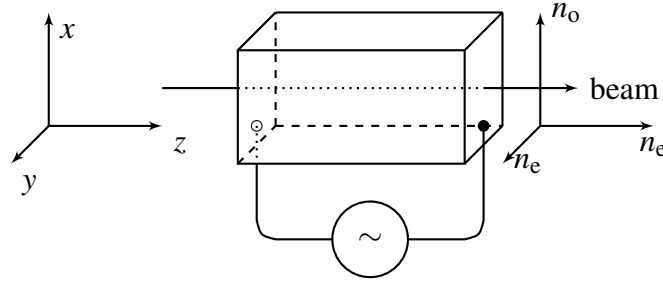


Figure 3.4 Scheme of the non linear crystal used as a phase modulator. The electrodes apply a high sinusoidal voltage on one of the extraordinary axis of the crystal n_e and generate the sidebands.

crystal as

$$\begin{aligned}
 E(t) &= A \exp(-i\omega t + ikz) = \\
 &= A \exp\left(-i\omega t + i\frac{2\pi}{\lambda} n(t) z\right) = \\
 &= A \exp\left(-i\omega t + i\omega \frac{z}{c} \left(n_e - \frac{1}{2} n_e^3 r_{33} \frac{V_0}{d} \sin \Omega t\right)\right) = \\
 &= A \exp(-i\omega t) \exp\left(i\omega \frac{z}{c} n_e\right) \exp\left(-i\frac{\omega z}{2c} n_e^3 r_{33} \frac{V_0}{d} \sin \Omega t\right)
 \end{aligned}$$

It is clear that we have three incident waves, the carrier and two *sidebands* of frequency ω , $\omega + \Omega$ and $\omega - \Omega$ respectively. If we define $\beta = \frac{1}{2} \frac{\omega z}{c} n_e^3 \frac{V_0}{d} r_{33} = \frac{\pi z}{\lambda} n_e^3 \frac{V_0}{d} r_{33}$ and $E_0 = A \exp\left(i\omega \frac{z}{c} n_e\right)$, we can write

$$E(t) = E_0 \exp(i\omega t) \exp(i\beta \sin \Omega t)$$

We can expand this expression, using Bessel functions, to

$$E(t) \approx E_0 [J_0(\beta) + 2iJ_1(\beta) \sin \Omega t] \exp(-i\omega t) = E_0 [J_0(\beta) e^{i\omega t} + J_1(\beta) e^{i(\omega+\Omega)t} - J_1(\beta) e^{i(\omega-\Omega)t}]$$

If $P_0 \equiv |E_0|^2$ is the total power in the incident beam, then the power of the carrier is $P_c = J_0^2(\beta) P_0$, while the power of each first-order sideband is $P_s = J_1^2(\beta) P_0$. Note that when modulation is small, so when $\beta < 1$, we can neglect the power of all higher-order sidebands and write $P_0 \approx P_c + 2P_s$. Now we have to consider the reflected beam, so we multiply the electric field by the function defined in Equation 3.10. We obtain

$$E_{\text{ref}} = E_0 \left[F(\omega) J_0(\beta) e^{i\omega t} + F(\omega + \Omega) J_1(\beta) e^{i(\omega+\Omega)t} - F(\omega - \Omega) J_1(\beta) e^{i(\omega-\Omega)t} \right]$$

As previously explained, photodiodes can measure intensity only. The power of the reflected beam is given by $P_{\text{ref}} \equiv |E_{\text{ref}}|^2$. Thus after some algebraic manipulations, the power reflected by the cavity can be written as²

$$\begin{aligned} P_{\text{ref}} = & P_c |F(\omega)|^2 + P_s \left(|F(\omega + \Omega)|^2 + |F(\omega - \Omega)|^2 \right) + \\ & + 2\sqrt{P_c P_s} \text{Re} [F(\omega) F^*(\omega + \Omega) - F^*(\omega) F(\omega - \Omega)] \cos \Omega t + \\ & + 2\sqrt{P_c P_s} \text{Im} [F(\omega) F^*(\omega + \Omega) - F^*(\omega) F(\omega - \Omega)] \sin \Omega t + (2\Omega \text{ terms}) \end{aligned} \quad (3.12)$$

We are interested in oscillating terms, because they sample the phase of reflected field. There are two oscillating terms in the previous equation: a cosine and a sine. We put ourselves in the case of modulation frequency Ω greater than the line width $\delta\omega$ of the cavity³. In this situation only the sine term is considered, because $F(\omega) F^*(\omega + \Omega) - F^*(\omega) F(\omega - \Omega)$ is purely imaginary. This result is evident considering that for fast modulation the carrier is perfectly resonant with the cavity, while the sidebands are not. In particular they are totally reflected, so we can make the approximation $F(\omega \pm \Omega) \rightarrow -1$, which brings to [4]

$$F(\omega) F^*(\omega + \Omega) - F^*(\omega) F(\omega - \Omega) \sim -2i \text{Im} [F(\omega)]$$

As we have already written, this quantity is purely imaginary, thus the $\cos \Omega t$ term in Equation 3.12 vanishes. Typically the power of the carrier is much greater than the power of the sidebands (up to 10^2 , since $\beta \approx 0.1$), so $P_c \gg P_s$ and we can neglect the term proportional to P_s . Equation 3.12 becomes

$$P_{\text{ref}} \approx P_c |F(\omega)|^2 - 4\sqrt{P_c P_s} \text{Im} [F(\omega)] \sin \Omega t + (2\Omega \text{ terms}) \quad (3.13)$$

The photodiode converts this power into a voltage signal, which is then amplified. Amplifiers usually cut the DC component, so it is possible to neglect the first term in Equation 3.13. Notice that the information about the cavity position contained in $P_{\text{reflected}}$ is at the frequency Ω contained in the sine term. In order to directly access the quantity $\text{Im} [F(\omega)]$, we have to demodulate the signal with the frequency Ω by a mixer, which multiplies the signal itself by a modulation $\sin \Omega t$. From simple trigonometric considerations it can be shown that the information at frequency Ω has been moved to zero frequency and 2Ω frequency. Typically a low-pass filter is inserted so that double frequency terms can be neglected, bringing to the

²Notice that we expressed every quantity in function of ω and Ω , which are pulsations, while experimentally one deals with pure frequencies f and ν . Thus, for the applications it will be necessary to make the substitutions $\omega = 2\pi f$ and $\Omega = 2\pi \nu$.

³ $\delta\omega$ is defined as the Full Width at Half Maximum (FWHM) of the amplitude of the cavity reflection function.

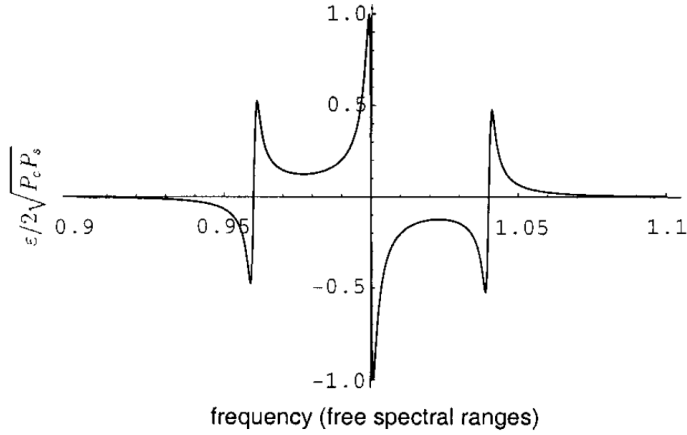


Figure 3.5 Typical PDH error signal in the case of fast modulation (figure from [4]).

Pound-Drever-Hall error signal

$$\varepsilon_{\text{PDH}} \approx -\sqrt{P_c P_s} \text{Im} [F(\omega) F^*(\omega + \Omega) - F^*(\omega) F(\omega - \Omega)] \cos \phi \quad (3.14)$$

where ϕ is the phase shift between mixed signals and it is usually set to zero. ε_{PDH} is used to drive the cavity and its shape in fast modulation case is shown in Figure 3.5.

3.3 Source: optical cavities

The source in the feedback system is a Fabry-Perot four mirror bow-tie optical cavity in which two mirrors are flat and two are curved. An optical cavity is an object formed by two or more mirrors which accumulates electromagnetic radiation inside. There the electromagnetic field can have only some determined shapes imposed by the boundary conditions and in particular stationary waves at certain frequencies will be formed [14]. These stationary waves are called *modes* and they are characterized by three indexes: one longitudinal and two transverse. In general, the modes of any cavity can be obtained from the Huygens-Fresnel equation for the electromagnetic field with a fixed cavity geometry [14] in paraxial approximation. By imposing that after one round-trip the field reproduces its shape, so that $\mathbf{E}(x, y, 2L) = \sigma \exp(-ik2L) \mathbf{E}(x, y, 0)$ where σ is a complex eigenvalue. It is worth noting that the field of the modes reproduces itself after a round trip, so they can be considered as eigenstates of the cavity with eigenvalue σ : a resonator takes the incoming field and projects

it on its eigenstates [14]. When cylindrical symmetry is broken the eigenfunctions are the *Hermite-Gaussian modes*:

$$E_{npq}(x, y, z) = E_0 \frac{w_0}{w(z)} H_p \left(\sqrt{2} \frac{x}{w(z)} \right) \exp \left(-\frac{x^2}{w(z)^2} \right) H_q \left(\sqrt{2} \frac{y}{w(z)} \right) \exp \left(-\frac{y^2}{w(z)^2} \right) \exp \left[-i \left(k_{npq} z - (1 + p + q) \arctan \frac{z}{z_R} + \frac{k(x^2 + y^2)}{2R(z)} \right) \right] \quad (3.15)$$

With H_N Hermite polynomial with index N , while $w(z)$ and $R(z)$ follow the trend imposed in a Gaussian Beam. Each mode has a defined frequency, given by

$$\nu_{npq} = FSR \left(n + \frac{1 + p + q}{2\pi} \arccos m \right) \quad (3.16)$$

where p and q are the transverse mode indexes, n is the longitudinal mode index and m is the so called *stability parameter*, which depends on the geometry of the cavity and it is related to the coefficients of the round trip matrix M_{RT} . Moreover, a cavity is considered *stable* if its stability parameter satisfies $|m| < 1$ [14]. It is worth noting that the 2D nature of the cavity produces different beam diameters in the vertical and horizontal axis. Such asymmetry alters the mode structure, then mode frequencies become [14][10]:

$$\nu_{npq} = FSR \left(n + \frac{1/2 + p}{2\pi} \arccos m_H + \frac{1/2 + q}{2\pi} \arccos m_V \right) \quad (3.17)$$

where m_V and m_H are the stability parameters of the vertical axis and horizontal axis respectively. The Hermite-Gaussian mode structure is shown in Figure 3.6

As written above, MariX cavity is a four mirror Fabry-Perot resonator. The incoming laser beam is reflected many times inside the cavity generating one partial wave at each round trip. If the round trip optical path is an integer multiple of the incident laser wavelength, the waves inside the cavity interfere constructively creating a strong field. Treating the four mirror FP resonator as an interferometer (as in scheme presented in Figure 3.7), the transmitted beam can be used to obtain informations about the radiation inside the cavity. The power transmission coefficient after the second cavity mirror at normal incidence is

$$T_B = \frac{(1 - R_1)(1 - R_2)}{\left[1 - \sqrt{R_{TOT}} e^{-i2\pi \frac{\delta\nu}{FSR}} \right]^2} \quad (3.18)$$

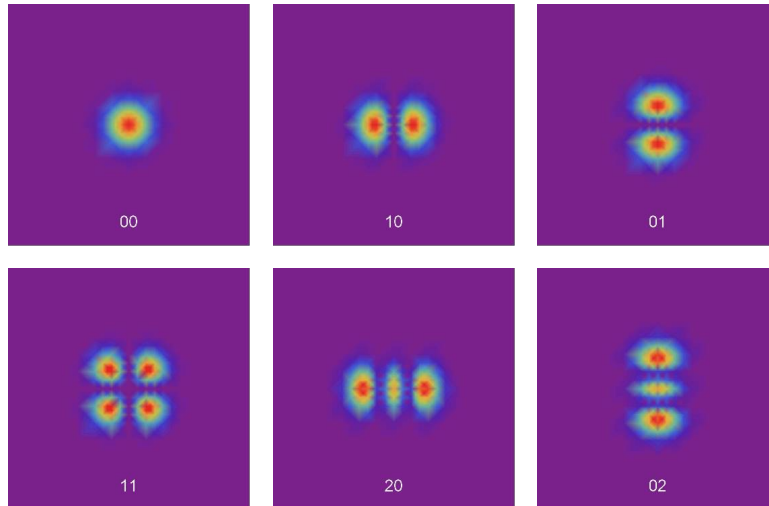


Figure 3.6 Low-order Hermite-Gaussian modes intensity profile theoretically calculated using Wolfram Mathematica software.

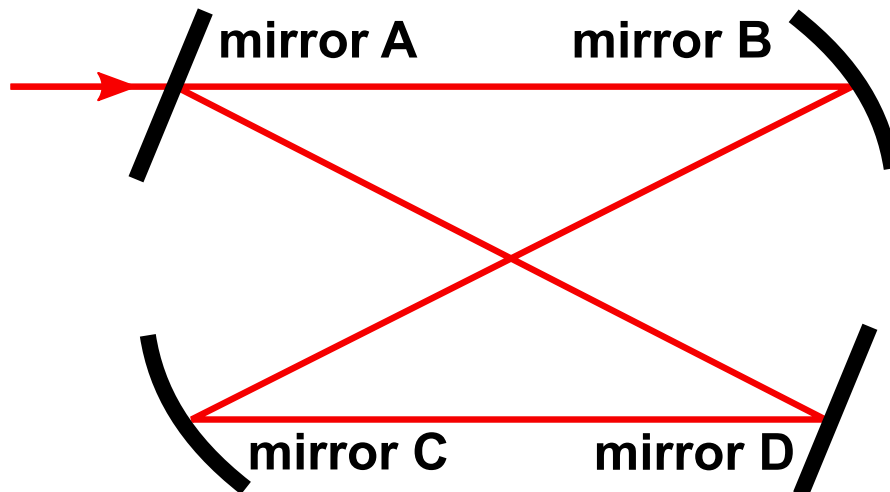


Figure 3.7 Four mirror Fabry-Perot cavity scheme: the first mirror is labeled *A*, the second is labeled *B*, the third is *C*, while the last one is named *D*.

Where R_A and R_B are the reflectivity of the first and output mirrors respectively, while $R_{TOT} = R_A \cdot R_B \cdot R_C \cdot R_D$ is the product of the reflectivities of all the mirrors constituting the cavity, FSR indicates the Free Spectral Range of the optical cavity and $\delta\nu$ is the frequency difference between the cavity resonance frequency and the light wave frequency. We can also write the transmission coefficients for the third and fourth mirror:

$$T_C = \frac{(1 - R_A)(1 - R_C) R_B}{\left[1 - \sqrt{R_{TOT}} e^{-i2\pi \frac{\delta\nu}{FSR}}\right]^2} \quad (3.19)$$

$$T_D = \frac{(1 - R_A)(1 - R_D) R_B R_C}{\left[1 - \sqrt{R_{TOT}} e^{-i2\pi \frac{\delta\nu}{FSR}}\right]^2} \quad (3.20)$$

Considering now the second mirror case only, when the coupling between the cavity and the laser is perfect (then when resonance frequency of the cavity is the same of the incoming wave), Equation 3.18 becomes

$$T_B = \frac{(1 - R_A)(1 - R_B)}{\left[1 - \sqrt{R_{TOT}}\right]^2} \quad (3.21)$$

We can then obtain the width of the transmission peak starting as

$$\Delta\nu_{FP} = FSR \frac{1 - (R_{TOT})^{1/2}}{\pi (R_{TOT})^{1/4}} \quad (3.22)$$

Equation 3.22 allows us to define a very important characteristic of a FP cavity: its *Finesse*:

$$F \equiv \frac{FSR}{\Delta\nu_{FP}} = \frac{\pi (R_{TOT})^{1/4}}{1 - (R_{TOT})^{1/2}} \quad (3.23)$$

Note that the Finesse depends only on the product of the four reflectivity coefficient R_{TOT} . The *Finesse* of a cavity is strictly related to the power gain G_{power}

$$G = \frac{F}{a} \quad (3.24)$$

where a is a coefficient dependent on the cavity mirrors properties. The undercoupled configuration allows the lowest a , then the highest gain. In particular, for an undercoupled Fabry-Perot cavity we have

$$G = \frac{F}{\pi/2} \quad (3.25)$$

The power gain is a fundamental quantity in MariX application, because it permits to obtain high power inside the cavity and then the desired X-ray flux produced by the electron-photon scattering.

We can also study important properties like the beam radius for a certain position or the waist at focus size and shape. As an example, it is possible to write the spot dimension at the optical coordinate z for each axis as

$$w(z) = \frac{FWHM(z)}{\sqrt{2 \ln 2}} \quad (3.26)$$

where $FWHM(z)$ indicates the full with half maximum size of the intensity profile at the same coordinate z . Cavity geometry determinates waist minimum size and spot dimension on mirrors and for the MariX cavity the better situation occurs near the edge of stability region, in near-confocal configuration. Indeed, in near-confocal configuration waist dimension is minimized, while spot size on mirrors is maximized (reducing thermal deformation of mirrors). Practically, the near-confocal configuration can be achieved approaching the 2 curved mirrors and restoring the length modifying the distance between the two flat mirrors.

3.4 Reference: mode locking laser

The reference in our feedback system is an infrared mode-locking pulsed laser and, as already explained, the optical cavity is locked to it. In order to reach a better comprehension of the physical system we have studied, a short exposition of mode locking lasers principles is here provided. In general lasers can operate in *continuous wave regime* or in *pulsed regime*. Some applications, like Compton Back-Scattering with electrons, as an example, cannot be performed by continuous wave laser because they need high powers or short optical pulses. Transient laser behavior allows one to obtain higher peak powers by concentrating the available energy in a single short optical pulse or in a periodic sequence of optical pulses. From dynamical point of view, pulsed laser behavior can be divided into two distinct categories[18]:

- Laser transient occurring on time scale of the order of the cavity photon lifetime, namely appreciably larger than the cavity round trip time. This includes gain-switching regime and Q-switching regime, which enable the generation of optical pulses as short as few nanoseconds.
- Laser transient occurring on time appreciably shorter than the cavity round trip time. These are basically multi-longitudinal-mode regimes and include mode-locking regime,

which permits the generation of trains of ultrashort laser pulses with duration down to few femtoseconds.

As written above, a mode-locking laser is used in our experimental setup and a description in frequency domain is here reported [14].

Let us now consider a laser oscillating on a large number of longitudinal modes. Under normal circumstances, the beam intensity of continuous wave oscillation will show a random time behavior, due to the random value of the phase associated to the each mode. The square of the electric field amplitude, defined as $|A(t)|^2$ of the output beam in the case of many oscillating modes of the same amplitude spaced in frequency by a frequency difference of $\Delta\nu$ between consecutive modes shows the mentioned time random behavior, as can be seen in Figure 3.8-a. Despite the randomness, the pulse waveform is formed by a superposition of N frequency, so it has some general properties of Fourier series. In particular, the waveform is periodic with a period $\tau_p = 1/\Delta\nu$ and light pulse of the random waveform presents a duration of $\Delta\tau_p$ approximately equal to the inverse of the total oscillating bandwidth, written in formula $\Delta\tau_p \approx 1/\Delta\nu_L$ where $\Delta\nu_L = N\Delta\nu$. We can observe that for lasers with relatively large gain bandwidths, $\Delta\nu_L$ might be comparable to it and hence pulses of very short duration (picoseconds or less) can be produced.

If we then suppose that the oscillating modes, while still having equal or comparable amplitudes, are made to oscillate with a definite relation of phase: the laser is referred to be *mode locked*. Many methods are used to obtain mode-locking and we will mention the most important later.

The simplest case is the one in which $N = 2n + 1$ longitudinal modes oscillate with the same amplitude E_0 and the phases φ_l locked according to a linear relation $\varphi_l - \varphi_{l-1} = \varphi$ where φ is a constant. The total electric field $E(t)$ at any point of the output beam is given by

$$E(t) = \sum_{l=-n}^{+n} E_0 \exp[i((\omega_0 + l\Delta\omega)t + l\varphi)] \quad (3.27)$$

where ω_0 is the pulsation of the central mode and $\Delta\omega$ is the frequency difference between consecutive modes. Total electric field can be rewritten as

$$E(t) = A(t) \exp i \omega_0 t \quad (3.28)$$

where

$$A(t) = \sum_{l=-n}^{+n} E_0 \exp[i l (\Delta\omega t + \varphi)] \quad (3.29)$$

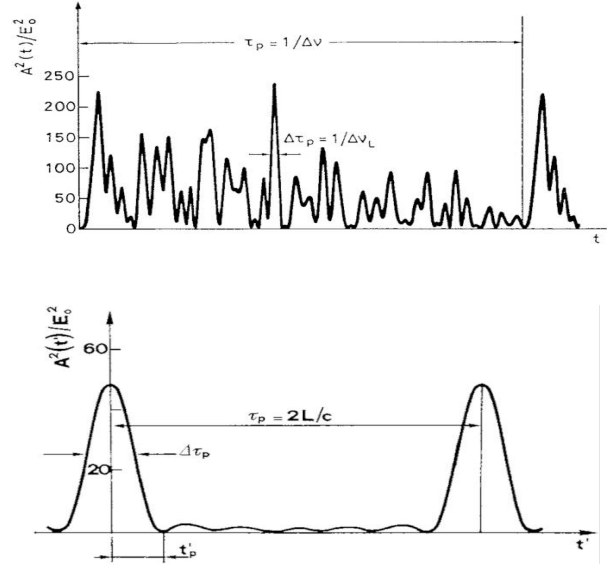


Figure 3.8 a) Electric field of many modes random distributed in time. b) Electric field pulsed obtained locking phases together (figure from [14]).

So $E(t)$ is representable in terms of a sinusoidal carrier wave whose amplitude $A(t)$ is time dependent. A variable change can be performed in order to calculate the time behavior of $A(t)$: we now choose a new time reference t' such that $\Delta\omega t' = \Delta\omega t + \varphi$. In terms of t' , $A(t)$ becomes

$$A(t) = \sum_{l=-n}^{+n} E_0 \exp[i l (\Delta\omega t')] \quad (3.30)$$

It is easy to recognize a geometric progression with ratio $\exp(i\Delta\omega t')$ that can be developed as

$$A(t) = E_0 \frac{\sin[(2n+1)\Delta\omega t'/2]}{\sin[\Delta\omega t'/2]} \quad (3.31)$$

The quantity $A^2(t)/E_0^2$ is shown in Figure 3.8-b. It is clear that as a result of the phase-locking condition, the oscillating modes interfere so as to produce a train of evenly spaced pulses. Maximums occur when $t' = 0$ and when the condition $(2\pi\Delta\nu t'/2) = \pi$ is satisfied, then two successive pulses are separated by a time

$$\tau_p = 1/\Delta\nu \quad (3.32)$$

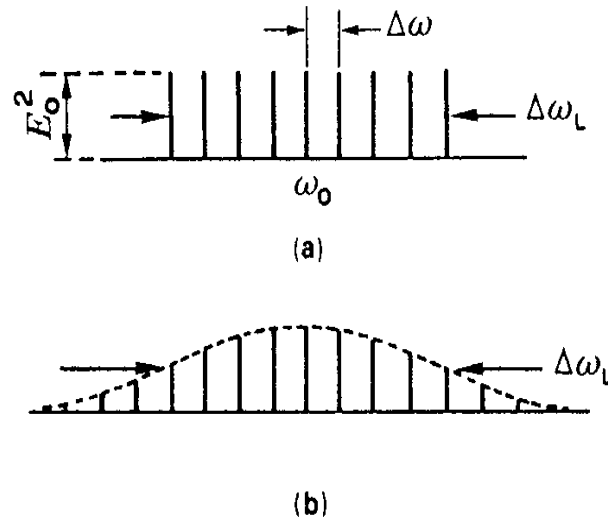


Figure 3.9 a) Frequency comb with equal field amplitude for each mode. b) Gaussian shaped frequency comb (figure from [14]).

The first zero of $A^2(t')$ occurs at time t_p' such that $[(2n+1)2\pi\Delta\nu t'] = \pi$. Since the FWHM $\Delta\tau_p$ of $A^2(t')$ is approximately equal to t_p' , we have

$$\Delta\tau_p \approx 2\pi / (2n+1)2\pi\Delta\nu = 1/\Delta\nu_L \quad (3.33)$$

Where $\Delta\nu_L$ is the total oscillating bandwidth, as defined above. So we have deduced the most important characteristic quantities of a mode-locking optical pulse, but we have restricted our considerations to the unrealistic case of equal-amplitude mode-spectrum. A more realistic theory can be developed assuming a bell-shaped form for the spectral envelope. As an example, it could be considered Gaussian distributed. In this case, the field amplitude E_l of the l -th mode is given by

$$E_l^2 = E_0^2 \exp \left[- \left(\frac{2l\Delta\nu}{\Delta\nu_L} \right)^2 \ln 2 \right] \quad (3.34)$$

where $\Delta\nu_L$ represent the *FWHM* of the spectral intensity divided by a factor 2π .

Starting from the same linear phase relation of the precedent case, it can be shown that the total field $E(t)$ can be again expressed as in Equation 3.29. Approximating the sum in $A(t')$ by an integral, the field amplitude becomes proportional to the Fourier transform of the spectral amplitude E_l . Then the square of $A(t)$, i.e. the pulse intensity is a Gaussian function of time:

$$A^2(t) \propto \exp \left[- \left(\frac{-2t}{\Delta\tau_p} \right)^2 \ln 2 \right] \quad (3.35)$$

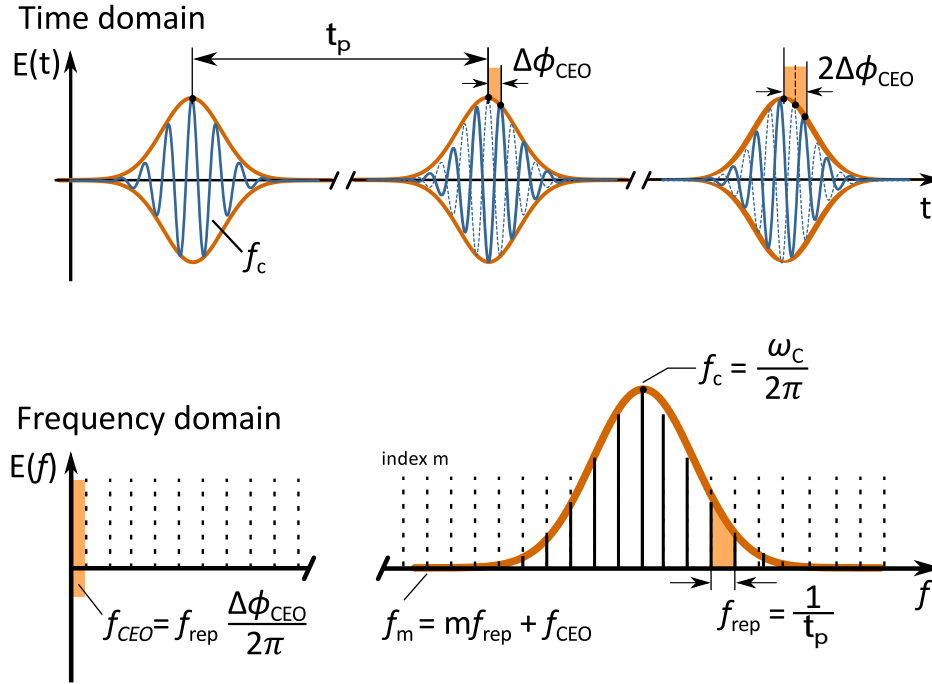


Figure 3.10 Time domain and Frequency domain representation of the mode-locking pulse where f_{CEO} and the phase shift $\Delta\phi$ are present.

Where $\Delta\tau_p$ is the width of the pulse intensity and can be seen as

$$\Delta\tau_p = 2 \ln 2 / \pi \Delta\nu_L \approx 0.441 / \Delta\nu_L \quad (3.36)$$

Ideally, in the time domain, the output of a mode-locking laser is a sequence of pulses that are copies of the same pulse separated by a time τ_p . When instead dispersion in cavity is considered, the time separation remain the same, but a slip of phase between different pulses is introduced as shown in Figure 3.10 [18]. In frequency domain this can be seen as a shift of the entire comb to the integer harmonics of f_{rep} by a frequency offset f_{CEO} (Carrier Envelope Offset). Then the l -th comb line corresponds to a frequency

$$f_l = l f_{rep} + f_{CEO} = f_{rep} (l + \Delta\phi_{CEO} / 2\pi) \quad (3.37)$$

It is then clear that the characteristic parameters in frequency comb generated by a mode-locking laser are two: the repetition rate τ_p and the frequency offset f_{CEO} .

Mode locking condition can be reached by many methods that can be divided into two categories[18]:

- *Active mode-locking*, in which the mode-locker is driven by an external source

- *Passive mode-locking*, in which the mode-locker is not externally driven

Active mode-locking is usually achieved by placing inside the laser cavity either a phase modulator which periodically varies the optical length of the cavity, or an amplitude modulator which produces a periodic modulation of the cavity loss. In some cases mode locking can be achieved by periodic modulation of the laser gain. We cite here three different passive mode-locking methods: fast saturable-absorber mode-locking, Kerr-lens mode-locking and Nonlinear Polarization Rotation (NPR) fiber lasers⁴. A fast saturable-absorber permits light oscillations only when it is saturated, favoring high intensity peaks. Most famous example of saturable-absorber is the so called SESAM. Kerr-lens mode-locking instead exploits the Kerr non-linear effect, that causes a dependence of refraction index of a material by the intensity of the radiation. If the laser cavity is projected to be stable only when the refraction index of a Kerr-medium inside it is the one obtained for high peak intensities, low intensity pulses will be lost during the round trip, leading to a selection of the pulses circulating in the cavity, then to the mode-locking condition. NPR fiber lasers exploit different polarization rotation in a nonlinear fiber for different pulse intensity [19]. If a pulse with elliptical polarization is sent into a nonlinear fiber, such polarization will rotate of a term proportional to the pulse intensity by nonlinear effect. Then, using $\lambda/4$ waveplates, $\lambda/2$ waveplates and linear polarizers it is possible to select high intensity narrow pulses, leading to mode-locking condition.

3.5 Discriminator and Servo: electronic concepts

The importance of Electronics in most of experimental fields of physics is huge, especially for experiments in which electronics is a fundamental part of the whole feedback system, like this thesis work. From this point of view the aim of this section is easily understandable: due to the presence of many electronic components (low pass filters, operational amplifiers, photodiodes and some others) it is important to introduce the basic concepts necessary for the comprehension of the experimental setup. Firstly we will describe filters used both in discriminator and in servo, then we will address the other main electronic components used.

3.5.1 Signal filtering

Electronic signal filtering can be obtained using a variety of different devices. In this thesis work we only use single pole low-pass and high-pass filters and Butterworth filters that are here described. Single pole ideal filters shown in Figure 3.11 consist of a resistance and

⁴NPR is the principle of operation of our Menlo Orange oscillator.

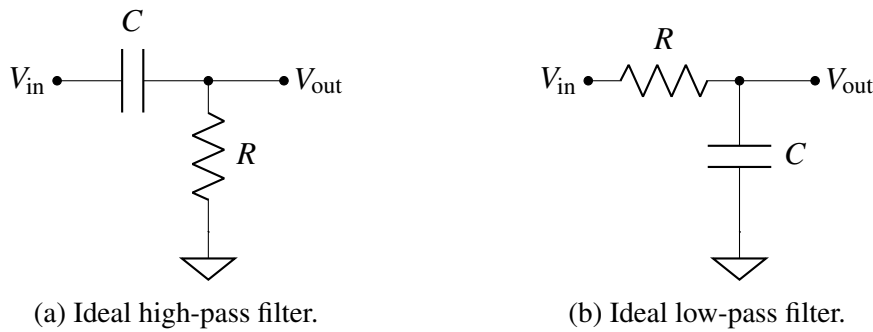
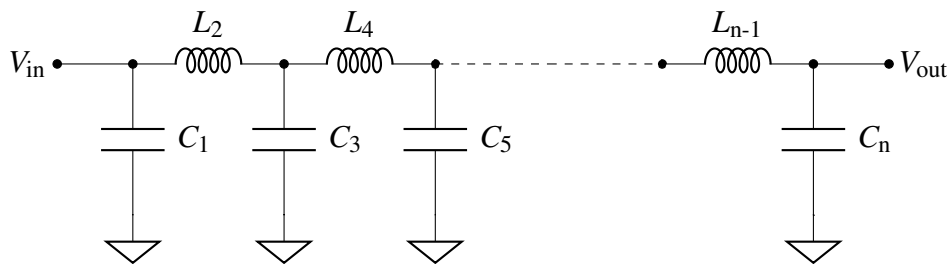


Figure 3.11 Electric schematics of ideal single pole filters.

Figure 3.12 A typical Butterworth low-pass filter of order n (n odd) in π configuration.

a capacitance and can be described analytically by the following complex transfer functions

$$G(f) = \frac{V_{\text{out}}}{V_{\text{in}}} \quad [20]$$

$$G_{\text{high}}(f) = \frac{i2\pi fRC}{1 + i2\pi fRC} \quad (3.38)$$

$$G_{\text{low}}(f) = \frac{1}{1 + i2\pi fRC} \quad (3.39)$$

respectively for high and low pass band. Low-pass Butterworth filters, shown in Figure 3.12 are inductive-capacitive filters and are designed in order to obtain a frequency response as flat and sharp as possible[20]. Two different configurations exist: T and π . In a T Butterworth filter the first element is an inductance, while in a π filter the first element is a capacitance. The choice of a configuration or the other is strictly related to circuit characteristics, for example π configuration may be preferable when load impedance is much lower than source impedance, while T configuration is better in the opposite case, so when load impedance is higher than signal impedance. The complex transfer function can be easily written using approximated real coefficients and depends from the number of poles constituting the filter. As the order of the filter, that is the number of poles, increases we have:

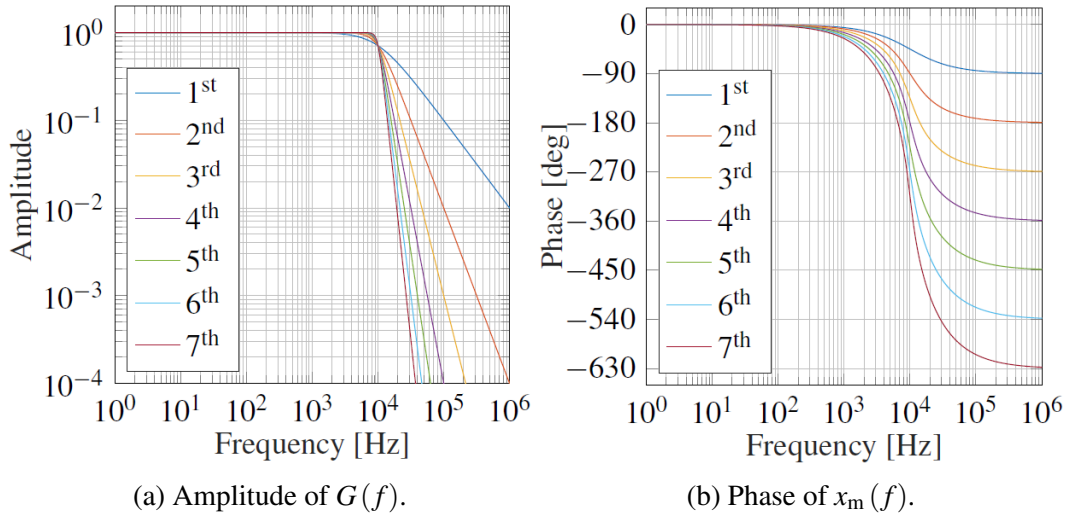


Figure 3.13 Amplitude and phase of $G(f)$ of ideal Butterworth low-pass filters for the first 7 orders.

$$G(f) = \begin{cases} \frac{G_0}{a+1} & 1^{\text{st}} \text{ order} & (3.40a) \\ \frac{G_0}{a^2+1.4142a+1} & 2^{\text{nd}} \text{ order} & (3.40b) \\ \frac{G_0}{(a+1)(a^2+a+1)} & 3^{\text{rd}} \text{ order} & (3.40c) \\ \frac{G_0}{(a^2+0.7654a+1)(a^2+1.8478a+1)} & 4^{\text{th}} \text{ order} & (3.40d) \\ \frac{G_0}{(a+1)(a^2+0.6180a+1)(a^2+1.6180a+1)} & 5^{\text{th}} \text{ order} & (3.40e) \\ \frac{G_0}{(a^2+0.5176a+1)(a^2+1.4142a+1)(a^2+1.9319a+1)} & 6^{\text{th}} \text{ order} & (3.40f) \\ \frac{G_0}{(a+1)(a^2+0.4450a+1)(a^2+1.2470a+1)(a^2+1.8019a+1)} & 7^{\text{th}} \text{ order} & (3.40g) \end{cases}$$

where G_0 is the amplitude at zero frequency, $a = i \frac{f}{f_c}$ and f_c is the cut frequency of the filter, defined as the frequency at which $\frac{G(f)}{G_0} = -3\text{dB}$. Amplitude and phase of $G(f)$ for different orders are shown in Figure 3.13. It is clear from the figure that the frequency cut is characterized by high sharpness and increases with order of the filter.

3.5.2 Circuits with operational amplifiers

Operational amplifiers, also known as Op-Amps, are widely diffused electronic devices used in a large variety of circuits, including our servo stage. Op-Amps behavior is defined by two Golden Rules[20]:

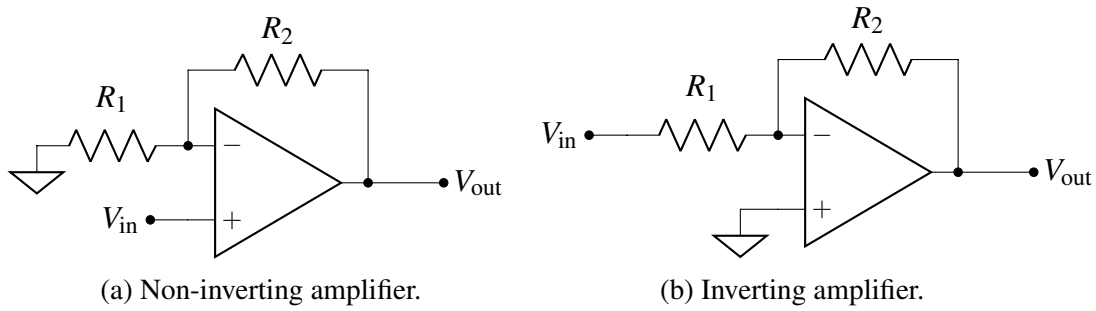


Figure 3.14 Electric schematics of typical ideal non-inverting and inverting amplifiers.

- The output attempts to do whatever is necessary to make the voltage difference between the inputs zero
- The inputs draw no current

In addition to these points, other important features of ideal operational amplifiers are the infinite input impedance, the null output impedance and the infinite bandwidth. Fundamental features and golden rules can vary from the ideal case to the reality. As an example, a voltage difference of a fraction of millivolt is present between the inputs and a little input current is present (on the order of few pico Ampère), but these contribution can be considered negligible in the most of cases and ideal rules are so valid. Basic Op-Amps circuits can be used to amplify a signal in non-inverting or inverting configuration. Two typical schemes adopted for this purpose are sketched in Figure 3.14. The complex transfer functions can be directly derived from the golden rules and their expressions for the ideal non-inverting and inverting amplifiers are respectively [20]

$$G_{\text{non-inverting}} = 1 + \frac{R_2}{R_1} \quad (3.41)$$

$$G_{\text{inverting}} = -\frac{R_2}{R_1} \quad (3.42)$$

It is worth noting that the input and output impedances of the non-inverting amplifier are given by $Z_{\text{input}} = \infty$ and $Z_{\text{output}} = 0$ respectively, while in the inverting amplifier we have $Z_{\text{input}} = R_1$ for the input and $Z_{\text{output}} = 0$ for the output.

Another useful application of the operational amplifier is the integrator circuit, which is one of the fundamental components of the feedback system used in this thesis work. The typical scheme of this circuit is shown in Figure 3.15. The scheme is similar to inverting amplifier, so, to find out the analytic expression for the complex gain function we have to

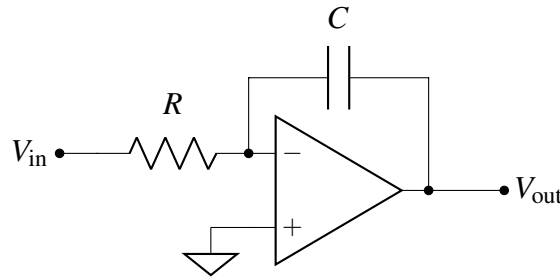


Figure 3.15 Electric schematic of a typical inverting integrator.

equate the current flows through R and C . So we have

$$\frac{V_{in}}{R} = -C \frac{dV_{out}}{dt}$$

and thus

$$V_{out} = -\frac{1}{RC} \int V_{in} dt + \text{constant}$$

which is the integral of the input signal. So, the complex transfer function associated to the inverting integrator can be calculated as [20]

$$G_{\text{inverting}}(f) = -\frac{1}{i2\pi f RC} \quad (3.43)$$

Until now we have assumed that operational amplifiers were ideal, but in experimental setups some non-ideal effects have to be considered. The only non-negligible effect that we had to deal with is related to the bandwidth of the operational amplifier, which is limited and in first approximation can be modeled as single pole limited [20] and it is not infinite as in the ideal case. The non-ideal complex transfer function can be written as

$$A(f) = \frac{A_0}{1 + i\frac{f}{f_p}}$$

Where A_0 is the open loop gain at zero frequency, while f_p is the frequency of the pole, defined as the frequency where amplitude becomes -3dB with respect to A_0 .

When the loop is closed and the feedback is purely resistive, so the feedback is frequency independent, the effect of the real operational amplifier leads to a simple expression of the gain [20]

$$G(f) = \frac{G_0}{1 + i\frac{f}{f_p}}$$

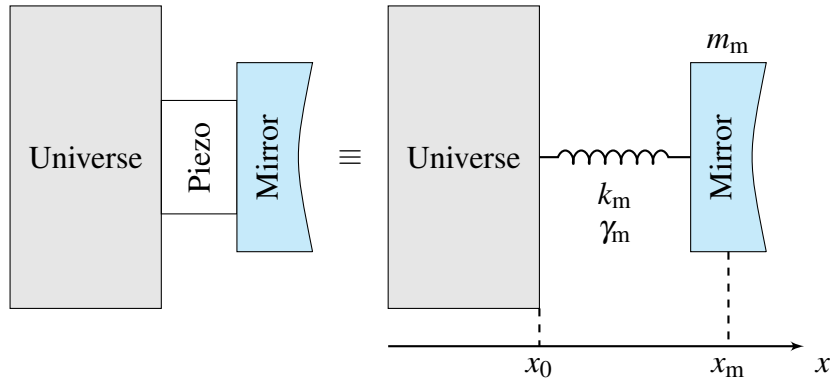


Figure 3.16 Scheme of the actuator modeled as a little mass m_m (piezoelectric and mirror) attached to a big mass (the universe), which is considered infinite with respect to the first one. The harmonic oscillator associated to this system is represented by the spring constant k_m and the damping constant γ_m .

where G_0 is the gain of the feedback (for example $-\frac{R_2}{R_1}$ for the inverting amplifier) and f_p is its bandwidth with close loop. This can be easily calculated assuming that the so called *Gain–BandWidth Product* (GBWP) is constant⁵. We simply have

$$f_p = \frac{GBWP}{G_0}$$

3.6 Actuator: harmonic oscillator model

The actuator is the part of the feedback system which is able to read the error signal generated with Pound-Drever-Hall technique and properly modified by the servo and to apply it to the cavity, in order to correct its resonance frequency and follow the external reference. It consists of two main parts: one of the cavity mirrors and a piezoelectric crystal attached to it, which stretches and contracts in response to the signal coming from servo. Hence, it moves the mirror modifying the cavity length and thus converting the signal into an optical frequency. This kind of system can be modeled as a series of driven damped harmonic oscillators, each of which represents a different connection between two components[21]. At a first step we introduce just one harmonic oscillator representing the piezoelectric, that is the connection between the mirror and the optical table, as shown in Figure 3.16. In particular we can consider the optical table having an infinite mass respect to the other parts of the physical system and we call it *Universe*. The equation of motion of this kind of system is

⁵The GBWP is defined simply as the product of the gain and the bandwidth. The GBWP of an operational amplifier is usually given on the datasheet.

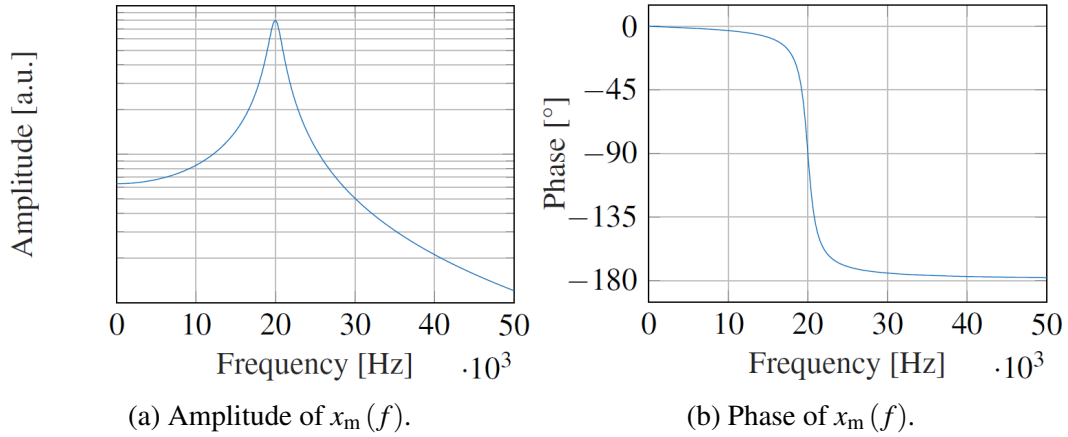


Figure 3.17 Amplitude and phase of $x_m(f)$ for a single harmonic oscillator with a resonance frequency of 20kHz, where we have used the typical values $\gamma_m = 100 \text{ kg s}^{-1}$ and $m_m = 10 \text{ g}$.

given by

$$F_m(t) = m_m \ddot{x}_m(t) - \gamma_m \dot{x}_m(t) + k_m(x_m(t) - x_0) \quad (3.44)$$

where $x_m(t)$ is the position of the mirror as a function of the time, $F_m(t)$ is an external driving force applied to the mirror by means of the piezoelectric, m_m is the mass of the mirror and the piezoelectric, k_m and γ_m are respectively the spring constant and the damping constant associated to the piezoelectric while x_0 is the rest position of the mirror. One can solve Equation 3.44 for $x_m(f)$ by Fourier transforming and using the property that $\mathfrak{F}(\dot{g}(t)) = i\omega \mathfrak{F}(g(t))$, so that the results is [21]

$$x_m(\omega) = \frac{F_m(\omega)}{m_m \omega_0^2 - m_m \omega^2 - i \gamma_m \omega} \quad (3.45)$$

where ω is a pulsation, related to frequencies by $\omega = 2\pi f$, then the resonance frequency $\omega_0 = \frac{1}{2\pi} \sqrt{\frac{k_m}{m_m}} = \frac{1}{2\pi} f_0$, with f_0 resonance frequency of the system. From the last formula directly follow the amplitude of the system response and its phase.

The trends of the amplitude and phase of $x_m(f)$ are shown in Figure 3.17. It is important to note that near the resonance phase delay increases rapidly, limiting the control system bandwidth to a value under the resonance frequency.

It is possible to make a more realistic (but more complex) description of the actuator taking into account the mirror actually is not directly attached to an infinite mass [21]. It can be done adding a counterweight between the mirror and the table (which has again an infinite mass, the *Universe*), so that the system can be described as two harmonic oscillators in series, as shown in Figure 3.18. We have two coupled equations of motion for the mirror

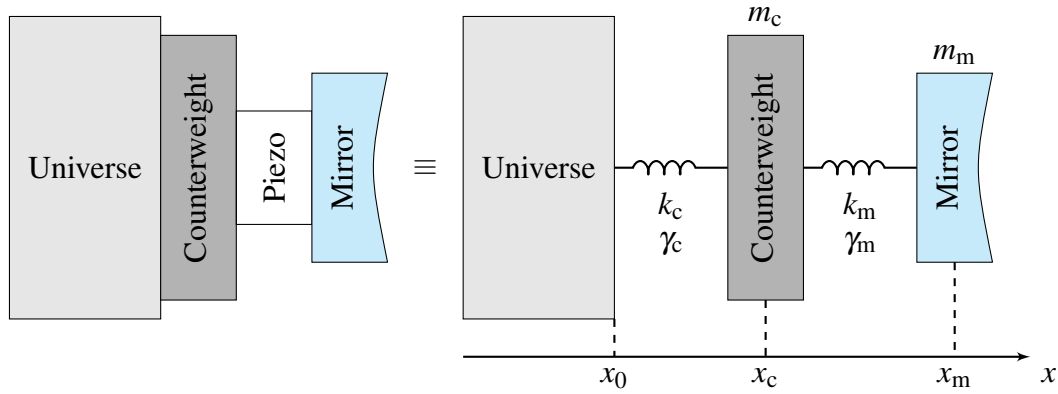


Figure 3.18 Scheme of the actuator modeled as a little mass m_m (piezoelectric and mirror) attached to another mass m_c (the counterweight) attached to a big mass (the optical table), which is considered infinite. The two harmonic oscillators associated to this system are represented by the spring constant k_m and the damping constant γ_m of the piezoelectric and by the spring constant k_c and the damping constant γ_c of the counterweight.

and the counterweight respectively

$$F_m(t) = m_m \ddot{x}_m(t) - \gamma_m \dot{x}_m(t) + k_m ((x_m(t) - x_0) - (x_c(t) - x_0))$$

$$F_c(t) = m_c \ddot{x}_c(t) - \gamma_c \dot{x}_c(t) - \gamma_m \dot{x}_c(t) + k_c (x_c(t) - x_0) - k_m ((x_m(t) - x_0) - (x_c(t) - x_0))$$

where the new terms k_c and γ_c are the respectively the spring constant and the damping constant of the connection between the counterweight and the Universe and are different from k_m and γ_m . Since the external force can be generated only by the piezoelectric, we can place $F_c = 0$. The two coupled equations set can be solved for $x_m(f)$, obtaining [21]

$$x_m(f) = \frac{F_m(f)}{-m_m (2\pi f)^2 - i2\pi\gamma_m f + k_m \frac{-(2\pi f)^2 m_c - i2\pi f (\gamma_c + \gamma_m) + k_c}{-(2\pi f)^2 m_c - i2\pi f (\gamma_c + \gamma_m) + k_c + k_m}} \quad (3.46)$$

Amplitude and phase of $x_m(f)$ are shown in Figure 3.19. Notice that the counterweight could introduce another resonance, which would further limit the control bandwidth of the system. It is worth to consider that a real actuator system often has more than one or two resonances, so the introduction of the counterweight does not completely solve the problem of modeling the system.

A way to improve the control bandwidth is to increase k_m , because this leads to an increase of f_0 (remembering that $f_0 = \sqrt{\frac{k_m}{m_m}}$) and so of the bandwidth. This can be done for example with the so called *preloading*, which consists of clamping the piezoelectric and the mirror assembly in order to increase the mechanical tension over the first one, placing an

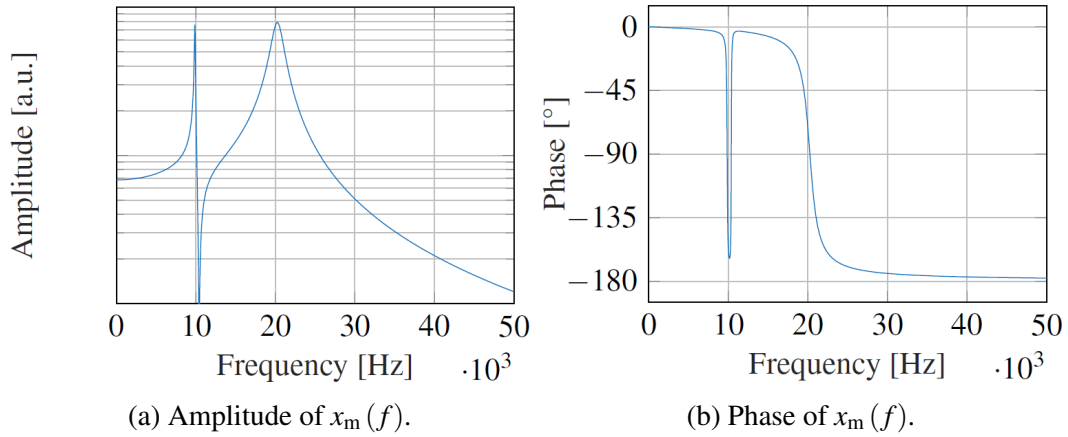


Figure 3.19 Amplitude and phase of $x_m(f)$ for two harmonic oscillators in series, with resonance frequencies of 20kHz and 10kHz, where we have used the typical values $\gamma_m = 100\text{kg s}^{-1}$, $m_m = 10\text{g}$, $\gamma_c = 100\text{kg s}^{-1}$ and $m_c = 500\text{g}$.

O-Ring between the mirror and the clamp. In this configuration, additional terms are summed to k and γ : $k = k_m + k_{\text{pre}}$ and $\gamma = \gamma_m + \gamma_{\text{pre}}$. The equations of motion in the two cases of single oscillator are trivial, indeed it is sufficient to make the substitution $k_m \rightarrow k_m + k_{\text{pre}}$ and $\gamma_m \rightarrow \gamma_m + \gamma_{\text{pre}}$. Then is evident that increases k ampliate the control bandwidth of the actuator system, as can be see clearly in Figure 3.20, where amplitude and phase of $x_m(f)$ are shown for different theoretical values of the preload in the case of single harmonic oscillator.

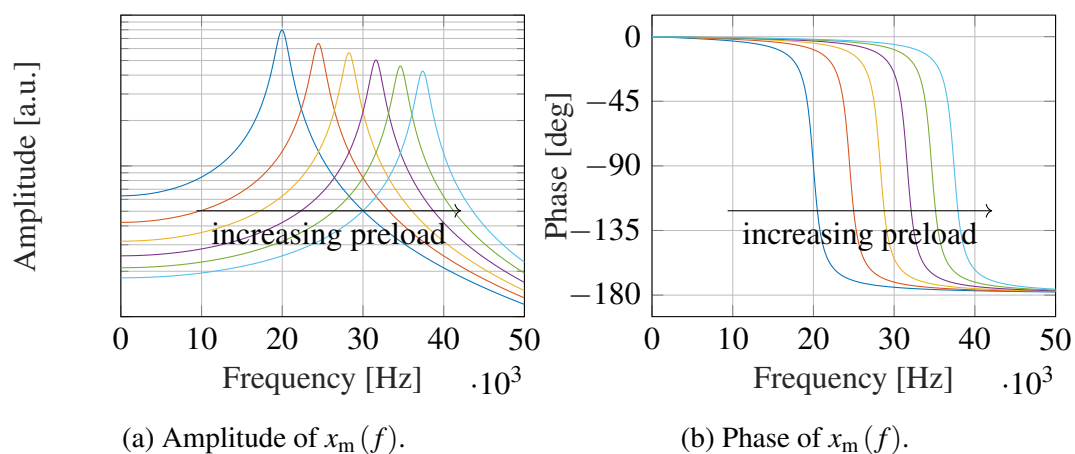


Figure 3.20 Amplitude and phase of $x_m(f)$ for a single harmonic oscillator with preloading. Here we can notice that the resonance frequency moves to higher values as we increase the preload (see the arrows in the two graphs), but the amplitude peak decreases and so the dynamic of the piezoelectric.

Chapter 4

Experimental setup

In this chapter we will describe the experimental setup used in this thesis work. Firstly, the whole apparatus will be introduced, then a description of the laser source and the optical cavity characterization will be performed, while the detailed description of the feedback system will be left to the next chapter.

4.1 Global layout

The experimental setup consists of three main parts: the laser line that lead the light beam to the Fabry-Perot cavity, the optical cavity and the feedback system. The general layout scheme of the apparatus is shown in Figure 4.1. We will explain the feedback system and the stability experimental results in detail in the next chapter, while the other parts of the experimental setup will be treated in this chapter. The laser line is fundamental to adequately manipulate the laser beam before the coupling with the optical cavity. In particular, the path to the cavity is formed by optical components that changes polarization, dimension, divergence and spectral width of the laser beam. The laser beam is produced in a Menlo Orange Oscillator horizontally polarized. The output laser light then encounters a waveplate that rotates the polarization of $\pi/2$ and a two lenses system that allows to focus the beam and (after the second lens) to re-collimate it. In the point of minimum beam width is positioned an Electro-Optical Modulator which is part of the feedback system. After the second lens the laser beam pass through another waveplate that restores the horizontal polarization. Then the light is sent to a *4-f spatial filter* that selects a 2 nm wide spectrum. The beam leaving the *4-f* is sent to a mirror that changes the direction and allows it to enter inside a two lenses telescope that adjusts the beam dimension in order to obtain a better matching with fundamental cavity mode. Using two consecutive mirrors the beam is sent inside the cavity, which is formed by four fused silica mirrors. The third and fourth mirrors are mounted on

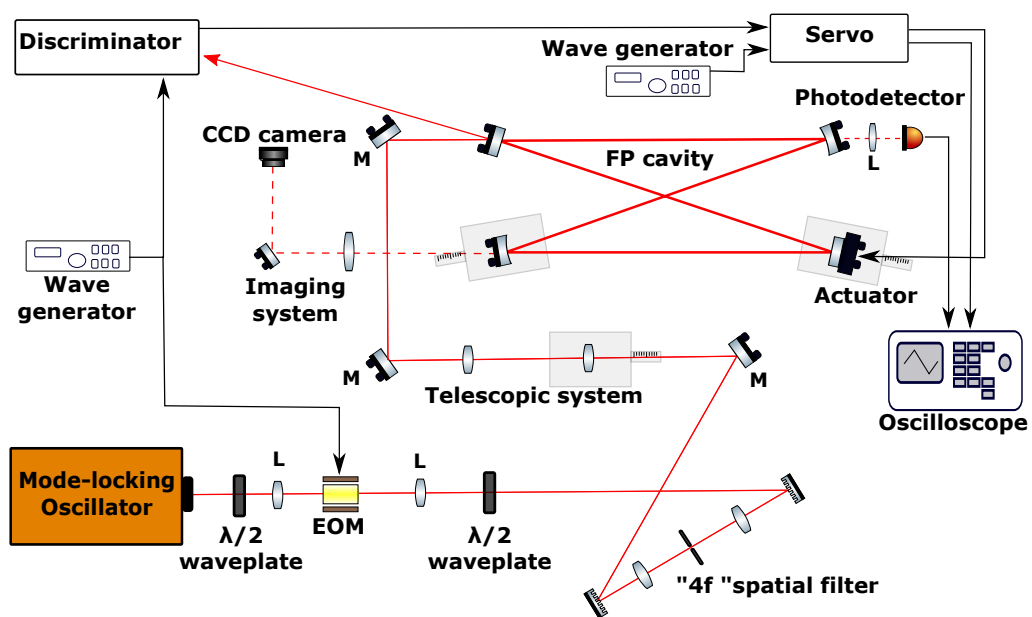


Figure 4.1 Experimental setup scheme. Main components names are explicitly shown, while lenses and mirrors are labeled L and M respectively.

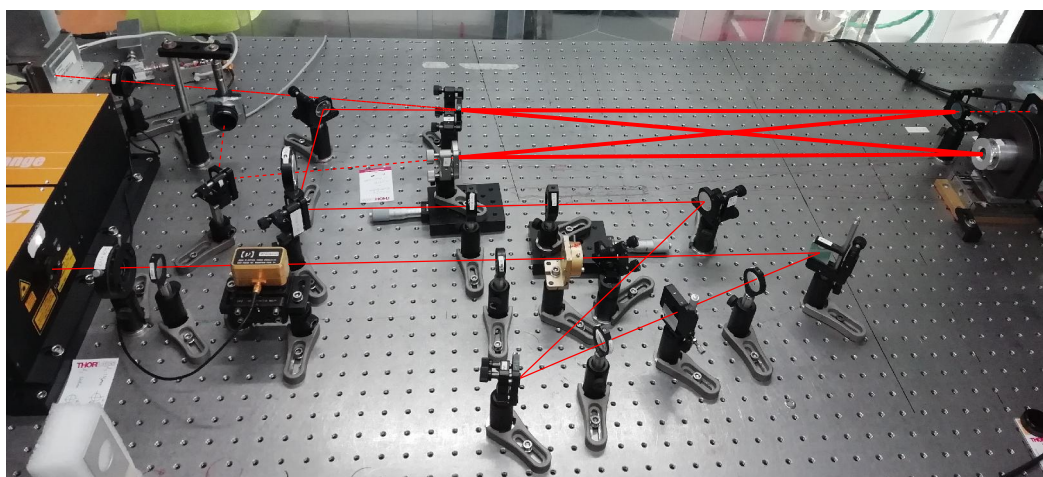


Figure 4.2 The experimental setup photographed in laboratory. The laser path is highlighted in red.

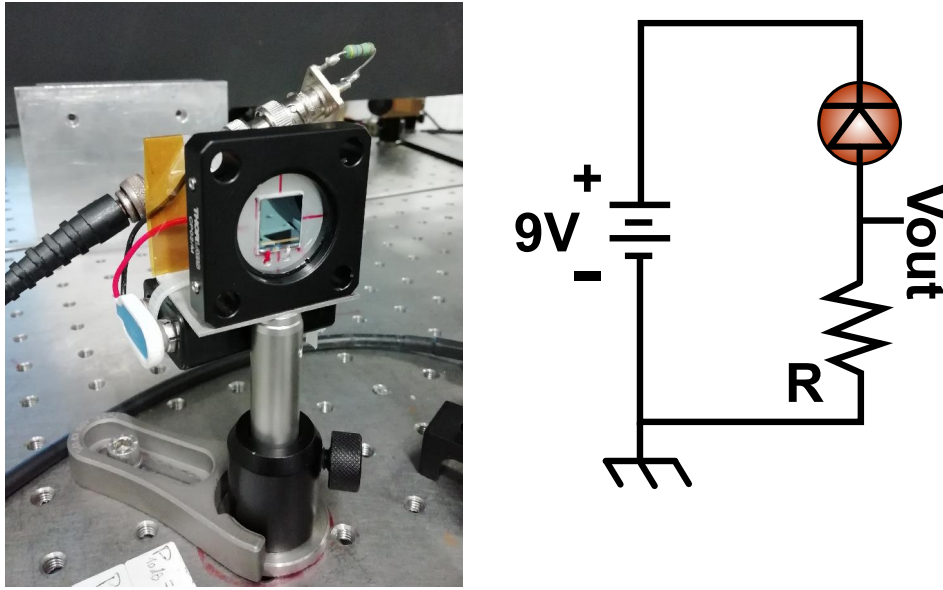


Figure 4.3 Picture and electrical schematics of the photodetector in our experimental setup.

micrometric slide that allows a precise control over their position. Moreover, the third mirror is also controlled by a piezoelectric crystal which acts as Actuator of the feedback system. Not all the incident radiation can enter inside the cavity: most of it is reflected and goes on the feedback system Discriminator that is connected to the Servo. Then the beam reflected by the first mirror of the cavity plays a crucial role in the stabilization of the cavity itself. If the resonator and the laser are in resonance, part of the radiation is transmitted outside the cavity through the mirrors and can be exploited to obtain informations like the power inside the cavity or the frequency detuning between laser and cavity. In particular, the beam outgoing from the second mirror of the cavity is sent to a photodetector made with a FDS1010 Si photodiode and a 470Ω resistance, as shown in Figure 4.3.

The photodetector signal can be read by an oscilloscope like in our case, where we used a LeCroy 9360 oscilloscope to perform all the measurements. Here we have to highlight that talking about voltage or power of the signal is essentially the same thing, because these quantities are related in our photodetector linearly, since

$$P = V \frac{1}{\eta R} \quad (4.1)$$

where $\eta = 0.638 \frac{\text{A}}{\text{W}}$ is the responsivity of FDS1010 photodiode at $\lambda = 1030 \text{ nm}$ and $R = 470\Omega$. Then, it will occur that in next sections we will refer to power or voltage indiscriminately in non-measleading cases. Also the transmission signal outgoing from the third cavity mirror has been exploited for measures: using an imaging system and a CCD camera it is possible

to estimate the spot dimension and shape on the mirror and the waist dimension in the cavity focus. It is important to note that the laser source power is variable in function of pump diodes electric current and amplification diodes electric current. We have defined the standard conditions for the measures performed during this thesis work looking for the best compromise between good power level and risks of Q-switch phenomenon. Such conditions correspond to a pump diode current of 507 mA and an amplification diodes current of 800 mA.

4.2 Laser source

As previously explained, the laser beam is manipulated in order to reach a better coupling with the optical cavity. Its features has been experimentally characterized for what concerns temporal (hence spectral) properties, shape and intensity noise.

4.2.1 Spectral and temporal properties

In order to obtain a better matching between the laser beam and the cavity fundamental mode and reproduce the MariX experimental condition in which the light pulses spectrum will be 2 nm wide, a spectral selection has been performed. In Figure 4.4 are shown respectively the spectrum before and after the spectral selection, experimentally acquired using a commercial available Thorlabs OSA Spectrum Analyzer with 1 nm resolution.

Such selection is achieved using a so called *4-f spatial filter*, which is composed of two 1200 lines/mm diffraction gratings, two lenses with focal length equal to 100 mm and a slit. The incoming laser beam is reflected by the first diffraction grating that spatially separates the spectrum components. After the spectral separation the light is collimate and selected in frequency by the first lens and the slit. Since the angle of incidence is equal to 22° , the 2 nm wide spectrum can be selected by a 0.46 mm wide slit. The second lens recomposes the beam on the second grating and the laser pulse then leaves the *4-f filter*. The name *4-f* is related to the distance of the optical components which are all equal to f , namely the focal length of the two lenses.

In terms of power, the spectral selection lead to a reduction of a factor ten, because of the cut on frequencies, but also because of inefficiency of the diffraction gratings. Indeed, their efficiency is dependent from polarization, angle of incidence (in our case maximized at 35 degrees), wavelength and other factors and about the 40% of radiation is lost.

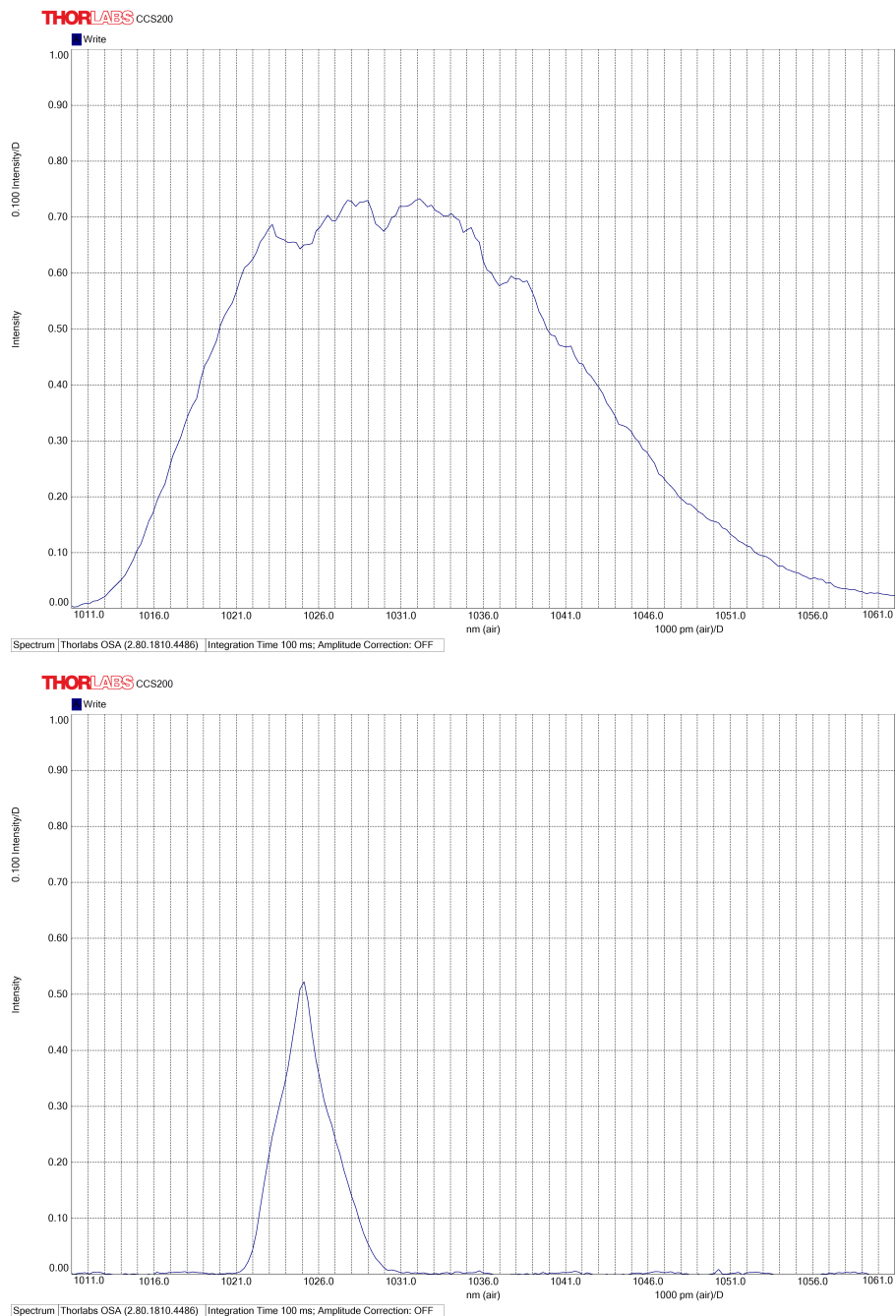


Figure 4.4 *Above*: light beam spectrum before the spectral selection. Note that it is about 35 nm wide and centered around 1030 nm. *Below*: light beam spectrum after the spectral selection performed by the slit. Here the spectrum is about 2 nm wide and centered around 1025 nm.

From the temporal point of view, the spectral selection causes a pulse broadening. Since the initial spectrum is 26 nm wide, the pulse length is less than 200 fs¹ and it is strongly influenced by the settings of the compressor inside the commercial Menlo apparatus. But if the spectrum is reduced to only 2.5 nm, then the pulse temporal can be elongated on the order of 0.5 ps and the compressor is no longer dominant. This value can be estimated starting from the Gaussian spectral profile and supposing we are in *transform limit* condition:

$$A(\omega) = e^{-\frac{\omega^2}{\Delta^2}} \longrightarrow A(t) = e^{-\frac{\Delta^2}{4} t^2}$$

where $\Delta = FWHM/1.177$ and $\omega = 2\pi\nu$. Then the intensity is

$$I(t) \propto e^{-\frac{\Delta^2}{2} t^2} = e^{-\frac{2t^2}{\tau}}$$

Hence

$$\frac{\tau^2}{2} = \frac{2}{\Delta^2} \longrightarrow \tau = \frac{2}{\Delta}$$

Then, recalling that $\Delta\omega = 2\pi \frac{c}{\lambda^2} \Delta\lambda$ and $\lambda \approx 1000 \text{ nm} = 10^{-6} \text{ m}$, approximating $\Delta\lambda$ with $2 \text{ nm} = 2 \cdot 10^{-9} \text{ m}$ and $\pi \cdot c$ with 10^9 m/s we can obtain an indicative pulse temporal length value:

$$\tau = \frac{2}{\Delta} = \frac{2}{2\pi \frac{c}{\lambda^2} \Delta\lambda} = \frac{\lambda^2}{\pi c \Delta\lambda} \approx \frac{10^{-12}}{10^{18} \Delta\lambda} \approx \frac{10^{-12}}{10^9 \cdot 2 \cdot 10^{-9}} \text{ s} \approx 0.5 \text{ ps} \quad (4.2)$$

4.2.2 Laser intensity noise

Intensity noise causes fluctuations of the laser power that directly affect the power inside the cavity. Laser intensity noise can be measured by a photodetector placed before the first cavity mirror; in this way the laser intensity noise can be decoupled from the noise introduced by the Fabry-Perot cavity. The photodiode can only record a voltage signal proportional to the incident power, then fluctuations on the voltage signal correspond to power (or intensity) fluctuations. From the photodiode signal is possible to calculate the Fourier transformation directly on the oscilloscope. Power Spectral Density calculation from the oscilloscope FFT data has been performed by a software written in LabView able to recognize the time interval and calculate $S_V(f)$. The measured spectrum is shown in Figure 4.5. The photodetector bandwidth is about 900 kHz, because the cut frequency is given by $f_{cut} = \frac{1}{2\pi RC}$, where the capacitance is 375 pF and resistance is 470 Ω in our case.

We can note a general decreasing behavior of the PSD for increasing frequencies. Four peaks stand out from the smooth background at frequencies that are approximately multiples

¹Data taken from Menlo Orange datasheet

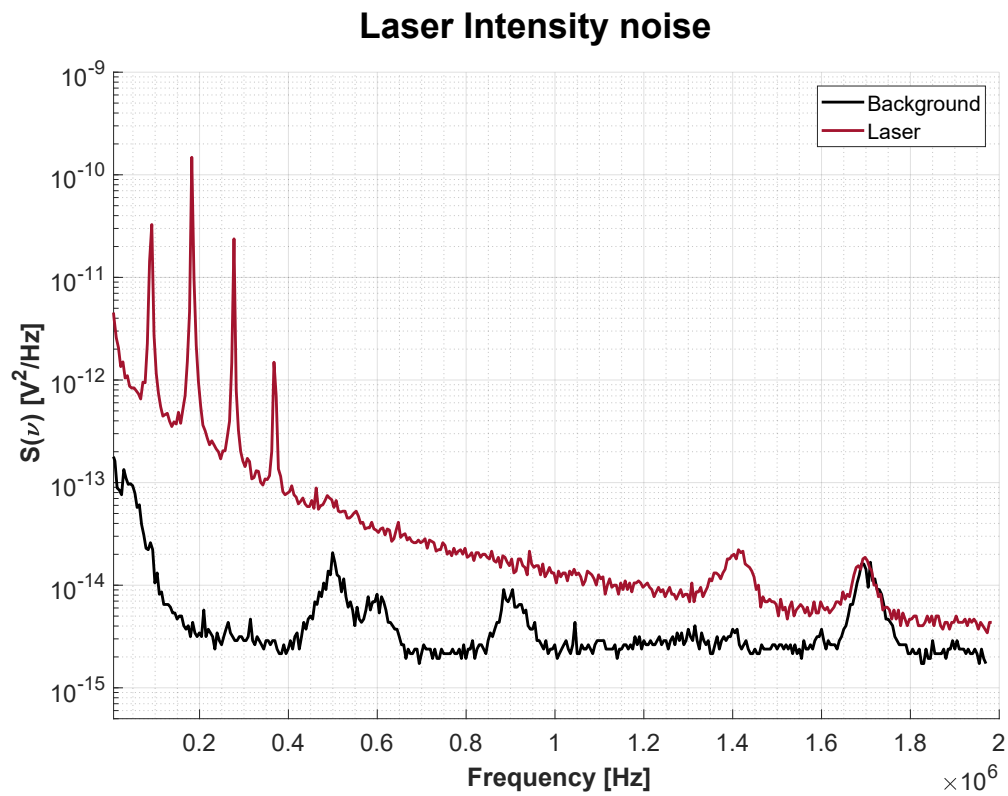


Figure 4.5 The intensity noise Power Spectral Density $S(\nu)$ of the Menlo Orange laser radiation is drawn in red, while the background noise (due to electronic components) is drawn in black. The noise contribution of the frequency range represented in figure is about $0.25V$, corresponding to a relative noise $\delta V = 0.039\%$.

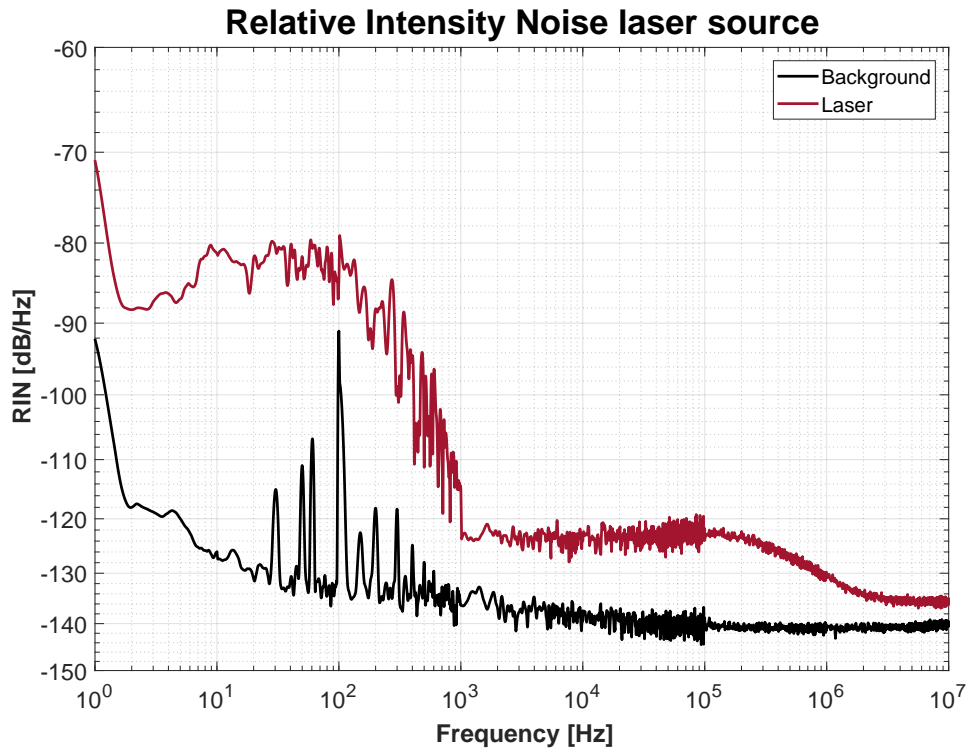


Figure 4.6 Relative intensity noise of Menlo Orange oscillator performed via spectrum analyzer at Politecnico di Milano.

of 90 kHz. Precisely, the peaks are located at 92.5 kHz, 182.5 kHz, 277.5 kHz and 367.5 kHz. Moreover, the frequencies of such peaks are independent from the pump diodes current and from the amplification diodes current of the Menlo Orange Oscillator. The noise obtained integrating from 0 Hz to 2 MHz is $\sigma = 1.2 \cdot 10^{-3} V$. Dividing this value by the mean value of laser voltage signal measured by the photodetector is equal to 3.14V, we obtain $\delta V = 0.039\%$. Such value is considerably lower than the MariX cavity power fluctuation requested limit of 2%, although all the spectrum should be considered, then the Orange laser is a good candidate to be part of the final experimental configuration.

We also performed a wide frequency range measurement at Dott. G. Galzerano's laboratory at Politecnico di Milano. Such measurement has been done using a Agilent Electronic Spectrum Analyzer. The laser beam has been sent directly to a photodetector connected to the ESA, firstly to measure the average incident power and then to measure the intensity fluctuations. The results are exposed in Figure 4.6, where the intensity noise is expressed in dB/Hz.

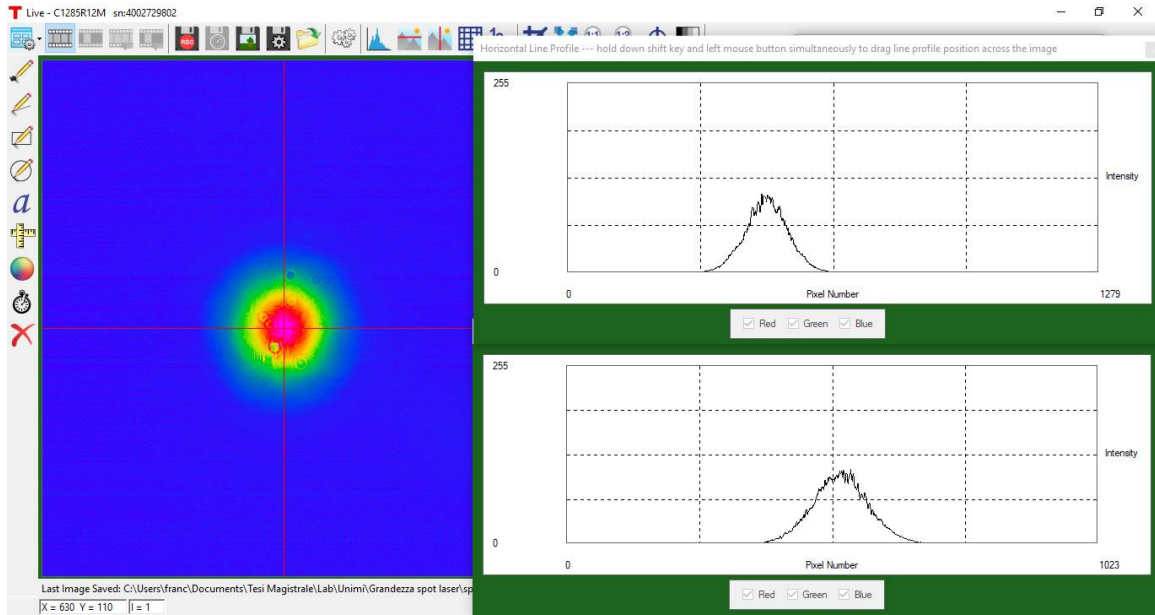


Figure 4.7 Example of beam radius measure: the screenshot shows the intensity profile on the vertical axis and on the horizontal axis.

4.2.3 Laser beam features

Fundamental parameters of a laser beam are certainly its dimension and intensity profile. In particular, the dimension of the cavity fundamental mode and of the incoming laser beam has to be as similar as possible in order to have a good cavity-laser mode coupling and avoid the presence of high order modes. We have directly measured the beam radius exploiting a Thorlabs CCD camera and *ThorCam* software. Such software allowed us to measure the beam FWHM, that is directly related to the beam radius as

$$w(z) = \frac{FWHM(z)}{\sqrt{2 \ln 2}}$$

where the Full Width Half Maximum in micrometers is calculated from the measured value in pixels multiplying by a factor $5.2 \frac{\mu m}{px}$. The relation written above is valid only for Gaussian beams, like the one generated by our Menlo Orange oscillator. A screenshot taken from ThorCam software used to measure the beam radius is shown in Figure 4.7. The output beam has been directly measured at the oscillator output at a distance $d_1 = 132$ mm and at a distance d_2 . We obtained values of $w_H = 472 \mu m$ on the horizontal axis and $w_V = 658 \mu m$ on the vertical axis in d_1 and values of $w_H = 725 \mu m$ on the horizontal axis and $w_V = 658 \mu m$ on the vertical axis in d_2 . The measured beam radius is about 2 times lower than the cavity fundamental mode dimension, so without any correction the mode coupling between laser

and cavity would be very bad. Moreover, the beam needs to be collimated when injected into the cavity. Then, in order to adequately manipulate dimension and divergence of the beam, two telescopic system has been implemented in the experimental setup before the light enters the Fabry Perot cavity. The first one is composed by a lens with a focal length of 100 mm and a lens with a focal length of 250 mm. This system allow us to enlarge the beam of a factor about 2.5 and to correct the divergence. A fine correction can be performed by a second telescopic system, positioned after the *4-f spatial filter* and made by two identical lenses with focal length equal to 100 mm. It is important to underline that the first lens is mounted on a micrometric slide with the aim of obtain a fine control on the magnification factor of telescope and beam divergence.

4.3 Optical cavity

The optical cavity realized in this thesis work is composed by four high-reflectivity mirrors disposed in the so called bow-tie configuration. In Figure 4.8 is drawn the Fabry-Perot scheme. The first cavity mirror is labeled *A* and it is a flat mirror. On this mirror the incoming external beam is injected inside the cavity and partially reflected on the feedback discriminator. The second mirror (labeled *B*) is a curved mirror with a nominal value of radius of curvature equal to 758 mm. Also the mirror *C* is curve, with a nominal radius of curvature of 750 mm and it is mounted on a micrometric slide, as the last mirror *D*. The last mirror is flat as the mirror *A*. Behind the mirror *D* is mounted a piezoelectric crystal: this is the Actuator of the feedback system and allows a very precise regulation of the position of the mirror. The total length of the cavity is fixed by the resonance condition, while the angles α and β are choosen in order to have the lowest angle of incidence between the electrons and photons permitted by mechanical requirements. In fact, since the electron pipeline will pass between mirrors *A* and *C*, it will go through the cavity and then it will pass between mirrors *B* and *D*, a distance about ten centimeters between such mirrors has been left. We measured the transmissivity of the mirrors in order to characterize them and estimate their reflectivity:

$$T_A = 1.27 \cdot 10^{-3} \quad T_B = 7.30 \cdot 10^{-4} \quad T_C = 3.34 \cdot 10^{-4} \quad T_D = 5.33 \cdot 10^{-4}$$

It is possible to estimate the reflectivity coefficients from the tansmissivity values, avoinding dispersion effects. If we define $R = (1 - T)$, we obtain

$$R_A = 0.9987 \quad R_B = 0.9993 \quad R_C = 0.9997 \quad R_D = 0.9994$$

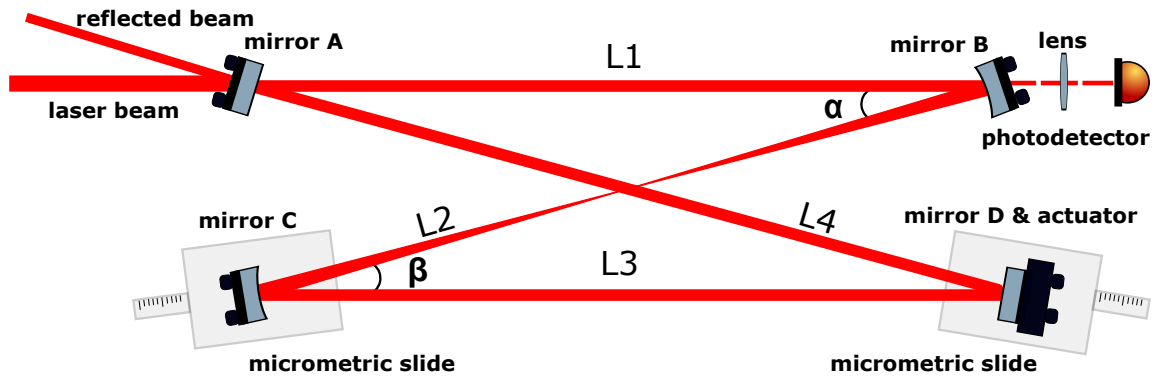


Figure 4.8 Fabry Perot cavity scheme where the laser beam is drawn in red. The first mirror is labeled *A*, the second is labeled *B*, while the third and fourth mirrors are labeled *C* and *D* respectively. The angle α has been experimentally measured and it is equal to 7.65 degrees, while $\beta = 6.27^\circ$.

Using this method we overestimate the reflectivity values and their product $R_{TOT} = 0.9971$. From experimental cavity Finesse, we estimated a more reliable (and lower) total reflectivity value $R_{TOT} = 0.98676$. Although the nominal values of the radius of curvature of the two curved mirrors are known from the production company datasheet, these values have been experimentally measured in laboratory, thus obtaining 767 mm for mirror *C* and 741 mm for mirror *D*.

4.3.1 Cavity modes

As every stable resonator, the bow-tie Fabry-Perot cavity realized in this thesis work has precise solutions for the oscillating fields inside it, thus it has well-defined modes. Its planar nature leads to a break of the cylindrical symmetry, then our cavity presents Hermite-Gaussian modes. Exploiting an imaging system done by a 100 mm focal lens and a mirror, we can recreate the image of the spot on mirror *C* on the CCD camera. It is so possible to capture the whole modal structure of the resonant cavity changing the cavity length, therefore its resonance frequency, as we will explain in next Subsection. Examples of the low-order modes of the cavity are shown in Figure 4.9.

4.3.2 Cavity alignment and mode-matching procedure

A preliminary step in laser-cavity coupling is the external beam alignment and mode-matching to the cavity resonator and only when the system is properly coupled the stabilization is performed. Initially, the length of the cavity has to be chosen as to be equal to

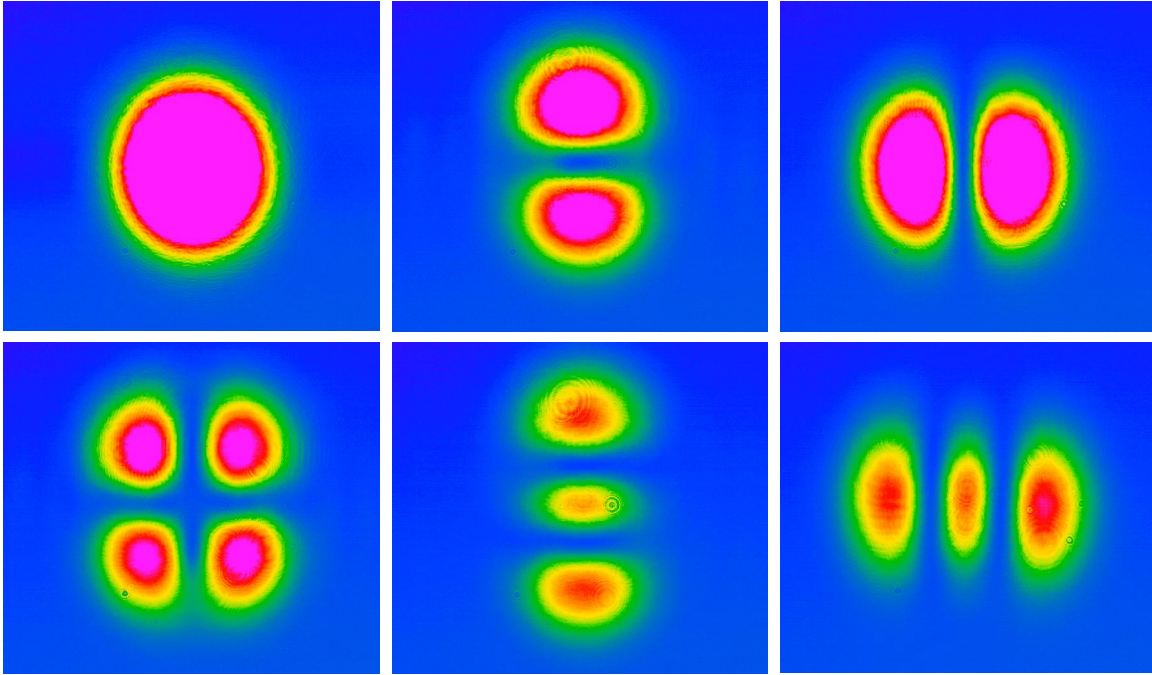


Figure 4.9 Hermite-Gaussian modes of our optical cavity. Images acquired by CCD camera.

$$L_C = c \tau_{rep}$$

where τ_{rep} is the mode-locking repetition rate of 10^{-8} seconds. Note that this condition is necessary only when the used laser is in pulsed regime, like in our case, but not in continuous wave regime, where the resonance condition is easier to satisfy. The resonance length can be precisely reached exploiting the micrometric slides of mirror C and D . Using a triangular wave signal sent on the actuator (directly or passing through the Servo) it is possible to scan the length of the cavity around the value of null voltage selected on wave generator: when voltage rises and falls, the piezoelectric crystal shortens and elongates the cavity length with a sub-micrometric sensibility. Indeed, assuming a linear response of the piezoelectric, we can write the cavity length as

$$L = L_0 + 2 \cdot \alpha_{piezo} \cdot \Delta V = L_0 + \delta L \quad (4.3)$$

where the factor 2 is necessary to consider the reduction of both L_3 and L_4 , while α_{piezo} is a coefficient such that a voltage difference of some Volts changes the cavity length on the order of the micrometer. When the peak-to-peak voltage of the triangular wave is enough to obtain $\delta L > \lambda_{laser}$ we can see more than one Free Spectral Range during the cavity scanion then all the resonating modes.

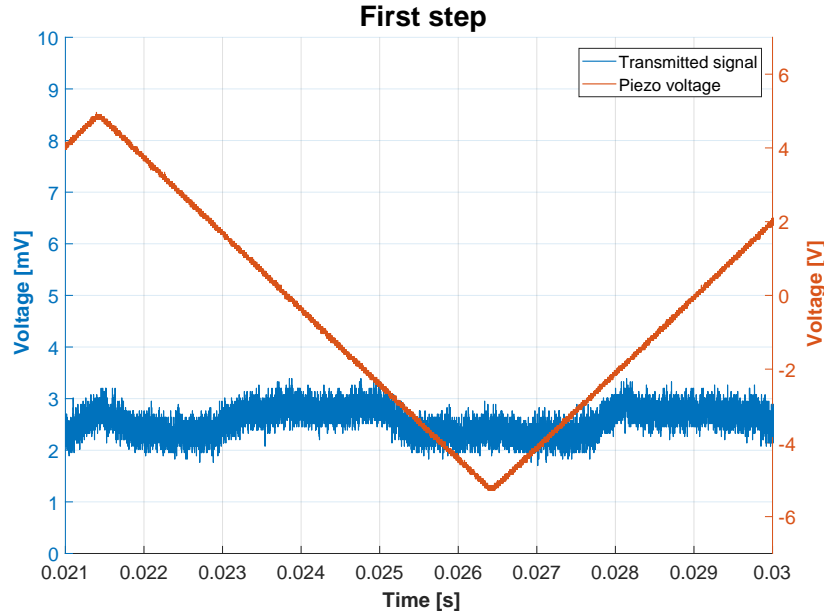


Figure 4.10 The voltage triangular wave sent to the piezo and the transmission signal are represented in figure. Here the cavity length is incorrect, then there is not resonance.

The transmitted signal measured by the photodetector after mirror B during the triangular wave cycle can be used to monitorate the cavity-laser coupling. The first steps (so the cavity length correction procedure) seen from the oscilloscope are shown in Figures 4.10, 4.11 and 4.12. When the resonance length has been reached, many modes are present within a FSR. In order to obtain a perfect matching between the incoming gaussian beam and the fundamental mode of the cavity, it is necessary to avoid misallignement and mode mismatching. Mismatching occurs when the incoming beam has a different dimension from the cavity fundamental mode one or when the waist axial position is incorrect. On the other hand, misallignement occurs when the incoming beam is shifted from the cavity centre or when the incidence angle is non-zero respect to the cavity mode axis. This fact can be theoretically shown[22] writing the incoming laser beam wavefunction $\Psi(x)$ as a superposition of the cavity modes $U_{m,n}(x)$ (in cartesian coordinates) or in terms of the radial modes $V_p(r)$. The ideal situation is the one in which $\Psi(x)$ perfectly matches the cavity fundamental mode, then we have perfect allignement and mode-matching. It can be shown that misallignement and mismatching lead to different expansions of $\Psi(x)$ as a sum of the fundamental cavity mode $U_0(x)$ or $V_{l,m}(r)$ and higher-order factors. In particular, if we define $k = p + q$ in cartesian coordinates and $k = l + 2m$ in radial coordiantes, we find out that misallignement is responsable of the presence in our cavity of *odd* k Hermite-Gaussian

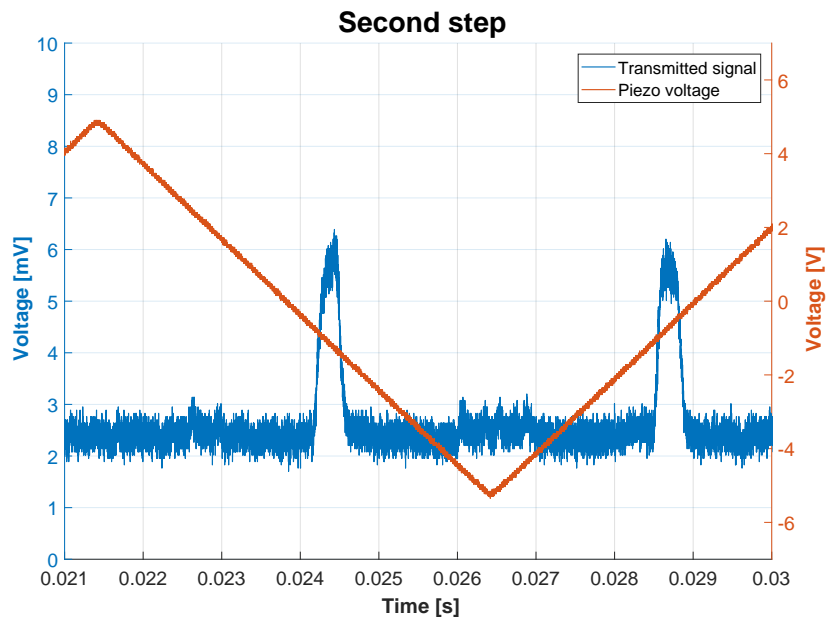


Figure 4.11 The cavity length is near the right one, then transmission peaks appear.

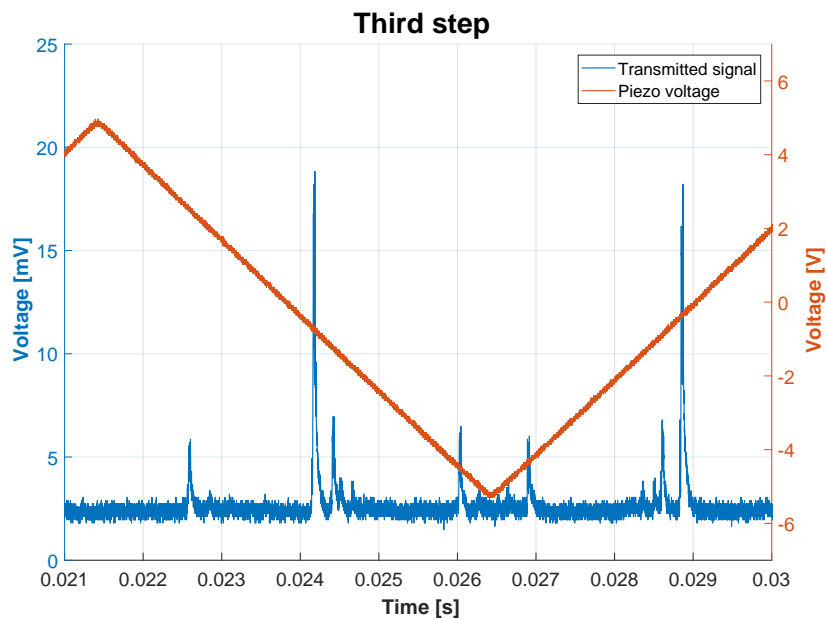


Figure 4.12 Cavity in resonance. The higher peaks correspond to the fundamental mode, the peaks immediately near to it are second-order modes, while the standing alone modes are first-order modes

modes in $\Psi(x)$ expansion like $TEM_{0,1}$ and $TEM_{0,1}$, while mismatching causes the arise of *even* k Hermite-Gaussian modes such as $TEM_{2,0}$ or $TEM_{0,2}$. If we define the cartesian fundamental mode

$$U_0(x) = \left(\frac{2}{\pi w_0^2}\right)^{1/4} \exp\left(-\left(\frac{x}{w_0}\right)^2\right)$$

and the first off-axis mode

$$U_1(x) = \left(\frac{2}{\pi w_0^2}\right)^{1/4} \frac{2x}{w_0} \exp\left(-\left(\frac{x}{w_0}\right)^2\right)$$

we can for example demonstrate the effect of a misalignment due to a shift a_x of $\Psi(x)$ respect to $U_0(x)$, namely

$$\Psi(x) = A U_0(x - a_x) = A \left(\frac{2}{\pi w_0^2}\right)^{1/4} \exp\left(-\frac{(x - a_x)^2}{w_0^2}\right) \quad (4.4)$$

if $a_x \ll w_0$ we can expand Equation 4.4 as

$$\Psi(x) \approx A \left[U_0(x) + \frac{a_x}{w_0} U_1(x) \right] \quad (4.5)$$

So a translational misalignment introduces a first order non-fundamental mode, correspondent to an odd value of k . It can be also shown that that in case of small difference between beam waist dimension and cavity waist size, hence in the case of mode mismatching due to $w_0' = w_0(1 + \varepsilon)$, we can write the incoming beam in radial coordinates as a superposition of the fundamental mode and the the lowest non-fundamental radial mode ($l = 0, m = 1$) as

$$\Psi(r) \approx A [V_0(r) + \varepsilon V_1(r)] \quad (4.6)$$

Since in radial coordinates $k = l + 2p$, the mode mismatching is associated to the raise of even k modes. Many different examples of misalignment and mode mosmaching exist, but they all lead to odd and even k respectively as in the cases taken in account above [22]. Considering that our goal is to have $\Psi(x) = U_0(x)$ in our experimental system, we must correct misalignment and mode mismatching conditions. We can reduce the laser beam shift and angle of incidence using two mirror positioned before the first mirror of the cavity, while mismatching effects can be reduced by the telescopic system posed after the *4-f spatial filter*. Figure 4.13 shows a screenshot from the oscilloscope in which, after allignment optimization, $TEM_{0,1}$ and $TEM_{1,0}$ have been deleted. Figure4.14 shows the modal structure

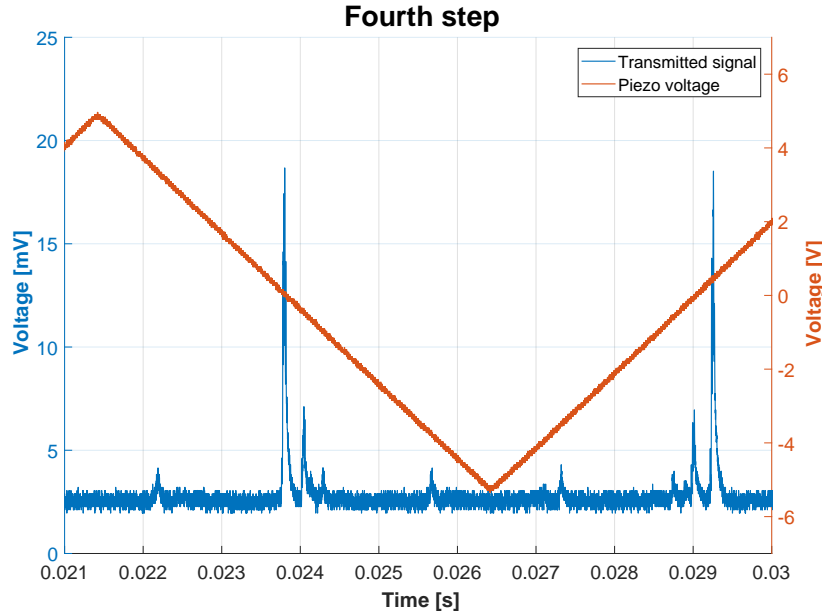


Figure 4.13 After misalignment correction only $TEM_{0,0}$ and even k modes survive.

after mismatching correction: only fundamental mode is visible (higher order modes have been suppressed or strongly reduced).

4.3.3 Cavity Finesse

Cavity Finesse is a fundamental parameter of a resonator. Especially for MariX application as Compton X-Ray source Finesse is very important, since the power gain is directly related to it as we have already demonstrate in Subsection 3.3. Finesse of the cavity used in this work has been measured acquiring data from the oscilloscope and exploiting the transmitted signal on the photodetector. Again triangular wave has been sent to the actuator, in order change cavity length and scan more than a Free Spectral Range and then see more than one fundamental mode peak as shown in Figure4.15.

The temporal distance between two $TEM_{0,0}$ has been measured and divided by the time corresponding to the FWHM of the higher peak in the scansion, so obtaining the Finesse value by $F = \frac{\tau_{FSR}}{\tau_{FWHM}}$. To gain precision in measurement it is also possible to change the temporal scale of the oscilloscope. It is here important to note that the scan frequency could ruin the measures, indeed for fast scanning (like at 200 Hz or 100 Hz) the peak is low in power and asymmetric because the cavity characteristic time is not enough lower than the transmission peak temporal width. In particular, the characteristic time τ_c is on the order of 10^{-6} seconds

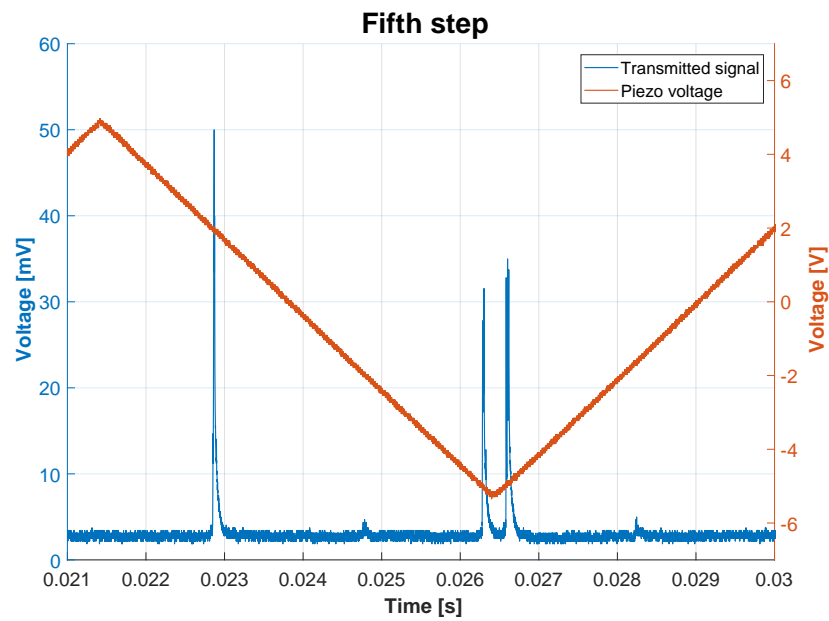


Figure 4.14 After mismatching adjustments $TEM_{2,0}$ and $TEM_{0,2}$ power is strongly reduced.

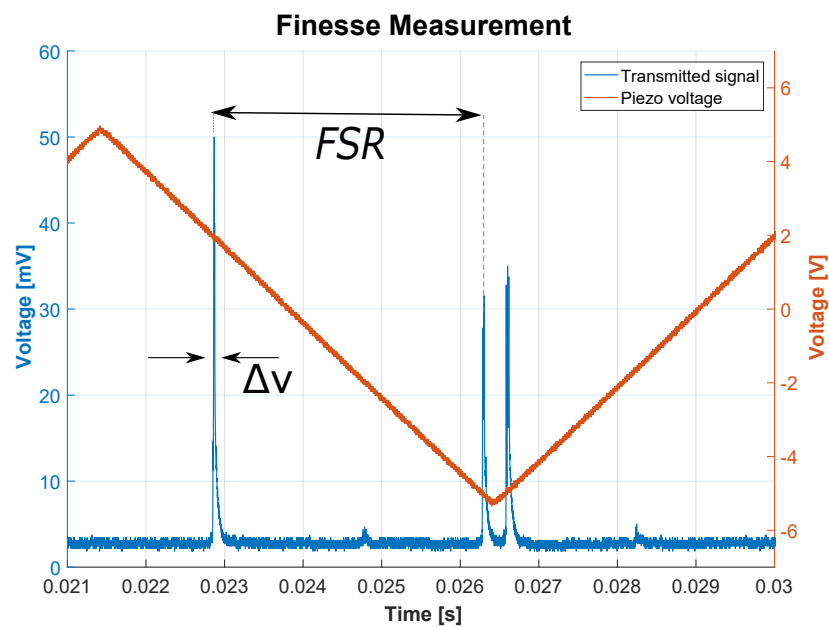


Figure 4.15 Example of a finesse measurement from the oscilloscope: the Free Spectral Range is divided by the peak width.

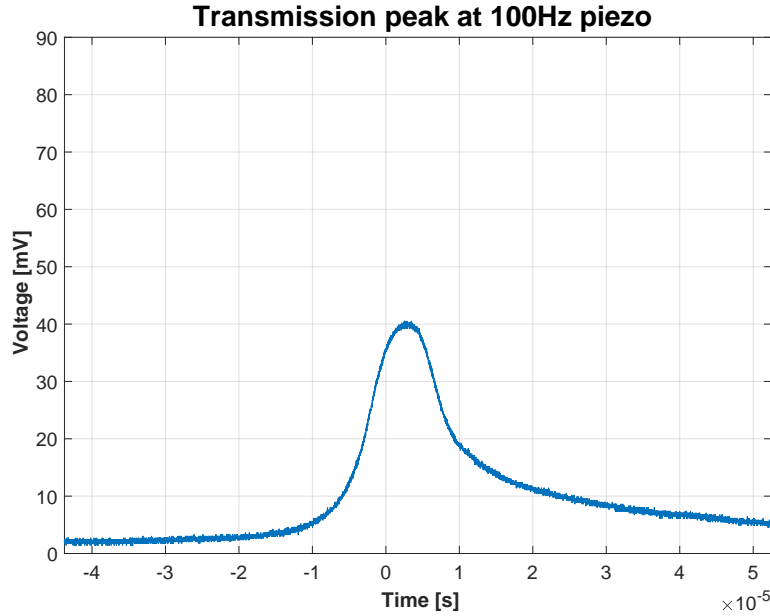


Figure 4.16 Peak shape for a piezo scan frequency of 100 Hz. The asymmetry due to the excessive scan speed is here evident. Indeed, the cavity characteristic time τ_c is comparable with the width of the transmission peak.

(a more precise value is calculated later in this subsection), while the temporal HFHM of a transmitted peak at frequency scan of 100 Hz is about $6 \mu\text{s}$ wide. Another cause of the asymmetry could be the characteristic time of the photodetector, namely $\tau_{ph} = 1.76 \cdot 10^{-7} \text{ s}$, but we have considered it negligible respect to τ_c . It is then important to use a scan frequency sufficiently low. On the other hand, at very low frequencies like 5 Hz, the piezoelectric actuator is subject to disturbances and noises that deform the peak shape and forbid precise measurement. In Figures 4.16, 4.17, 4.18 are presented some examples of peak shape at different frequencies. We have chosen a scan frequency of 10 Hz as the best compromise.

With an incident power of 0.01 W, the transmitted power detected after mirror *B* is equal to 0.37 mW (corresponding to 110 mV voltage peak) and in such condition we measured a Finesse value of $F = 470 \pm 25$. From the Finesse experimental value can be estimated the product of all reflection coefficients of cavity mirrors and the power inside the cavity. Solving

$$\begin{cases} F = \frac{\pi \sqrt[4]{R_{TOT}}}{1 - \sqrt{R_{TOT}}} \\ P_{tranB} = T_B P_{in} \frac{1 - R_1}{|1 - \sqrt{R_{TOT}}|^2} \end{cases} \quad (4.7)$$

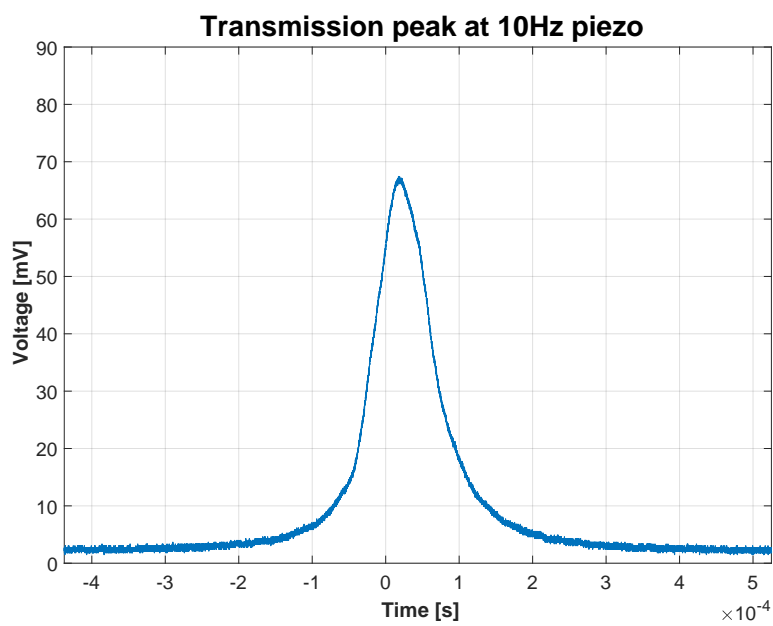


Figure 4.17 Peak shape for a piezo scan frequency of 10 Hz. The shape is very symmetric if compared to the one at higher frequencies and can be exploited in Finesse measurements. The asymmetry is here strongly reduced because the temporal width of the transmission peak is about 10 times longer than in the previous condition, then τ_c is negligible. A scan frequency equal to 10Hz represents our best compromise in Finesse measurement.

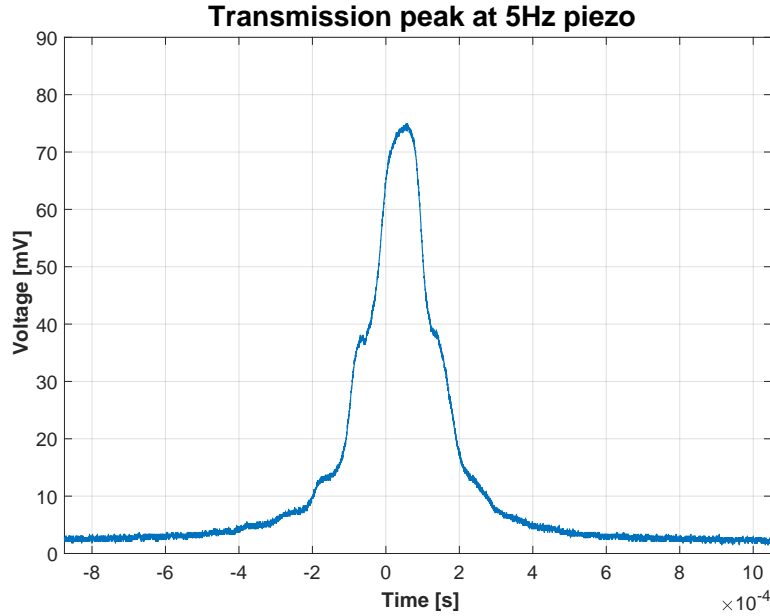


Figure 4.18 Peak shape for a piezo scan frequency of 5 Hz. Although the peak is symmetric and the cavity characteristic time is enough lower than the peak width, disturbances and noise deform the peak shape, avoiding precise Finesse measurements.

we find $R_{TOT} = 0.98676$ and $R_A = 0.99804$. Exploiting R_{TOT} cavity characteristic time τ_C can be calculated as

$$\tau_C = \frac{L}{\gamma_C} = 7.503 \cdot 10^{-7} s \quad (4.8)$$

where $L = 3$ m and $\gamma = -\ln R_{TOT}$. We can also estimate the radiation power inside the cavity, which is given by

$$P_{cav} = P_{in} \frac{(1 - R_A)}{|1 - \sqrt{R_{TOT}}|^2} = 465 \text{ mW} \quad (4.9)$$

4.3.4 Spot and Waist dimension

Know the spot dimension on mirrors and the waist size in the focal point in function of the distance of the curved mirrors is fundamental for the characterization of the bow-tie cavity developed in MariX project. In particular, the spot size is very important at high powers in order to avoid excessive heating of mirrors, while the waist dimension is of great importance especially thinking to the electron-photon scattering. We directly measured the spot dimension out the mirror C exploiting the CCD camera, the ThorCam software and an imaging system that recreates the mirror spot on the camera. From these data both the waist dimension and the spot size on the mirror can be obtained. It is worth to note that the

measured spot dimension is not the one on the mirror, but the spot dimension on its external surface, so a mathematical correction has to be performed. But how to calculate the spot size on mirror C and the waist dimension on focus starting from the experimental data? We made use of the so called *Far Field Technique*[23]. The basic idea is simple: when $z_{Rayleigh} \ll z$ the radius of a Gaussian beam can be asymptotically expanded as

$$w(z) \approx \frac{\lambda}{\pi w_0} z \quad (4.10)$$

where w_0 is the waist dimension that we are looking for and z is the distance from the focus. Since our experimental data are taken outside the mirror, we have to consider the matrix elements of the mirror interfaces (one curved interface and one flat, with a free space propagation in fused silica between them), that corrects the beam propagation equation (Eq.4.11). Counterpropagating the experimental spot dimension until the waist position, we obtain the waist dimension. Then, defining \tilde{z} as the distance of mirror C from the focus position, we have

$$w_{spot-mirror}(z) = \frac{\lambda}{\pi w_0} \tilde{z} \quad (4.11)$$

Successively, we checked our experimental results with theoretical predictions. We can calculate such theoretical functions of waist dimension and spot on mirror C size defining the Round-Trip Matrix of the cavity, choosing as a starting position a point immediately before the mirror C . Recalling that the matrix element corresponding to curved mirrors² free space propagation in paraxial approximation are respectively

$$M_{Curved} = \begin{pmatrix} 1 & 0 \\ -2/R & 1 \end{pmatrix} \quad (4.12)$$

and

$$M_{Space} = \begin{pmatrix} 1 & z \\ 0 & 1 \end{pmatrix} \quad (4.13)$$

we are able to write the Round-Trip Matrix as a function of the curved mirrors distance d , leaving p as a free parameter that determines the considered axis:

$$M_{RT}^{\{p\}} = \begin{pmatrix} 1 & L_2 \\ 0 & 1 \end{pmatrix} \cdot \begin{pmatrix} 1 & 0 \\ -2/R'_B & 1 \end{pmatrix} \cdot \begin{pmatrix} 1 & L_{TOT} - L_2 \\ 0 & 1 \end{pmatrix} \cdot \begin{pmatrix} 1 & 0 \\ -2/R'_C & 1 \end{pmatrix} \quad (4.14)$$

²Plane mirror's matrix are simply the Identity Matrix so it is trivial to consider them in the beam propagation.

where $R'_B = [\cos(\theta_B)]^p$ and $R'_C = [\cos(\theta_C)]^p$, with $p = -1$ for the horizontal plane and $p = +1$ for the vertical plane and while θ_B and θ_C are the incidence angles on mirror B and C respectively. Note that the incidence angle has different values for the vertical and the horizontal axis, while $\theta_B = \frac{\alpha}{2} = 3.85^\circ$ and $\theta_C = \frac{\beta}{2} = 3.14^\circ$. It is then possible to obtain the stability parameters $m_p = \frac{[M_{RT}^{\{p\}}(1,1) + M_{RT}^{\{p\}}(2,2)]}{2}$, labeled m_V and m_H . We can then directly calculate the theoretical beam dimension $w(z)$ for both axes at the point in which the Round-Trip has been started, so on mirror C . It is also possible to calculate the theoretical waist dimension using a similar procedure. Indeed in this case the waist position is unknown, but it can be calculated as a function of R_B , R_C , L_2 and d . Such parameters can be exploited to study the beam radius and find the point at which $1/R_{beam}$ is null, that is z_{focus} . When z_{focus} is known, the same procedure used to find the theoretical beam dimension on spot can be exploited to calculate the waist dimension.

The spot size on mirror C $w_{SpotMirror}$ and the waist dimension w_0 are shown in Figure 4.19a and Figure 4.19b as a function of the distance between the two curved mirrors of the cavity. The theoretical functions are also drawn.

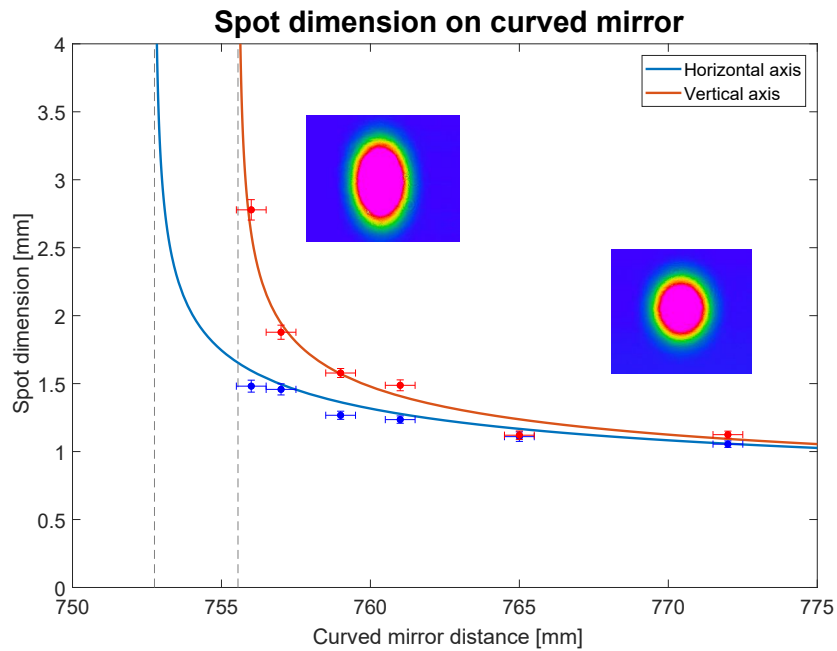
Mode frequency is directly dependent on the stability parameter of the resonant cavity. In fact, recalling 3.17

$$\nu_{npq} = FSR \left(n + \frac{1/2 + p}{2\pi} \arccos m_H + \frac{1/2 + q}{2\pi} \arccos m_V \right)$$

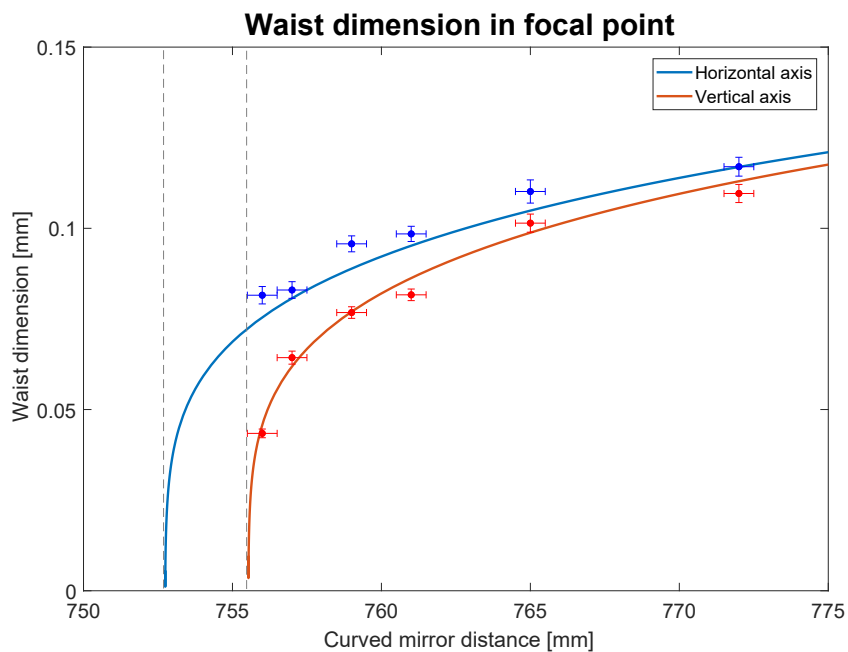
it is clear that m_V and m_H play a fundamental role. We directly observed this fact checking the distance between the fundamental mode $TEM_{0,0}$ and the nearest second order mode, thus $TEM_{0,2}$, for two different curved mirror distances so observing the difference

$$\Delta\nu [(n, 0, 0) - (n-1, 0, 2)] = FSR \left(\frac{2}{2\pi} \arccos m_V \right) \quad (4.15)$$

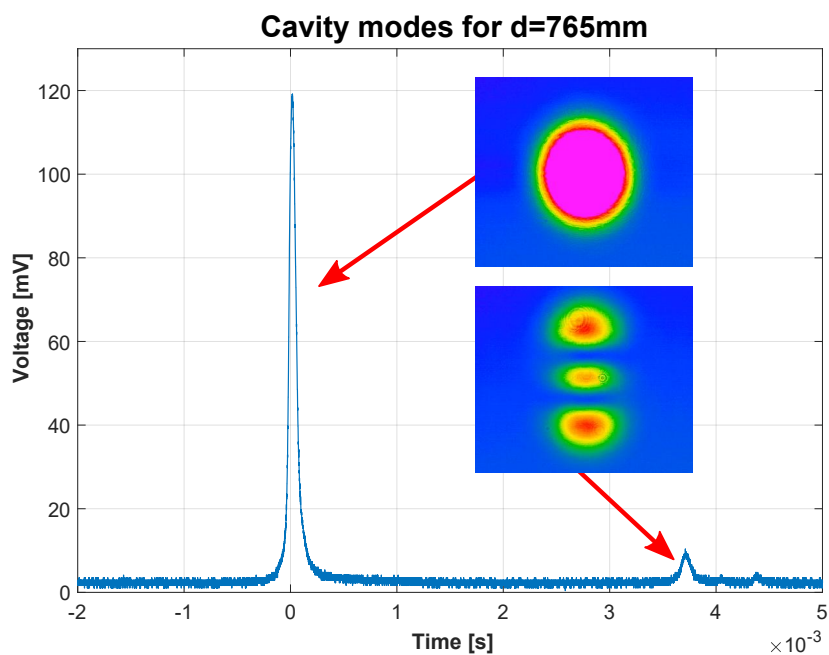
In particular, we have chosen $d_1 = 758$ mm and $d_2 = 765$ mm and in both the cases we sent to the actuator a 5 Hz triangular wave. The experimentally observed mode shift is exposed in Figures 4.20a and 4.20b. If curved mirror distance reduces, stability parameters (horizontal and vertical) values reduce approaching to -1. Since \arccos is a decreasing function equal to π when its argument is equal to -1, near the confocal configuration the distance in frequency between the fundamental mode of longitudinal index n and the second order mode posed in s with longitudinal index $n-1$ is lower than for higher values of m_V and m_H .



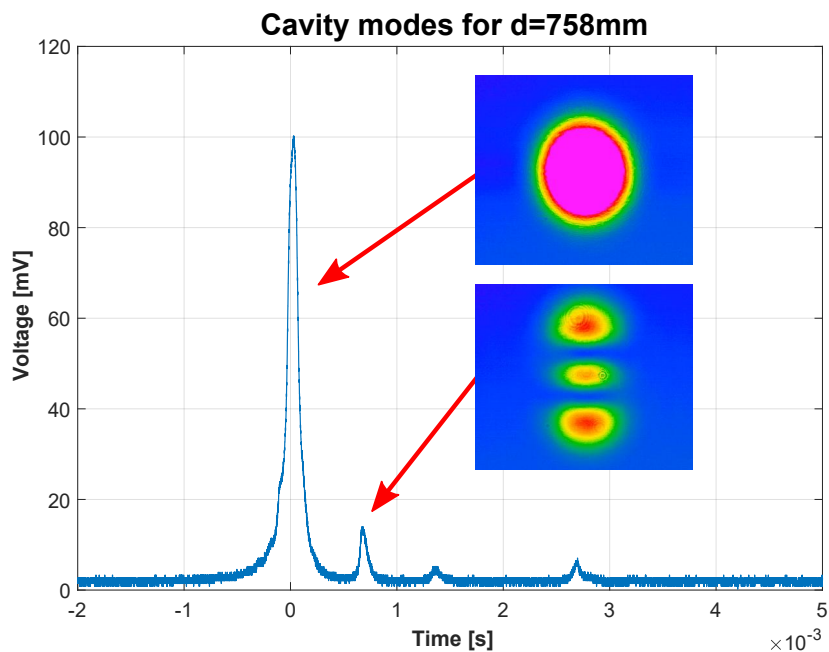
(a) Spot dimension on mirror C as a function of the distance between mirrors B and C . The continuous lines represent the theoretical behavior of the horizontal and vertical axes, while the two spot images are examples of the spot shape for the near-confocal configuration (*left*) and for a more stable situation (*right*). We can observe that the spot is almost circular when $d = 772$ mm, while near the confocal configuration the difference between vertical radius and horizontal radius is about 1 mm.



(b) Waist dimension in the cavity focal point. The continuous lines represent the theoretical behavior of the horizontal and vertical axes. We can note that for configurations near the confocal, then for $d \approx 755$ mm the waist is similar to the MariX electron bunch size [1].



(a) Cavity modes for a curved mirror distance of 765 mm. On the left there is the n^{th} $TEM_{0,0}$, while on the right there is $(n-1)^{\text{th}}$ $TEM_{0,2}$.



(b) Cavity modes for a curved mirror distance of 758 mm. Note that in this case the modes separation is smaller than in the previous case.

Chapter 5

Feedback system and noise suppression

The feedback system deserves a separate chapter in this work because of its fundamental importance and in order to better explain the experimental results achieved on the coupled cavity-laser system. In the first part of the following chapter, a detailed characterization of the feedback system components will be exposed. After that, we will discuss stability performances and noise suppression results.

5.1 Feedback characterization

The feedback system components have been characterized and studied in order to comprehend their behavior. We will start discussing about the Discriminator, and then we will write about the Servo and Actuator. The Source and the Reference of the feedback will not be described because they were already explained in Chapter 4 as the FP cavity and the Menlo laser oscillator respectively.

5.1.1 Discriminator

The Discriminator is the feedback component that generates the Pound-Drever-Hall error signal which is sent to the Servo. The implementation scheme is shown in Figure 5.1. Its first part consists of an Electro-Optical phase modulator fed with a high voltage RF (Radio Frequency) sinusoidal signal at a frequency of $\Omega = 3.5$ MHz. EOM generates two sidebands in the laser beam which are sent into the cavity. The same RF signal is also sent to a de-amplifier and phase shifter circuit and then to a mixer (Mini-Circuits Mixer ZFM-3+) where it is used to demodulate the signal coming from the Discriminator detector. Indeed,

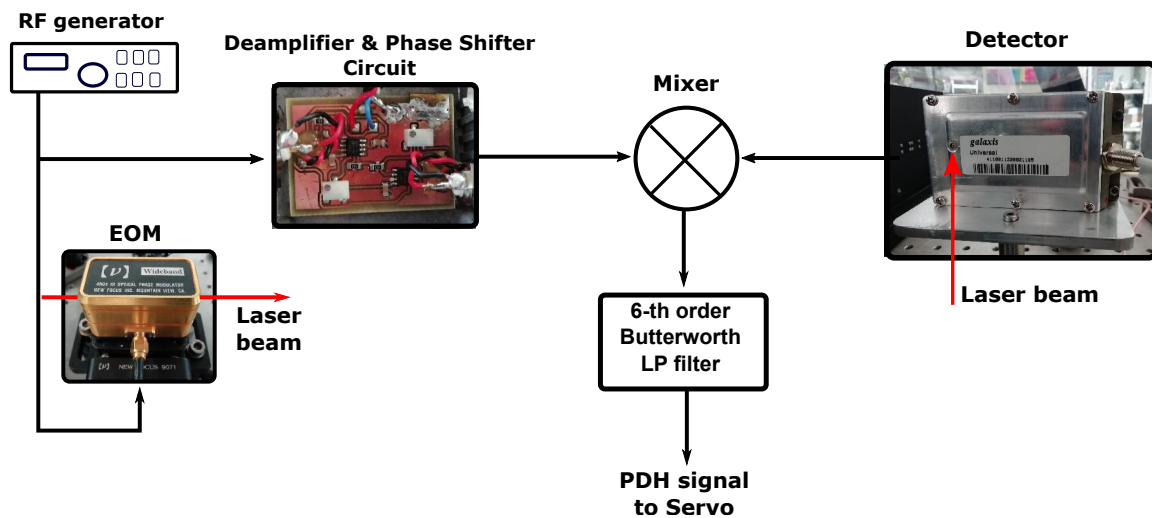


Figure 5.1 Discriminator scheme is here represented. Images of the main components such as the EOM, the detector and the deamplifier are also provided.

since not all the laser beam enters the cavity, an appositely built fast photodetector¹ reads the reflected signal summed to the radiation transmitted from cavity mirror A. Such signal is sent to the mixer where is demodulated using the de-amplified RF signal. Furthermore, the phase shifter can introduce a relative phase correction between the signal from the detector and the RF sine wave. The signal outgoing the mixer contains the frequency components of the the carrier signal as well their sums and difference, for this reason a low-pass filter (we used a 6-th order Butterworth filter with cut frequency of 100kHz) is needed after the mixer in order to suppress high frequency contributions. The signal is then ready to be sent to the Servo. EOM and mixer need to be fed by the same RF in order to modulate and de-modulate the signal, but it is worth to note that the voltage amplitude needed by the two components is completely different. In fact, EOM requires a quite high voltage, while mixer input must be only 7dBm. In our case, the wave generator sends into the circuit a sine wave with *peak-to-peak* amplitude of 12.2V. De-amplificator circuit is necessary to reduce the amplitude and satisfy the mixer needs. Moreover, we have also to optimize the reflected beam incidence on the detector: a good incidence is important in order to have a good signal-to-noise ratio and an bigger PDH signal. Figure 5.2 is an image taken from the oscilloscope of PDH signal outgoing the discriminator stage while a triangular wave is sent to the actuator (as we have done for Finesse measurements).

¹The fast photodetector has been designed from the Electronic research group of Physics department of Università degli studi di Milano.

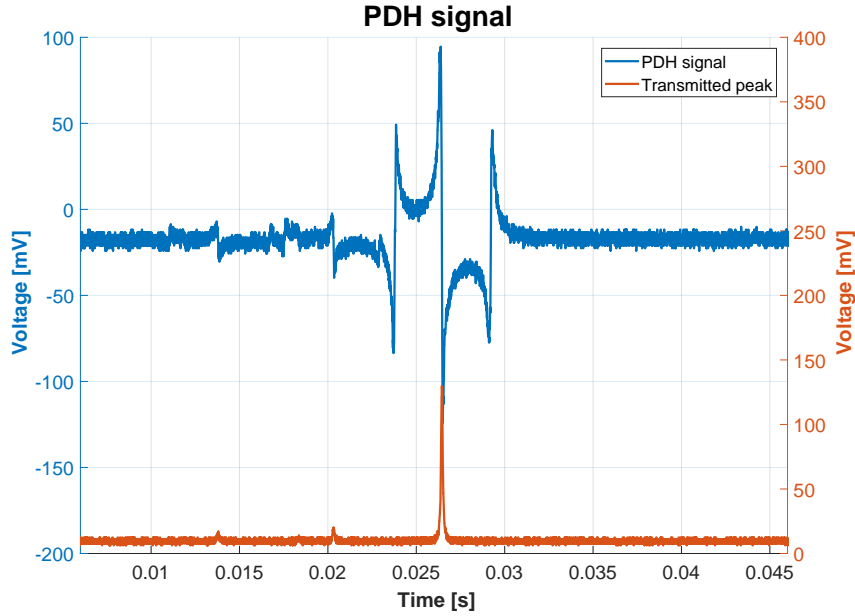


Figure 5.2 PDH signal obtained during an actuator scan. The two 3.5 MHz sidebands of the error signal are well visible. Below the error signal there is the corresponding transmission peak.

From frequency to voltage: $D(f)$

The discriminator transfer function converts the frequency detuning between the laser and the Fabry-Perot cavity to a voltage signal. In particular, the PDH signal value is directly related to such detuning. PDH error signal linear region is shown in Figure 5.3: here the asymmetry of the signal for negative or positive detuning is well visible. More precisely, we have $V_D(f) = [v_r(f) - v_s(f)] D(f)$. In order to calculate $D(f)$, we must consider both the frequency-voltage conversion coefficient (that we name $k_{\text{discriminator}}$) and the Butterworth filter transfer function. Firstly, for a fixed scan frequency, the temporal distance $\Delta\tau_S$ between the carrier and one of the two sidebands is measured. This time corresponds to Ω , so to a frequency of 3.5 MHz. Dividing $\Delta\tau_S$ by Ω we can obtain a coefficient C_1 . The second step is determine a second coefficient measuring the time $\Delta\tau_V$ corresponding to a given voltage difference on the PDH signal ΔV ; their ratio is named $C_2 = \Delta V / \Delta\tau_V$. Multiplying C_1 and C_2 each other and renormalizing we obtain $k_{\text{discriminator}} = 5.05 \cdot 10^{-6} \text{ V/Hz} = 5.05 \text{ V/MHz}$, thus a variation in frequency of 1 kHz corresponds to a variation of 5.05mV of the PDH signal. the function $D(f)$ is then the transfer function of the low-pass filter at the output of the Discriminator, multiplied for $k_{\text{discriminator}}$ ($D(f)$ is plotted in Figure 5.4). It is important to note that the phase of $D(f)$ is completely determined by the low-pass filter and due to the

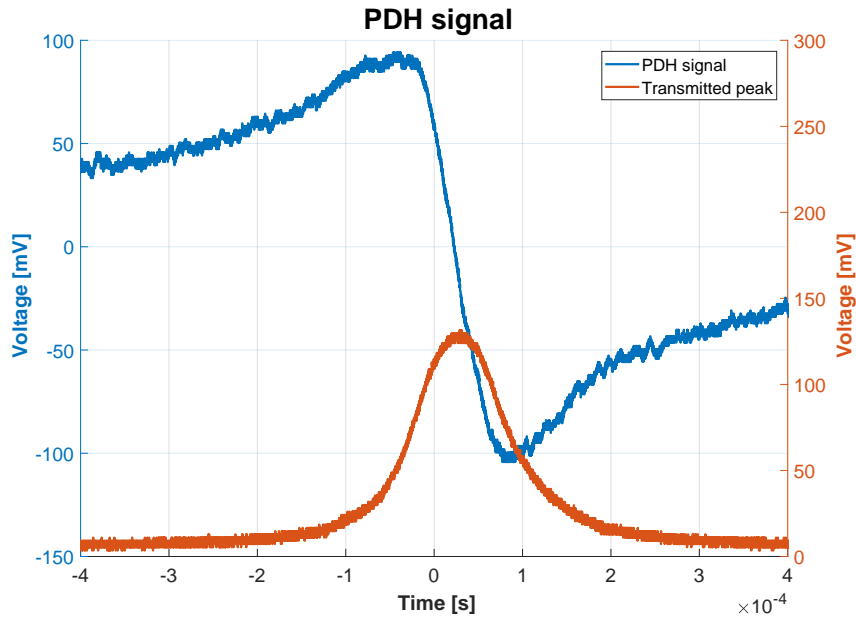


Figure 5.3 PDH signal zoom on the linear region. Below the error signal there is the corresponding transmission peak.

high cut frequency, it is substantially null in the spectral region of interest for our system stabilization (up to few tens of kHz).

5.1.2 Servo

The output signal of the Discriminator is sent to the Servo, that manipulates it and gives to the Actuator a signal adequate to reduce the frequency detuning between Source and Reference. In our case it consists of a PID circuit (Proportional-Integrative-Derivative²) made in our laboratory and shown in Figure 5.5. The PID electric schematics is represented in Figure 5.6. The PDH error signal firstly enters into the *offset stage*. Here the signal offset can be changed by the add of a DC voltage, in order to center the PDH signal on the cavity transmission peak. Without this stage a wrong error signal could lead the cavity not to stabilize on the resonance frequency but only near it. the offset stage introduces an almost unitary gain $k_{offset} = 0.988402$. We measured this value comparing sinusoidal input signals read at the *Offset Monitor* output and averaging the experimental data obtained at different frequencies (10 Hz, 100 Hz, 1 kHz and 10 kHz). Thus the offset transfer function is a real

²Despite the name, the derivative part is not implemented in our apparatus.

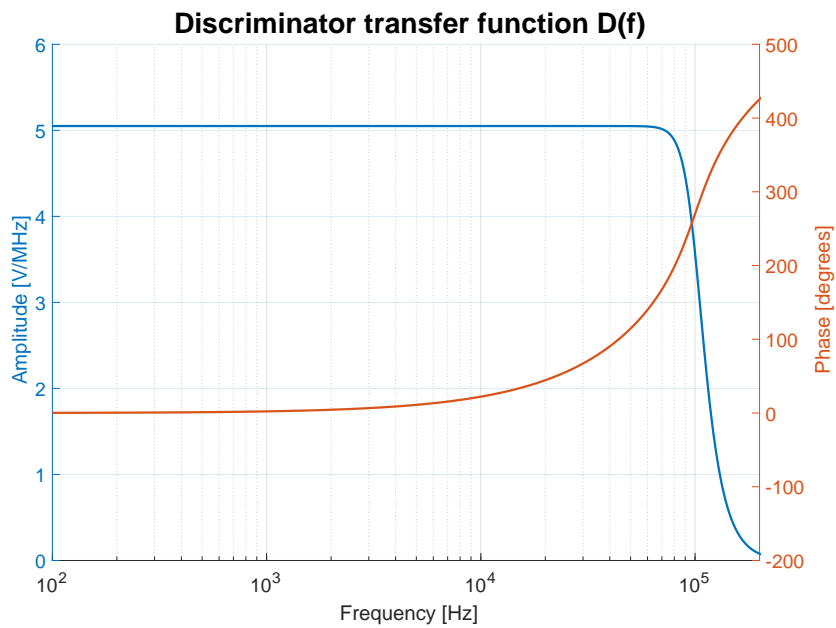
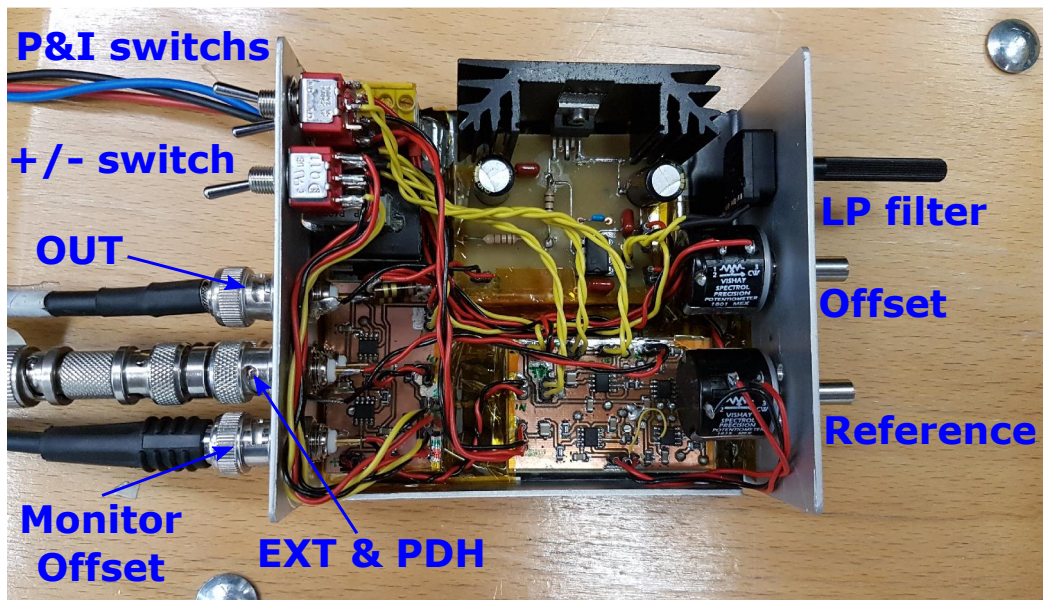
Figure 5.4 Discriminator transfer function $D(f)$.

Figure 5.5 PID picture. Input/output channels and manual controls names are here written in blue

constant simply given by:

$$G_{offset}(f) = k_{offset} = 0.988402 \quad (5.1)$$

The signal leaving the offsetstage goes to the *proportional* and the *integrator* stages. The proportional consists of a non-inverting operational amplifier with a voltage divider and an high-pass filter on its input. The proportional tranfer function is:

$$G_{proportional}(f) = G_{tension-divider}(f) G_{HPF}(f) G_{non-inv}(f) \quad (5.2)$$

$$= \left(\frac{R_{22}}{R_{21}} \right) \frac{2\pi f R_5 C_1}{1 + i2\pi f R_5 C_1} \left(1 + \frac{R_7}{R_6} \right) \frac{1}{1 + i2\pi f T} \quad (5.3)$$

where the operational amplifier gain-bandwidth product GBW has been considered and $T = [2\pi f_C]^{-1}$ is the time associated to the OP-Amp cut frequency $f_C = GBW \left[1 + \frac{R_7}{R_6} \right]^{-1}$. Note that R_6 is variable and it can be used to change proportional gain. The proportional can be switched on and off. The signal is also sent to the *integrator* stage, which is an inverting integrator circuit with transfer function given by:

$$G_{integrator}(f) = -\frac{1}{i2\pi f R_8 C_2} \quad (5.4)$$

As in the case of R_6 , R_8 is variable and it allows us to modify the integrator gain function³. The *integrator* can be switched on and off as the *proportional*, but without it we are not able to stabilize the cavity-laser system. Then, during the stabilization process, the integrator is switched on and maintained active. The PID is also composed by a *reference*, which generates an adjustable DC voltage directly sent to the piezoelectric actuator and used to search the resonance lenght. Then we have a *summer* circuit which takes as input the signals from the previous stages and summing them together. The tranfer function of the summer can be considered unity for the inverting input. After the summer there is a *unitary gain amplifier*, that is fundamental to drive the Actuator, because the previous stages cannot provide the needed electric current, which exceeds the used Op Amps parameters (Analog Devices OP07). This last stage is composed of a simple buffer with infinite input impedance that allows to uncouple the previous part from the Actuator, avoiding signal degradation, and of an unity gain circuit with high output current operational amplifier (Texas Instruments -LM675). It is fundamental to notice that if on the one hand the mechanical features of the piezoelectric belong to the Actuator response, on the other hand its electrical properties have to be considered as a part of the Servo. Indeed, because of its capacity $C_{piezo} = 1.431 \mu F$

³In next Sections we will refer to R_6 simply as R_{prop} and to R_8 simply as R_{int}

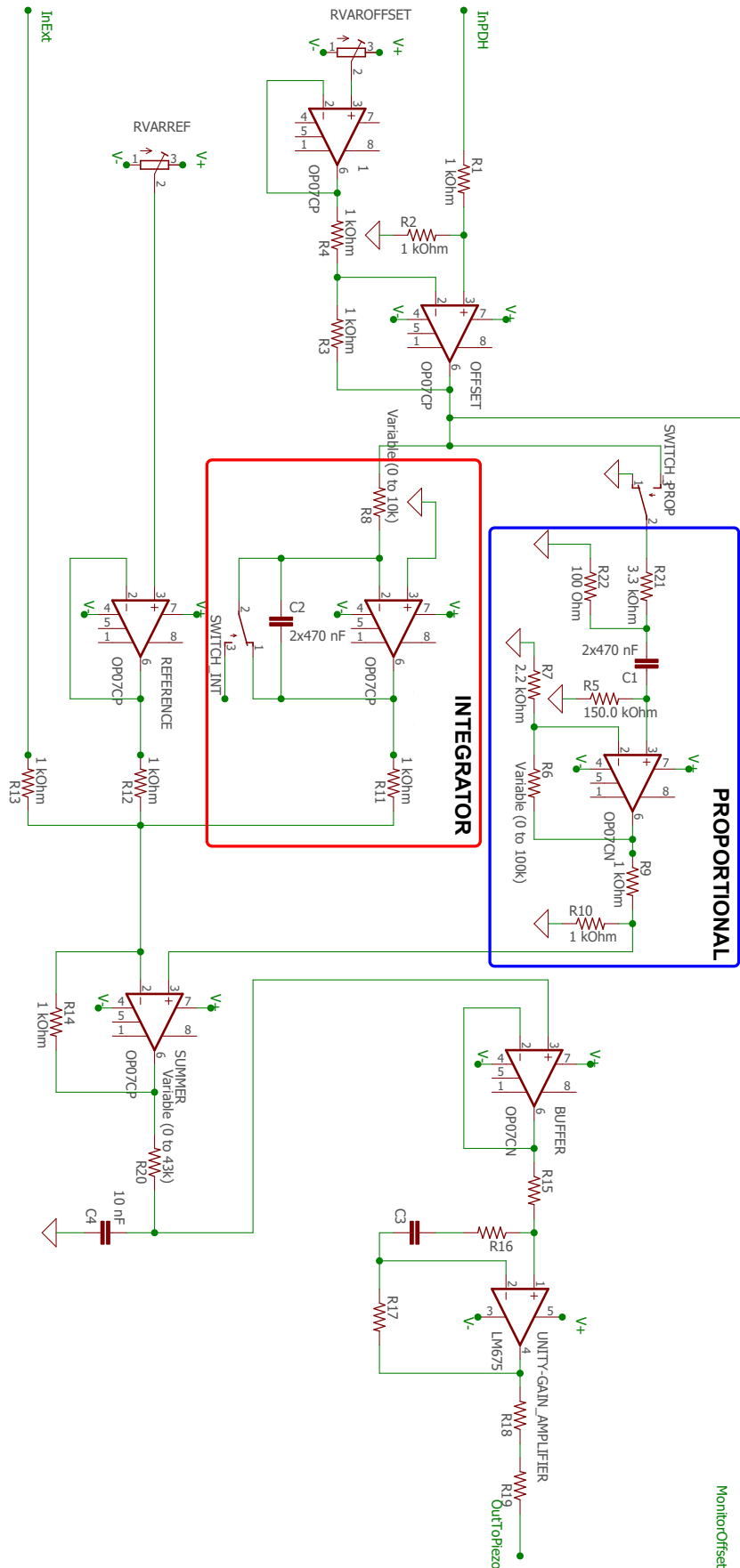


Figure 5.6 Servo circuit schematics. Integrator and proportional components are highlighted in red and blue.

and the presence of two resistances at the end of the unitary gain circuit $R_{18} = R_{19} = 1\Omega$, the piezoelectric crystal behaves as a low-pass filter which transfer function that must be considered in Servo transfer function calculation.

$$G_{piezo}(f) = -\frac{1}{1 + i2\pi f(R_{18} + R_{19})C_{piezo}} \quad (5.5)$$

In order to avoid the satisfaction of Barkhausen criterion for the global feedback loop, a single-pole low-pass filter has been inserted in the PID circuit. Its adjustable resistance R_{fil} make us capable of avoiding self-oscillations of the system choosing the right cut frequency. The low-pass filter complex transfer function is given by:

$$G_{fil}(f) = -\frac{1}{1 + i2\pi f R_{fil} C_{fil}} \quad (5.6)$$

From voltage to voltage: $H(f)$

The servo transfer function is obtained multiplying all the transfer functions we treated above. It is worth noting that the Servo response to a signal is completely different when the proportional is switched on or off. We can then distinguish two different Servo transfer functions for the two cases. When the proportional is switched off we have

$$H_{propOFF}(f) = G_{offset}(f) G_{int}(f) G_{piezo}(f) G_{fil}(f) \quad (5.7)$$

while $H(f)$ becomes

$$H_{propON}(f) = G_{offset}(f) [G_{int}(f) + G_{prop}(f)] G_{piezo}(f) G_{fil}(f) \quad (5.8)$$

when the proportional is switched on. In Figure 5.7 are shown two examples of transfer function of the Servo, one with proportional switched on and one without it. We can note that at low frequencies the behavior is the same for the two cases because the integrator is dominant. In this region we can also observe that the phase is near 90 degrees. When the proportional is switched off the phase raises due to the low-pass filter and the amplitude simply decreases. If the proportional is present, the phase goes to low values before raise because of the proportional contribution that becomes dominant from frequencies about $10^3 Hz$ until $10^5 Hz$, so where the filter contribution is no more negligible⁴. When the filter contribution become important around $10^5 Hz$ the gain amplitude decrease to zero also if the proportional is switched on.

⁴in the case represented in Figure 5.7 the low-pass filter cut frequency is $f_{fil} = 1.592 \cdot 10^7 Hz$

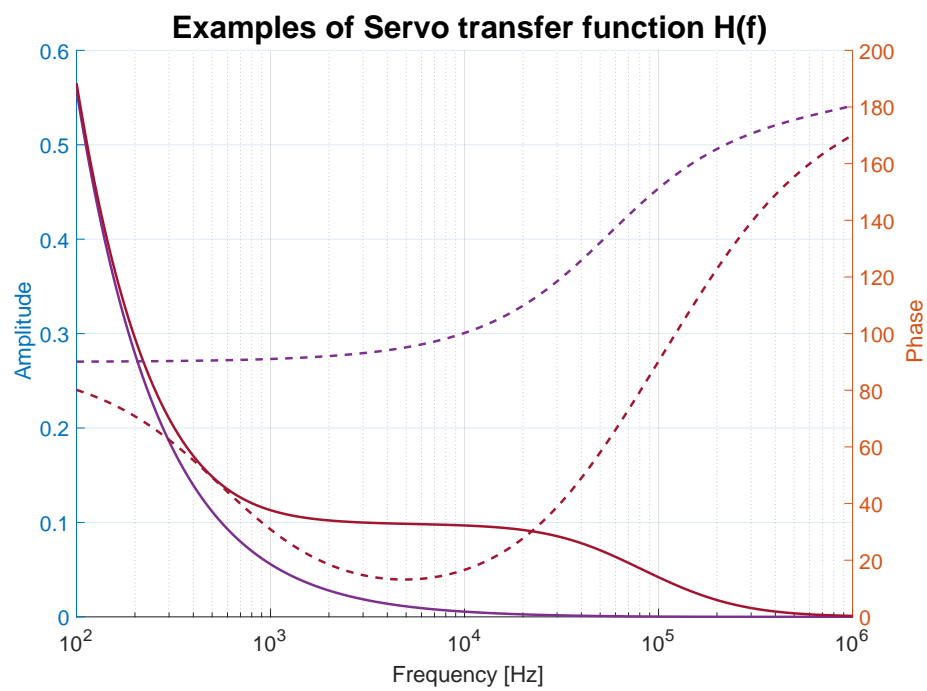


Figure 5.7 Two examples of $H(f)$ (continuous lines are amplitudes, while dashed lines are phases). $H_{propOFF}$ is plotted in purple and it is the transfer function when $R_{int} = 3k\Omega$ and $R_{fil} = 1\Omega$. H_{propON} is drawn in red and in this case $R_{prop} = 1k\Omega$.

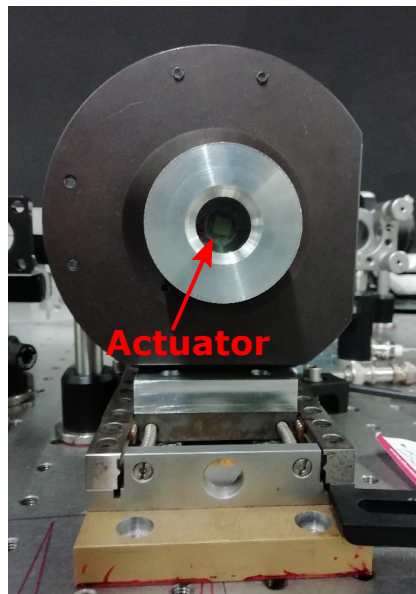


Figure 5.8 Picture of mirror D mount, micrometric slide and piezoelectric crystal. The red arrow indicates the Actuator, visible in the center of the mirror.

5.1.3 Actuator

The Actuator consist of the piezoelectric fixed on the mirror D mount. As we have seen in the theoretical chapter, when a voltage is applied to the piezo, it changes its lenght shifting the mirror D position following the signal elaborated by the Servo or probe triangular signals. In Figure 5.8 is shown mirror D mount and the Actuator behind the mirror, which is transparent in the visible region. subsectionFrom voltage to frequency: $A(f)$ As for $D(F)$, the Actuator transfer function calculation is divided in two steps: the first one is to measure the piezo spectral response, the second one is to calculate the voltage-to-frequency conversion coefficient k_{act} . $A(f)$ is obtained multiplying the spectral response by k_{act} .

Piezo spectral response has been measured by using a Michelson Interferometer and exploiting a narrow-linewidth infrared Nd:YAG laser as we have schematized in Figure 5.9. In particular we used a Mephisto 1500NE, which is characterized by a spectral linewidth of few kHz and consequently by a very large coherence time. The Mephisto light goes on a beam splitter that divides the light into two components, where the first goes ahead and it is reflected by a metallic mirror, while the second component is sent to the mirror C . The beam then recomposes, generating the interference, and incides on the photodetector. Firstly, the probe traingular wave has been sent to the Actuator, making interference fringes visible on the oscilloscope, as shown in Figure 5.10. Then, choosing the middle of a fringe as working point, a few millivolts sine wave is sent to the piezo instead of the triangular signal. In this situation the photodetector can releivate the same sine wavefunction, but with amplitude and

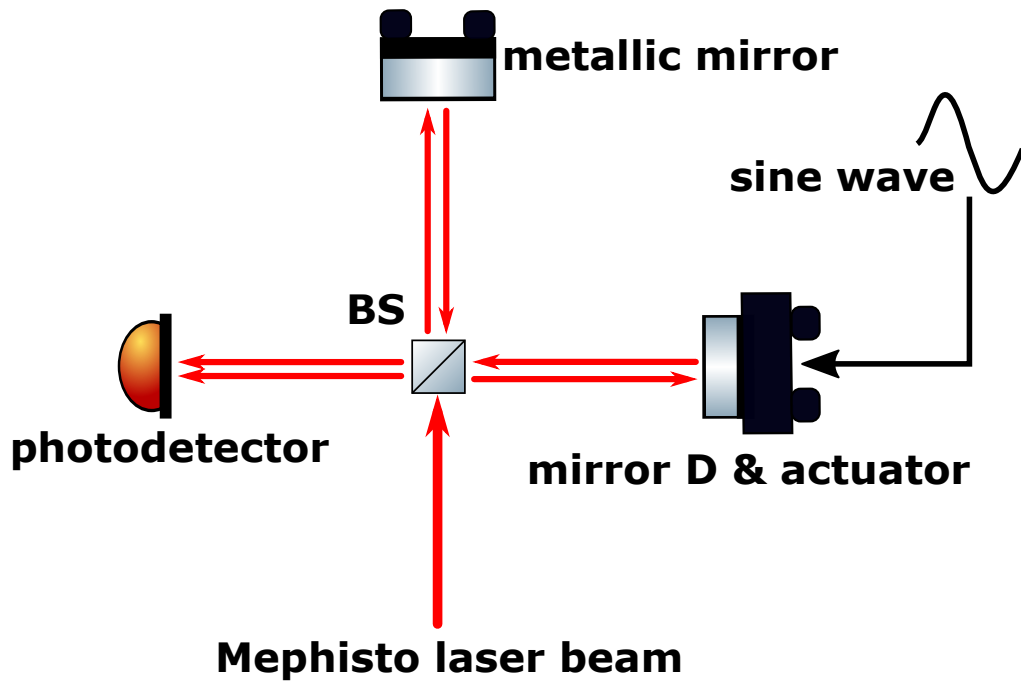


Figure 5.9 The Michelson Interferometer scheme.

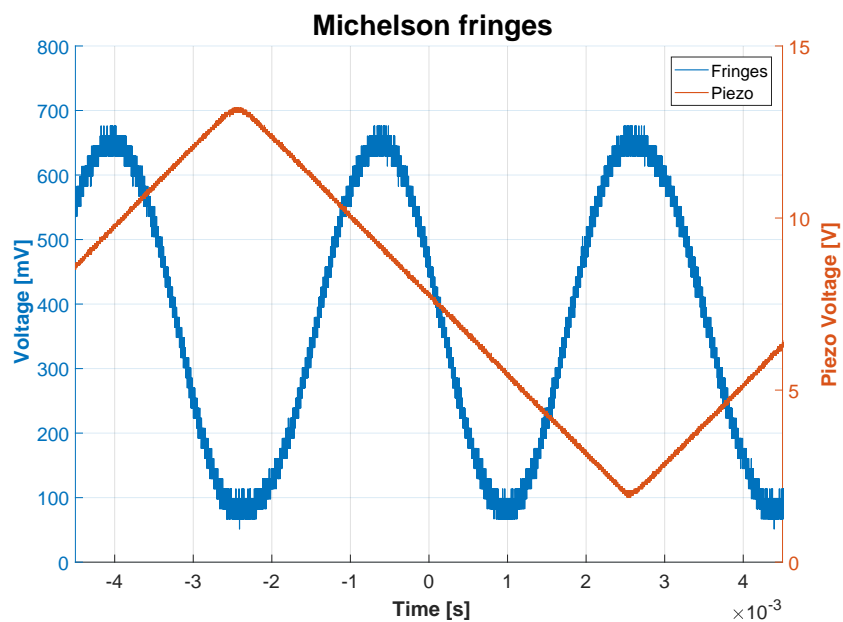


Figure 5.10 Michelson interference fringes visible during a piezo triangular scan. In this case the working point is around 0.4 V

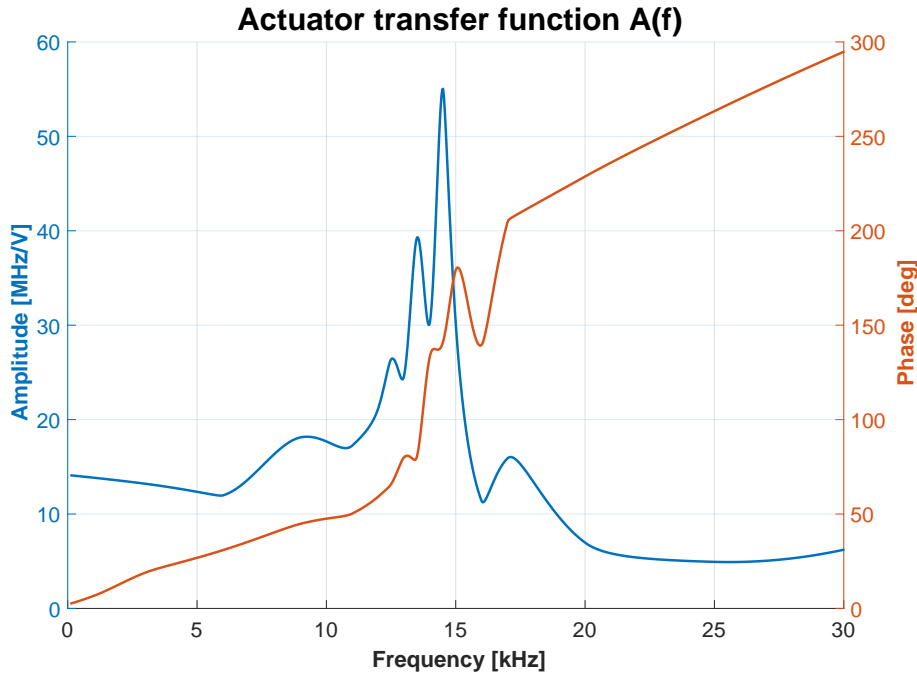


Figure 5.11 The Actuator transfer function $A(f)$.

phase depending on the piezoelectric crystal spectral response. The different amplitudes have been re-normalized choosing as reference the lowest setted frequency value. The so collected data have been successively interpolate to generate a continuous function $P(f)$.

The second step is the measure of k_{act} coefficient. To determine how many volts correspond to a certain frequency interval, we can do a frequency scansion sending to the actuator a traingular wave as during the alignment process. In this case, we have to choosen a Free Spectral Range (=100 MHz) as frequency reference. The voltage difference correspondent to a FSR is 7.09 V. Since $k_{act} = \frac{\Delta V}{\Delta f}$, we have $k_{act} = 14.1 \frac{MHz}{V}$. The last passage consists of multiply the response curve by the conversion coefficient, obtaining the Actuator complex transfer function:

$$A(f) = k_{act} \cdot P(f). \quad (5.9)$$

The result is exposed in Figure 5.11. We can immidiately note that the piezoelectric has a resonance peak at 14 kHz, associated to a fast increment of the phase, and many humps and smal peaks near the most important one. The presence of more than one peak suggests us that the Actuator could be composed of many harmonic oscillator linked together. The Actuator play a role of great importance on the feedback control bandwidth, since if the phase slope is

high and the the global gain decreases near the unit, the Barkhausen criterion can be satisfied leading to problems in stabilization.

5.2 Stabilization procedure

The feedback global gain function is defined as the product of all the three transfer functions recaved in the previous Sections:

$$G(f) = D(f) H(f) A(f) \quad (5.10)$$

As already exposed in Section 3.2, the noise PSD suppression is not given by only $G(f)$, but by a factor $\frac{1}{|1+G(f)|^2}$, where the phase of $G(f)$ can play a fundamental role when $G(f) \approx 1$. An example of the global gain function $G(f)$ is displayed in Figure 5.12. We can observe a strongly decreasing behavior at low frequencies, which is due to the *integrator* contribute. When the proportional gain becomes important compared to the integrator, $G(f)$ becomes more flat. The low-pass filter and Actuator transfer functions contributions are evident where there are peaks and smooth humps on the function. It is particularly noticeable the Actuator resonance frequency peak around 14 kHz. The Discriminator transfer function acts substantially as a multiplicative constant in the studied frequency region, because of the high cut frequency of the 6-th order Butterworth filter ($f_c = 100\text{kHz}$)⁵. Our feedback system allows us to lock the cavity to the external laser reference and an accurate choice of the PID components gain can lead to noise suppression which is fundamental in order to maintain the system stabilized. We stabilized the cavity for a curved mirrors distance of 763 mm. The main steps of the system stabilization procedure can be resumed as:

- Set to zero the PID offset and find the resonance condition exploiting the PID reference;
- Switch the integrator on. In this initial phase the integrator gain must be low in order to permit fine reulations on th offset ($R_{int} \approx 3/4k\Omega$);
- Make the integrator gain increase (until to $R_{int} \approx 0.65k\Omega$). At this point self-oscillation can occur, but can be reduced reducing the low-pass filter cut frequency.
- Switch the proportional on. A low resistance value ($R_{prop} \approx 40\Omega$) is enough to eliminate most of self-oscillation noise and external noise in the kHz range⁶.

⁵In theoretical simulations the value k_{discr} has been approximated to 3, in order to better fit the experimental evidences.

⁶Higher values of proportional gain can be choosen, but this lead to stronger self-oscillations that require an additional contribution of the low-pass filter, that can excessively reduce the control bandwidth

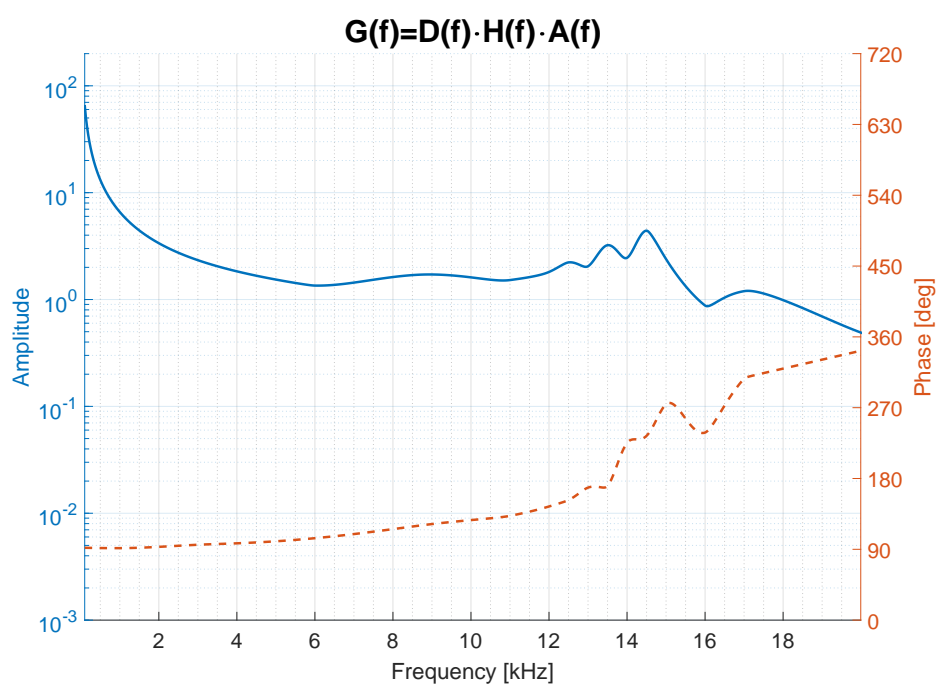


Figure 5.12 Example of $G(f)$ where $R_{int} = 1k\Omega$, $R_{prop} = 10\Omega$, $R_{fil} = 500\Omega$. The amplitude is drawn in blue, while the phase is the orange dashed line.

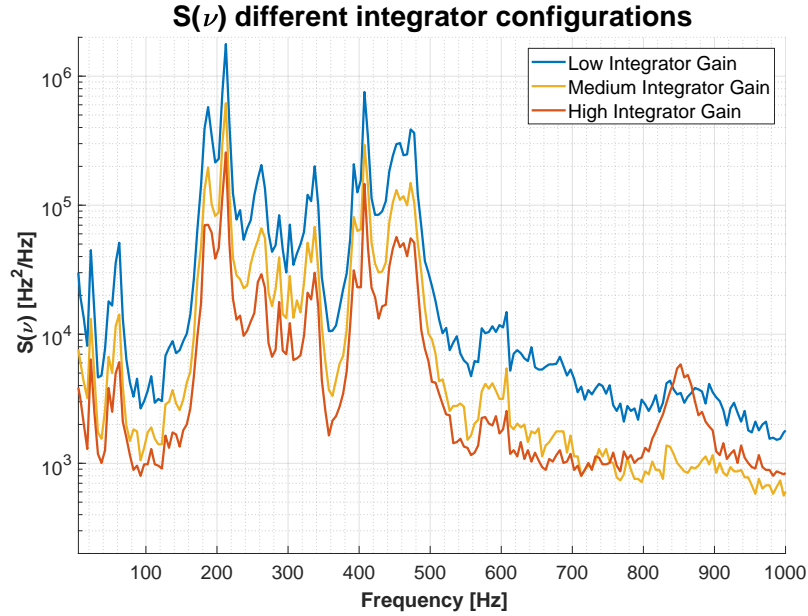


Figure 5.13 Power Spectral density acquired from the Offset Monitor. Low-Frequency noise is strongly reduced by the integrator.

Measurements of the noise suppression has been performed calculating the Power Spectral Density $S(f)$ of the PDH error signal, measured from the Offset Monitor. The PSD has been calculated from the oscilloscope data following the method exposed in Subsection 4.2.2 and using the inverse of $k_{discriminator}$ as voltage-to-frequency coefficient.

Before exposing the stabilization experimental results, it is important to focus on the role of the different PID components in the stabilization.

Integrator's role

Integrator circuit allow us to suppress noise at low frequencies until some hundreds of Hz . In order to demonstrate this fact, we studied the noise peaks height at low frequencies of $S(f)$, locking the cavity to the laser using only the integrator, without the proportional. The peaks amplitude decreases for decreasing integrator resistance, hence for integrator gain growth. In Figure 5.13 are shown the spectra we obtained for different integrator gains (in logarithmic scale). Note that noise level is lower in high and medium gain for the most of frequencies considered. In particular, we started in a low-gain condition where $R_{int} = 4k\Omega$ and then we increased integrator gain choosing $R_{int} = 2.5k\Omega$ and $R_{int} = 1k\Omega$. We also quantified the noise reduction calculating the total noise σ . For low-gain integrator we obtained $\sigma_{low} = 8065 Hz$, for medium-gain integrator we have $\sigma_{medium} = 4926 Hz$, while for

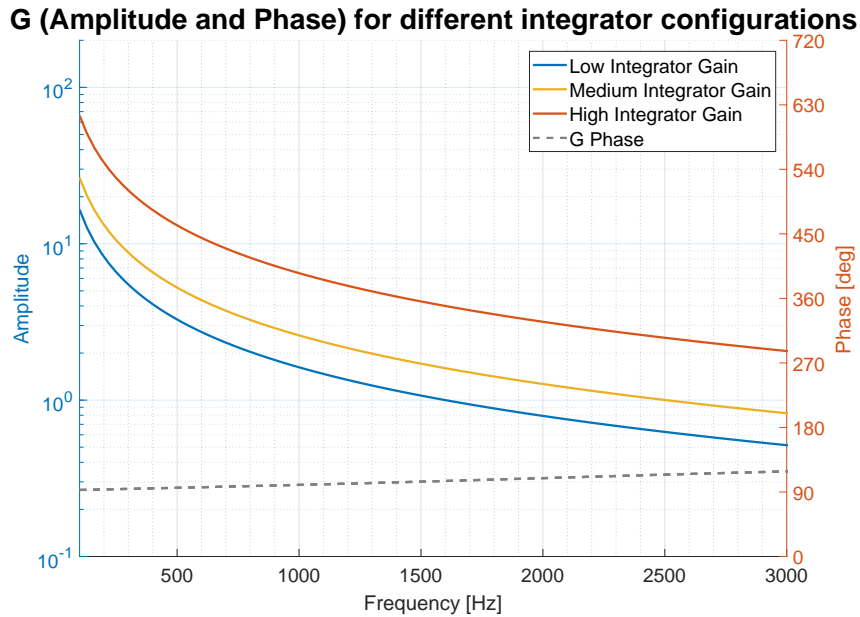


Figure 5.14 Theoretical global gain function. Both amplitude and phase are drawn in the figure. Higher gain values corresponds to higher suppression factors as demonstrated in Equation 3.9

high integrator gain $\sigma_{high} = 3419$ Hz. The experimental result can be explained looking at the theoretical $G(f)$ calculated using the transfer functions above exposed and plotted in Figure 5.14.

Proportional's role

Since the integrator gain function is a decreasing function, at a certain frequency it becomes too little to adequately compensate the noise. For frequencies around a kHz the proportional circuit gains importance and dominates over the integrator. We have proved this fact experimentally, measuring the reduction in height of artificial noise peaks. Such artificial peaks have been generated using a vibrating piezoelectric crystal fixed on the optical table. We observed a reduction of the noise intensity at a frequency of 800 Hz, but we did not observe reductions at 300 Hz, where the proportional has a secondary role compared to the integrator. Experimental spectra can be seen in Figure 5.15 (in linear scale). In the 300 Hz case, we maintained the integrator resistance $R_{int} = 1.15k\Omega$, while we set the proportional resistance value to $R_{propLOW} = 500\Omega$ and $R_{propHIGH} = 7k\Omega$. In the case of 800 Hz artificial noise peak, we set $R_{int} = 2k\Omega$ and we variate the proportional resistance from $R_{propLOW} = 10\Omega$ to $R_{propHIGH} = 11.25k\Omega$.

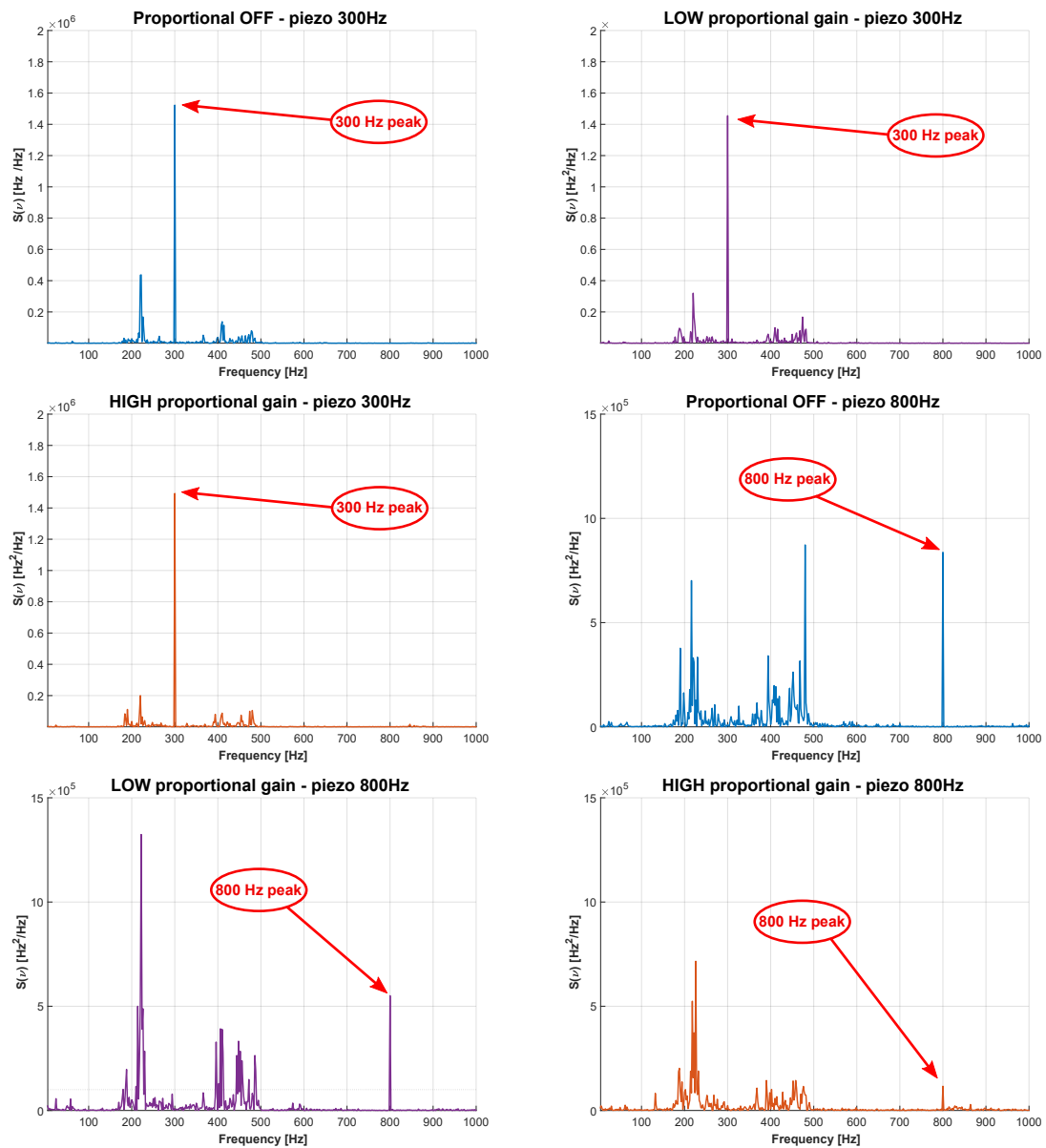


Figure 5.15 Power spectral densities measured for different *proportional* gain and piezo oscillation frequency.

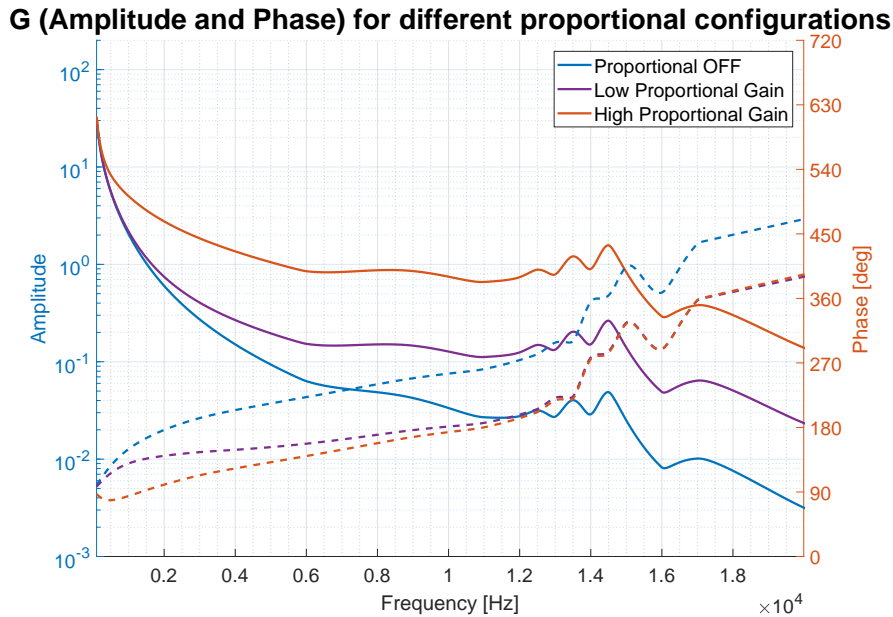


Figure 5.16 Theoretical global gain function calculated for different proportional configurations. Note that phases changes as well amplitudes changes.

We also calculated the suppression factor $\frac{1}{|1+G(f)|^2}$ for whole cases and the ratios *proportional off to high proportional* and *low proportional to high proportional* with the aim of compare such calculated values with the lowering of 800 Hz artificial peaks. The results

$$\frac{|1 + G_{propOFF}|^2}{|1 + G_{propHIGH}|^2} = 7.2 \qquad \frac{S_{peakOFF}}{S_{peakHIGH}} = 6.9$$

$$\frac{|1 + G_{propLOW}|^2}{|1 + G_{propHIGH}|^2} = 4.7 \qquad \frac{S_{peakLOW}}{S_{peakHIGH}} = 5.3$$

proof a good agreement between the theoretical model and the experimental data for what concerns the proportional circuit behavior in the feedback system.

Experimental results

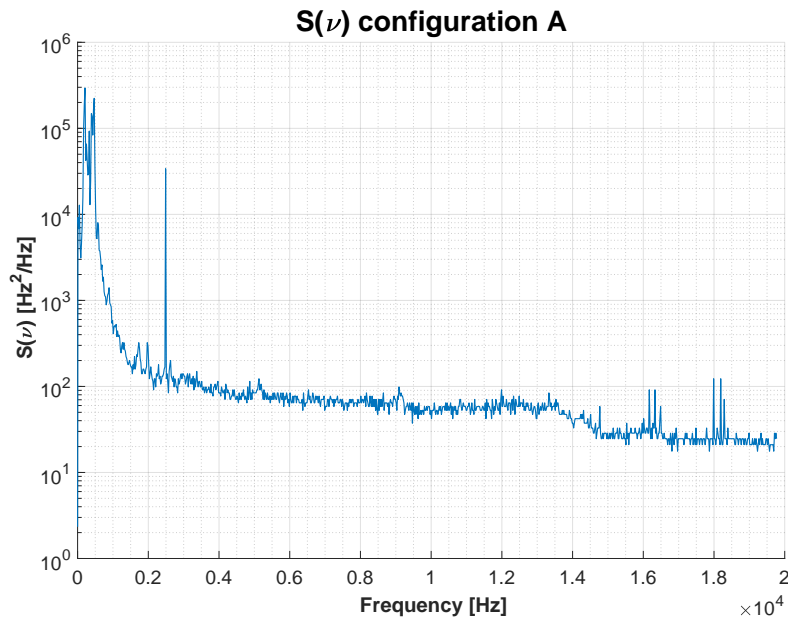
We stabilized the optical cavity in four steps, measuring the Power Spectral Density and calculating the global Gain function for each stage. In all measurements is present a probe artificial noise at 2.5 kHz. Firstly we used only the integrator with a high variable resistance value equal to $3k\Omega$ and we labeled this configuration *A*. In this condition the feedback gain is not enough to compensate the noise and low frequency noise can easily lead to the loss

of stabilization or to generate strong losses peaks on the transmitted power and then on the inside-cavity radiation power. PSD and the gain function of configuration *A* are shown in Figures 5.17a and 5.17b. In order to reduce the low-frequency noise, we increased the integrator gain setting the resistance to $0.65k\Omega$ (configuration *A**). High gain integrator help to reduce low frequency noise, but can spark off self-oscillations. The reason can be explained looking at Figure 5.18: at 1.1 kHz the gain amplitude is about unitary, while the phase is about 180 degrees, and in this situation Barkhausen criterion is satisfied. In case *A** experimental spectrum is not available because strong oscillations saturate the Offset Monitor and data acquisition becomes unreliable. To avoid self-oscillations, the low-pass filter can be inserted with a resistance value $R_{fil} = 6k\Omega$ and a cut frequency $f_c \approx 2.7$ kHz (feedback configuration *B*). The filter shifts $G \approx 1$ to lower frequencies and move the π phase away from it. Nevertheless, self-oscillations reduce but are not removed at all, as can be noted in Figures 5.19a and 5.19b. To suppress the noise peak growth around 3 kHz, the proportional is switched on. The use of proportional circuit allows us to improve the gain bandwidth reduced by the filter and to suppress self-oscillations. Low gain proportional, $R_{prop} = 40\Omega$ is enough for our purposes. The so obtained spectrum is exposed in Figures 5.20a and 5.20b. The achieved result can be explained by the global gain plot: the proportional raises the gain amplitude and shifts the dangerous 180 degrees phase of more than 4 kHz.

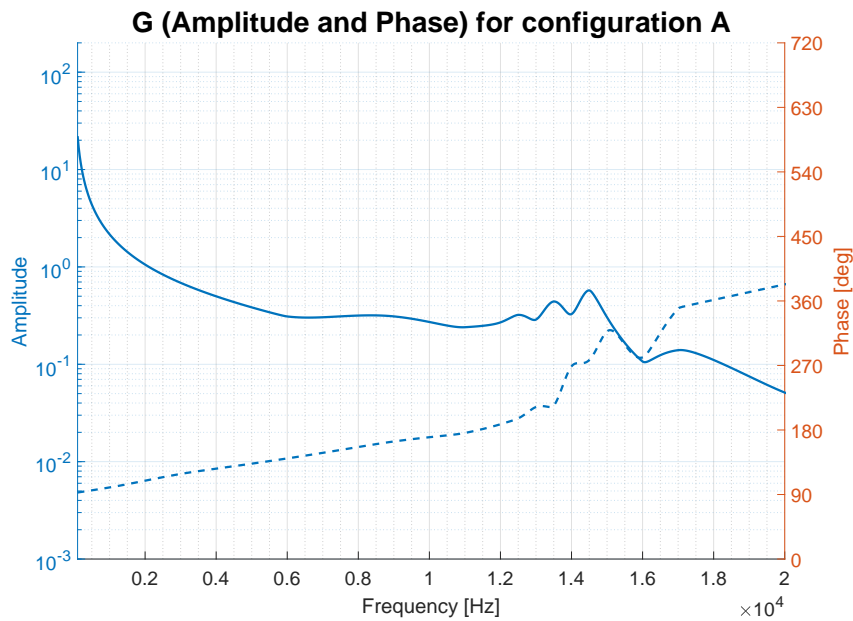
The noise σ has been also calculated in order to quantify the goodness of the stabilization procedure. In particular, we obtained $\sigma_A = 6251$ Hz for configuration *A*, which is reduced to $\sigma_B = 2934$ Hz in configuration *B*. The best stability result is reached by configuration *C*, where we have $\sigma_C = 2235$ Hz. Empirically the stabilization result is evident on the transmission signal detected by the photodetector positioned after the second mirror of the cavity: comparing the transmitted signal in configuration *A* in Figure 5.21 and in configuration *C* in Figure 5.22 we can note a more flat profile and an higher mean value.

5.3 Noise of stabilized cavity-laser system

After performing the active stabilization of the cavity, we measured the noise on the transmitted beam, calculating the Power Spectral Density of the signal sent on the photodetector. It is worth noting that measuring the transmitted radiation signal we have both intensity and frequency noise contribution associated to cavity-laser detuning and laser power fluctuations (Subection 4.2.2). It is also important to highlight that the cavity bandwidth is about 200 kHz and the photodetector cut frequency is about 900 kHz. We acquired experimental spectra stabilizing the cavity using feedback configuration *C* that guarantees the best stabilization performances. The result is shown in Figure 5.23. We also calculated the noise σ as an



(a)



(b)

Figure 5.17 (a): Spectrum in configuration A. We can observe a very high noise level at low-frequencies and a general decreasing behavior. The probe peak is well visible at 2.5 kHz. Low integrator gain does not allow a good stabilization, since does not well compensate fluctuations and disturbances. (b): $G(f)$ in configuration A. We can note that the Gain is high only at frequency lower than 2 kHz, while in other regions the noise is not suppressed, since the gain is too low. Moreover, we can observe that 180° phase is very far from $G(f) = 1$.

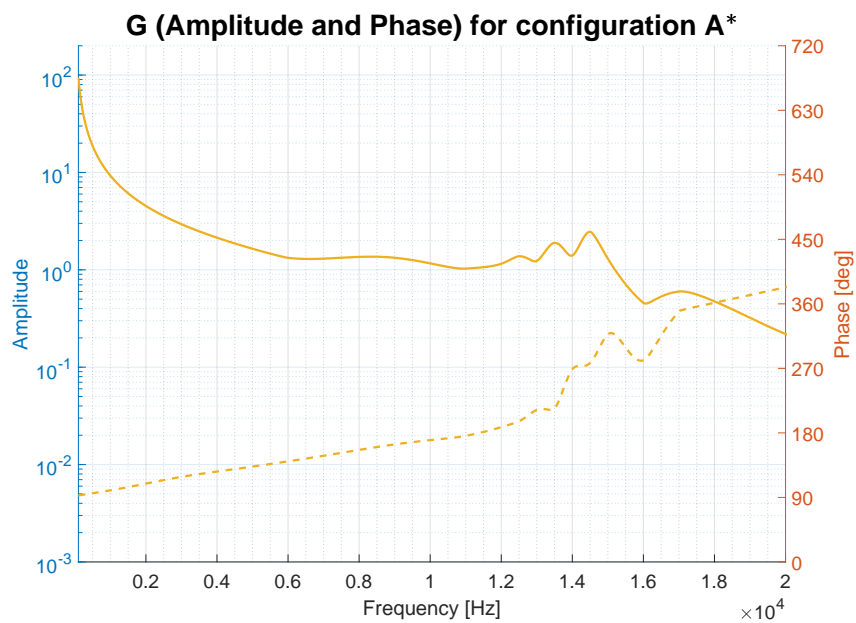
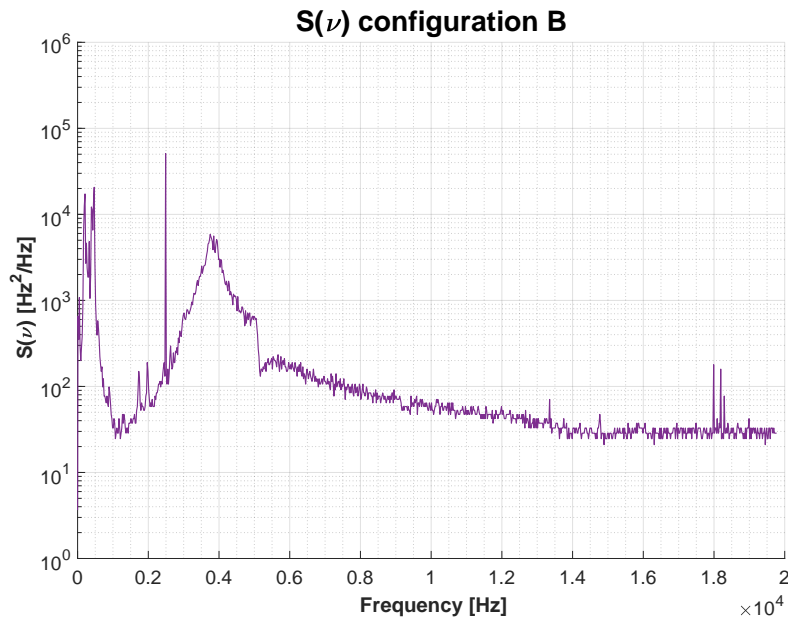
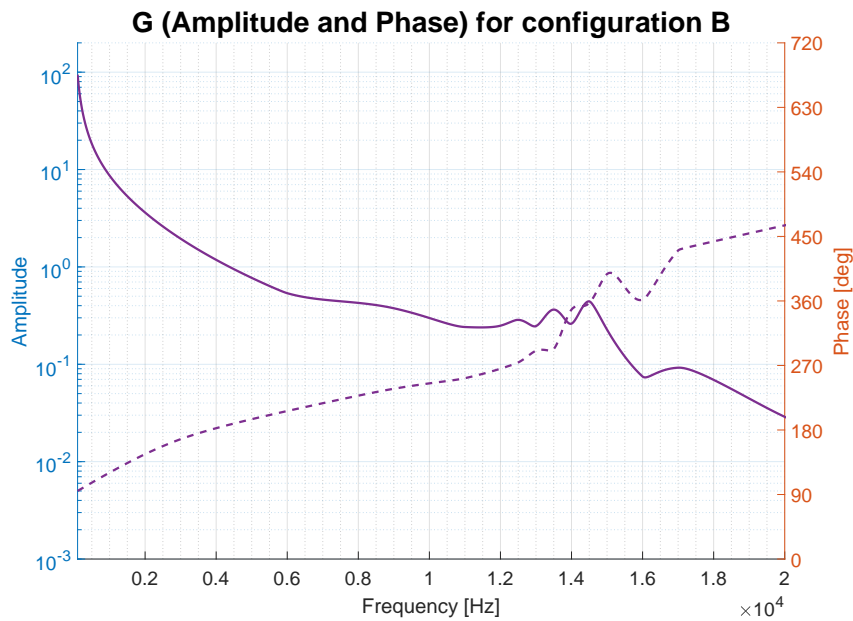


Figure 5.18 $G(f)$ in configuration A^* . In this configuration PSD is not measurable because the high self oscillation peak saturates the PDH error signal. From this graph we can easily understand why there are self-oscillations at a frequency approximately 11 kHz: here the Gain is approximately one and the phase is very close to 180° , then the system satisfies the Barkhausen criterion. By the way, we expect a better noise suppression at low frequency due to a higher integrator gain respect to configuration A.

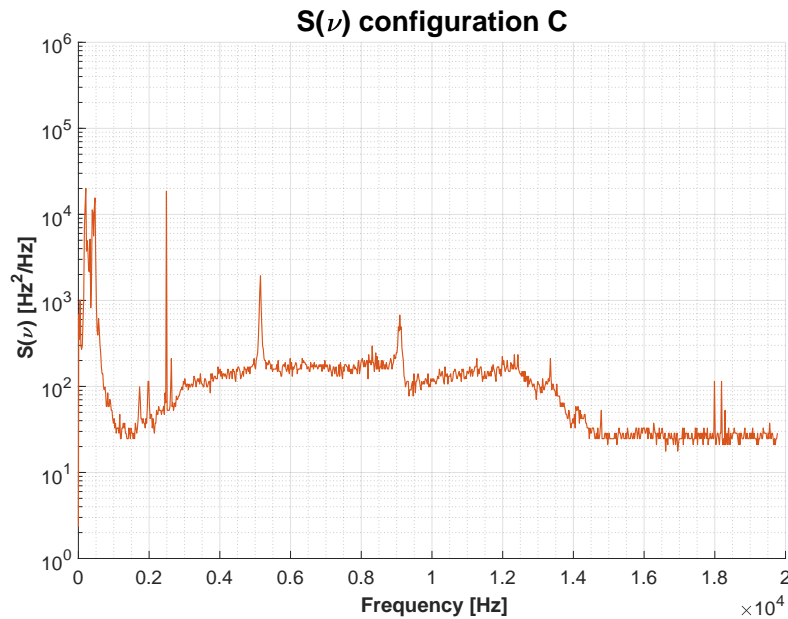


(a)

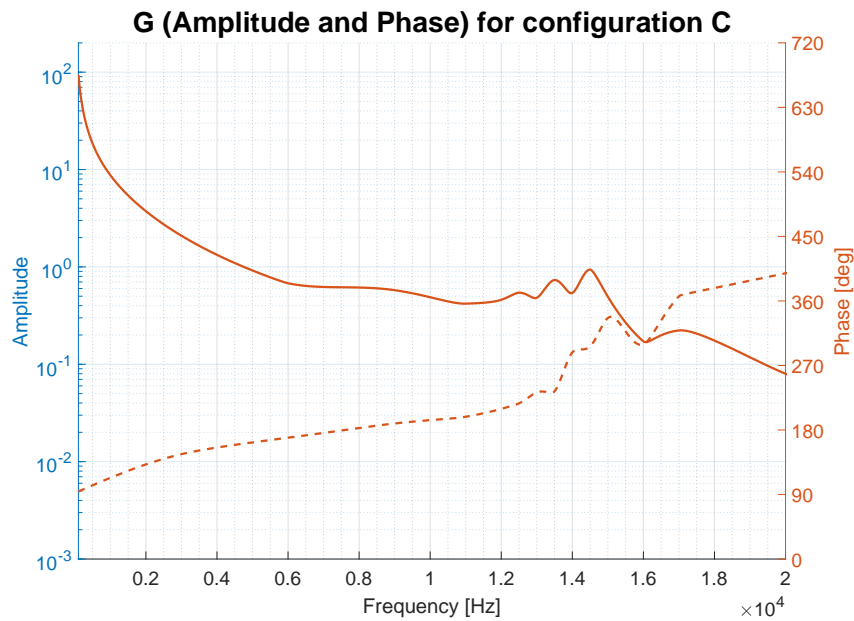


(b)

Figure 5.19 (a): Spectrum in configuration *B*. The presence of the low-pass filter reduces self-oscillations, but does not delete them at all. We can observe here that there is a big contribution to noise at frequencies about 4000 Hz due to self oscillations. We can also note that the low-frequency noise has been reduced of a factor 10 respect to configuration *A*, thanks to the higher integrator gain. (b): $G(f)$ in configuration *B*. Low-pass filter increases gain amplitude slope, reducing the control bandwidth. Furthermore, although the phase is not exactly 180° when the amplitude is equal to one, it is enough close to it in order to trigger self-oscillations. Self-oscillation frequency is lower than in case *A** because $G(f)$ becomes unitary near 4 kHz.



(a)



(b)

Figure 5.20 (a): Spectrum in configuration C. All self-oscillation peaks have been deleted inserting the proportional that guarantees an higher gain at frequencies higher than the kHz. In this configuration we reach the best results because we strongly suppress low-frequency noise with the integrator, we maintain an high gain up to some kHz thanks to the proportional and avoid self-oscillations exploiting the low-pass filter. (b): $G(f)$ in configuration C. We can immediately see that this configuration is quite far from the Barkhausen criterion conditions, then we have no self oscillations. On the other hand, the use of proportional and integrator circuits at the same time allows a good stability since the main noise contribution are in spectral region corresponding to high gain amplitude.

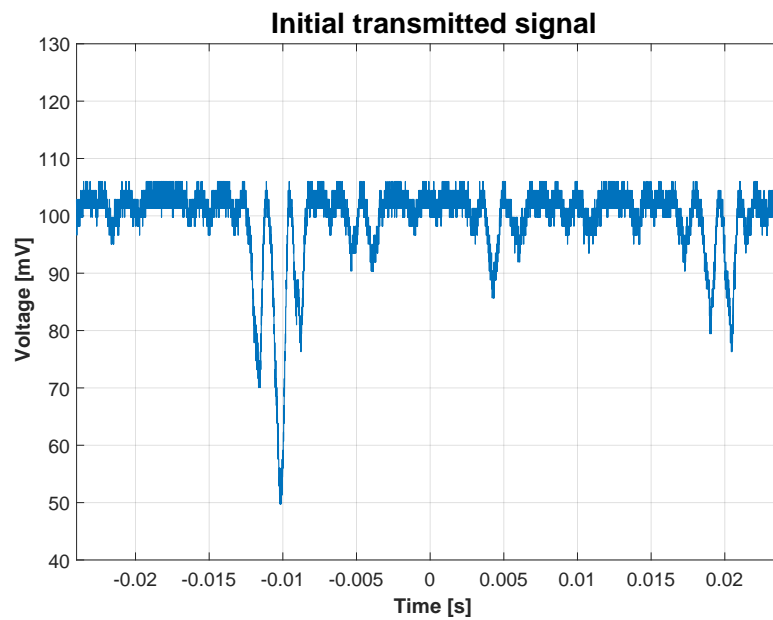


Figure 5.21 Transmitted signal in configuration A. The trace is noisy and many losses peaks are present.

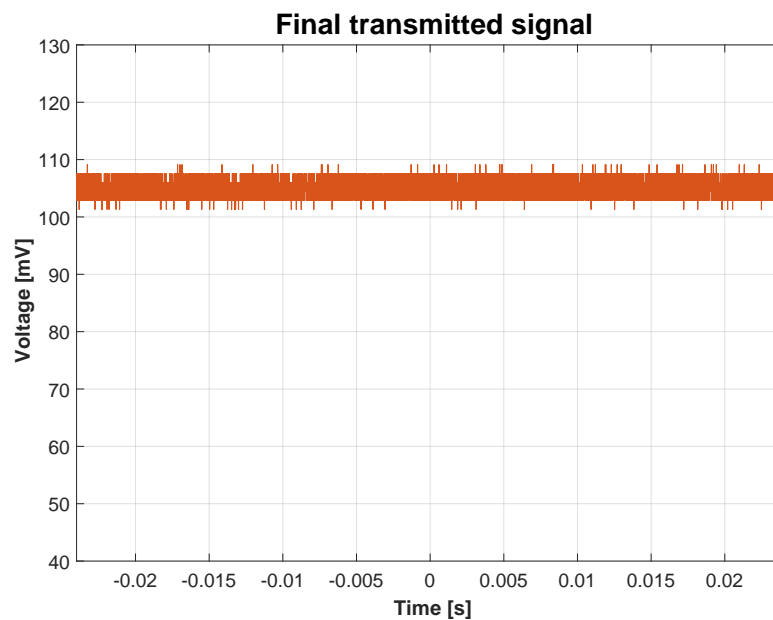


Figure 5.22 Transmitted signal in configuration C. Here the better situation obtained is presented. Noise is very low and the transmission trace is flat and without power downfalls.

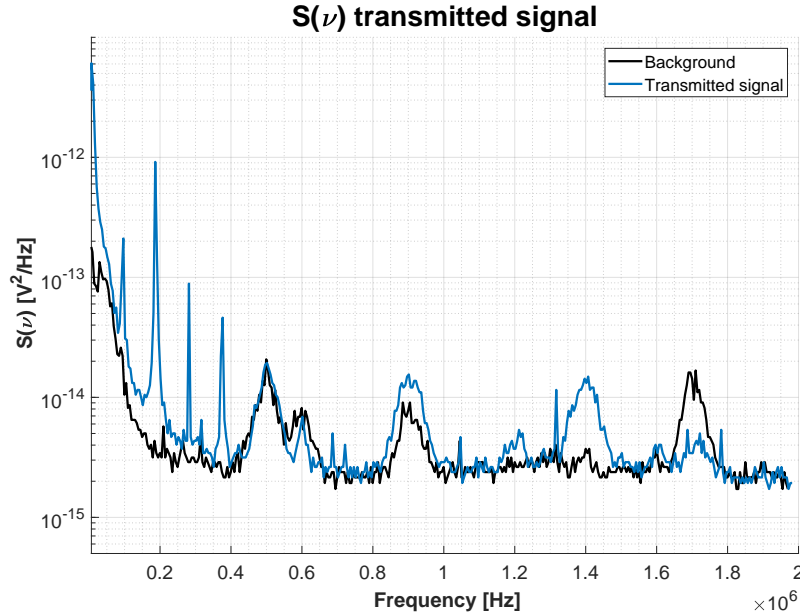


Figure 5.23 Power Spectral Density of the transmitted signal measured outside cavity mirror *B* while optical stabilization was active.

integral function of frequency, which is compared to the PSD in Figure 5.24. It is important to note that in these graphics the low-frequency noise peaks are not visible: this fact is due to the low resolution of the oscilloscope when wide range measures are performed. We can immediately note the same spikes of laser intensity noise, which directly influences the transmitted beam noise, while the signal goes to the background for high frequencies. We also calculated the σ of the transmitted beam considering the frequency range from 0 Hz to 2 MHz and so obtaining $\sigma_{tran} = 0.21$ mV. For a transmission peak about 115 mV we have a relative noise $\delta V = \frac{\sigma}{115 \text{ mV}} = 0.18\%$. The same percentage can be referred to the power inside the cavity, since it is directly proportional to the measured transmitted voltage ($P = \frac{V}{\eta R}$).

Evaluate noise over the transmitted signal is a key-point in order to make previsions on the next stages of MariX R&D. As an example, if we increase the cavity Finesse, can we already reach a good stability? To answer this questions, we calculated the power relative fluctuation assuming a Finesse of 5000. To do this, we converted σ_{tran} in Hz, supposing a Gaussian shape for the transmission peak of our cavity, so in in the case of $F \approx 500$. In Gaussian approximation we can write the transmission peak as a function of frequency

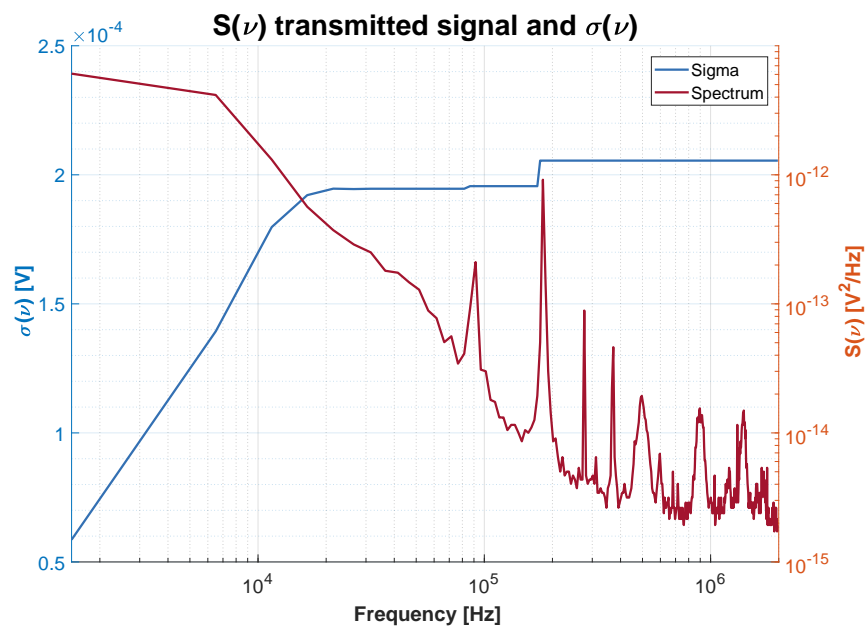


Figure 5.24 σ and Power Spectral Density as functions of frequency are here shown. We can easily note that the most of noise contributions are at low-frequency. In this plot we are not able to distinguish low-frequency peaks in power spectral density because of oscilloscope resolution. Also in σ plot we observe a linear behavior that we expect to become different at higher resolutions, thanks to the contribution of every single noise spike. Noise integral over 0 Hz-2 MHz frequency range gives relative power fluctuation about 0.18%.

detuning between cavity and laser:

$$G_{500}(\delta\nu) = 115 \text{ mV} \cdot e^{-\frac{\delta\nu^2}{2\Delta_{500}^2}} \quad (5.11)$$

Where $\Delta_{500} = \frac{HWHM}{1.177} = 8.496 \cdot 10^4 \text{ Hz}$, obtained starting from $HWHM = \frac{1}{2} \frac{FSR}{F} \approx 100 \text{ kHz}$. Following the Gaussian profile, we find that $\sigma_{500} \approx 5400 \text{ Hz}$ when the voltage has been lowered by a factor σ_{tran} subtracted to the maximum. If we now suppose to increase cavity Finesse up to 5000, we can calculate its transmission peak applying the same method we used above. Then the Gaussian function G_{5000} can be calculated from $\Delta_{5000} = \frac{\Delta_{500}}{10}$ instead of Δ_{500} :

$$G_{5000}(\delta\nu) = 115 \text{ mV} \cdot e^{-\frac{\delta\nu^2}{2\Delta_{5000}^2}} \quad (5.12)$$

We can exploit this Gaussian we can calculate the voltage fluctuation associated to a frequency noise of 6 kHz that we measured for our cavity. The result is $\sigma_{500} = 5.3 \text{ mV}$, which corresponds to a relative noise $\delta V_{5000} = 19\%$ on the average transmitted power. Since most of noise is found at frequencies between 0 Hz and 10 kHz (about 4/5 of the total), it is clear that it is fundamental reduce low-frequency noise in future. Indeed, if we suppose to remove all the low frequency noise, the relative power fluctuation reduces to $\delta \tilde{V}_{5000} = 2\%$, then it could be possible to stabilize a cavity with finesse ten times higher than the currently used maintaining the power over the 98% of its maximum.

5.4 Low frequency noise measurements

As can be realized from the considerations at the end of the previous section, low-frequency noise plays an important role in our system stabilization. Such noise is essentially due to mechanical vibrations of the components of the cavity, like mirror mounts and micrometric slides. Since the cavity studied in this work is the first realized for the MariX project, we used standard optical components unfortunately sensitive to mechanical vibrations. An important step for the cavity improvement during the R&D program is then individuate the most problematic elements with the objective of substitute them with more performant components. With such aim, we have studied the low-frequency noise from PDH signal, in a range between 0 Hz and 1 kHz. The low-frequency spectrum is presented in Figure 5.25. Three main peaks can be easily distinguished at 225 Hz, 410 Hz and 485 Hz. Lower peaks are also present at frequencies equal to 65 Hz, 365 Hz, 365 Hz and 450 Hz. We measured the resonance spectrum of all optical mounts from the Menlo source to the last mirror of the

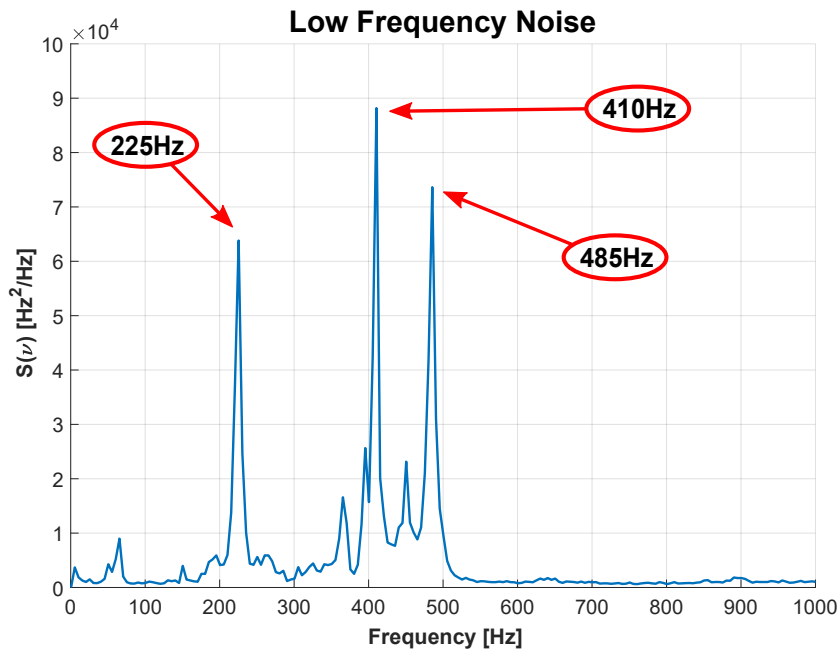
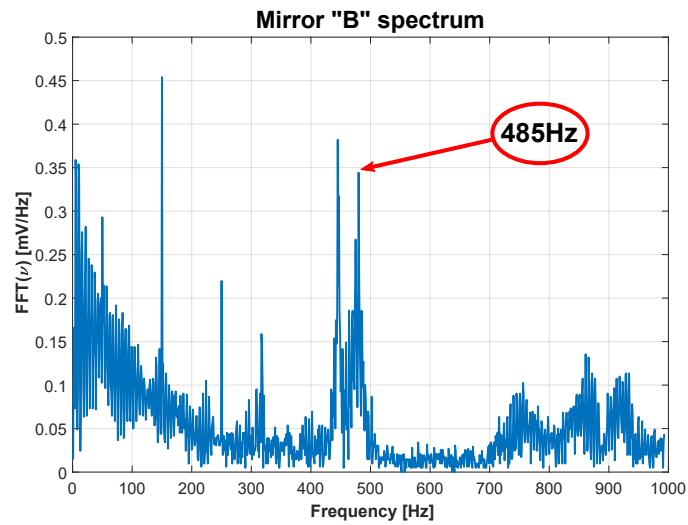
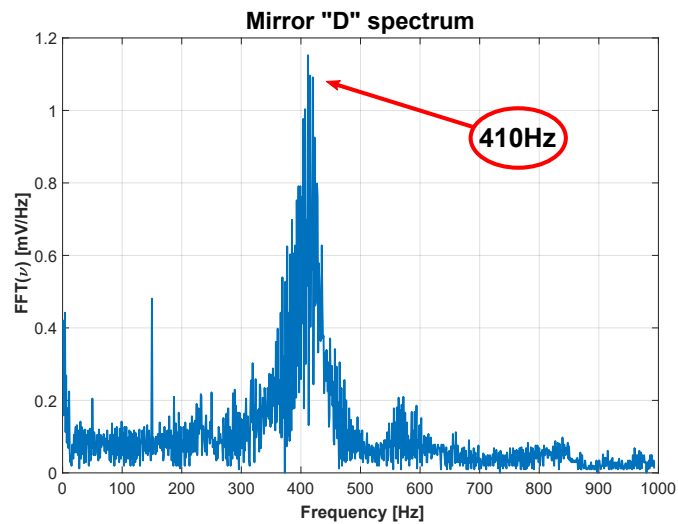
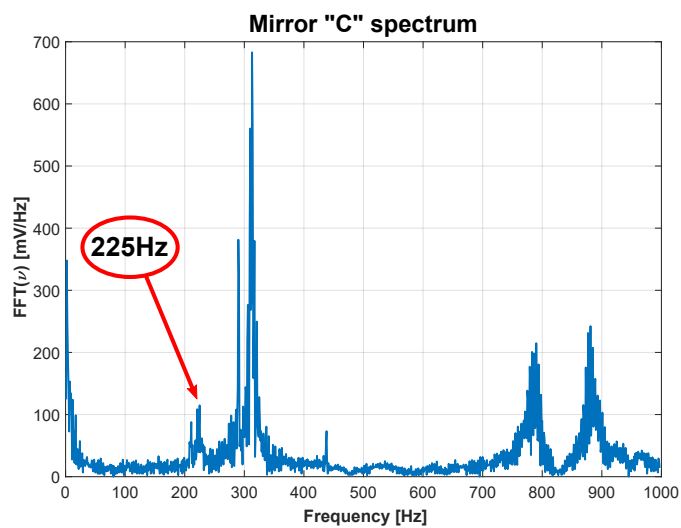


Figure 5.25 Low-frequency noise spectrum. The three main peaks are highlighted by red arrows.

optical cavity, exploiting an angular fluctuation measurator⁷. In practice, we delicately knock on the mounts and we acquired the FFT of the so caused horizontal angular fluctuation. Then the mounts Fourier spectrums have been compared with the error signal spectrum in Figure 5.25, looking for similar resonance peaks. Note that we simply used the FFT and not a PSD because we are not interested in peak height, but in their spectral position only. Recalling that in such spectrums the peak position in frequency is important, while their height is not, since it is correlated to many factors like the point in which the mount has been hit to make it vibrate or the direction of the bump; the 485 Hz noise peak can be attributable to the mount of cavity mirror *B*, the 410 Hz is due to the mount of cavity mirror *D*, while the 225 Hz noise peak is probably due to the mount of cavity mirror *C*. The measured Fourier transform of these components is shown in Figures 5.26a, 5.26b, and 5.26c respectively. It is then clear that the most important noise sources are components of the Fabry-Perot cavity. As next step in cavity stabilization is to increase its mechanical stability replacing both mirror and slides with high stability components.

⁷Details about the angular fluctuation measurator are not available, since Dott. Cialdi et al. hold the patent for this device.

(a) Angular fluctuation spectrum corresponding to the mount of mirror *B*.(b) Angular fluctuation spectrum corresponding to the mount of mirror *B*.(c) Angular fluctuation spectrum corresponding to the mount of mirror *B*.

Chapter 6

Conclusions

In this thesis work we have realized a bow-tie Fabry Perot optical resonator and we have actively stabilized it against an external mode-locking laser source, via Pound-Drever-Hall technique.

In order to reach our goal, we characterized the whole experimental setup, then the laser source, the optical cavity and the feedback-system. In particular, we studied spatial, temporal and spectral properties of the laser we used and also its intensity noise. For what concerns the optical cavity, we coupled it with the laser beam and we characterized its main features like the Finesse, the spot size and waist dimension in focus as a function of the curved mirror distance and the cavity modal structure. Then, we characterized all the feedback system components transfer functions. Furthermore, we developed a stabilization procedure to stabilize the cavity against the laser. With the aim of quantifying the experimental results we measured the Power Spectral Density of the PDH error signal and we calculated a Gain function able to explain the experimentally observed feedback behavior. We observed that integrator and proportional circuits in the PID are complementary and both necessary to have a good stabilization and noise suppression both at low frequency and in the kHz spectral region. Then we found that the best results are achieved by the choice of a high integrator gain, relatively low proportional gain in addition to a contribution give by the Servo low-pass filter. Such configuration is the best compromise between high gain (then strong noise suppression) and the prevention of self-oscillatory phenomena. Our stabilization method permits a stabilization with power fluctuations only on the order of 0.2% on the transmitted signal outgoing the cavity, then on the power inside the cavity.

Looking at the next steps of MariX R&D program, we also performed predictions on the stability of an analogue cavity with ten-times higher Finesse than the current one, since the final objective of MariX and BriXs demonstrator is to use an high-Finesse resonator. Because the main noise sources are mechanical vibrations that causes disturbance at low-

frequency, we have individuated the mounts responsible of the main noise peaks using a angular fluctuation measurator, in order to substitute them in future and so to increase system stability.

In conclusion, this work has allowed us to substantially solve the stability problem for MariX-BriXs optical cavity and to precisely individuate the strategies we need to apply in order to solve the current experimental problems, like improving mechanical stability. Meanwhile, the amplification system implementation began and we started studying a new method to solve the problems due to mode-mixing phenomena [10], that now represent the most important challenge in MariX cavity development.

Bibliography

- [1] L. Serafini et al. Marix conceptual design report, 2018.
- [2] W. Thomlinson et al. K-edge subtraction synchrotron X-ray imaging in bio-medical research. *Physica Medica* 49, 2018.
- [3] Advanced Photon Source APS 2016 science report, 2018.
- [4] Eric D. Black. An introduction to Pound–Drever–Hall laser frequency stabilization. *American Journal of Physics*, 69(1):79–87, 2001.
- [5] J. L. Hall. *Stabilizing Lasers for Applications in Quantum Optics*. 1986.
- [6] Frieder Lindenfelser. *Laser stabilisation for quantum information experiments with trapped ions*. Master thesis, Institut for Quantum Electronics ETH Zürich, 2011.
- [7] Evan Hall. Laser Frequency and Intensity Stabilization for Advanced LIGO. pages 1–4, 2016.
- [8] Donna Strickland and Gerard Mourou. Compression of amplified chirped optical pulses. *Optics Communications*, 55(6):447 – 449, 1985.
- [9] H. Carstens et al. Megawatt-scale average-power ultrashort pulses in an enhancement cavity. *Opt. Lett.*, 39(9):2595–2598, May 2014.
- [10] Julia Benedikter, Thomas Hümmer, Matthias Mader, Benedikt Schleder, Jakob Reichel, Theodor W. Hänsch, and David Hunger. Transverse-mode coupling and diffraction loss in tunable fabry-perot microcavities. *New Journal of Physics*, 2015.
- [11] P. Favier et al. The compact x-ray source thomx, 2017.
- [12] Gianluca Galzerano. Oscillators: frequency stability and noise analysis. In *Oscillators: frequency stability and noise analysis*, Trieste, 2016.
- [13] Rüdiger Paschotta. *Encyclopedia of Laser Physics and Technology*. John Wiley & Sons, 2008.
- [14] Orazio Svelto. *Principles of lasers*. Springer US, 2010.
- [15] B. Carter. *Op Amps for Everyone*. Elsevier Science, 2009.
- [16] P.R. Gray and R.G. Meyer. *Circuiti integrati analogici*. McGraw-Hill, 2nd edition, 1987.

-
- [17] Hans-A. Bachor and Timothy C. Ralph. *A Guide to Experiments in Quantum Optics*. Wiley-VCH, 2nd edition, 2004.
- [18] Trager. *Springer Handbook of Lasers and Optics*. Springer, 2012.
- [19] L.E. Nelson, D.J. Jones, K. Tamura, H.A. Haus, and E.P. Ippen. Ultrashort-pulse fiber ring lasers. *Applied Physics B*, 65(2):277–294, Aug 1997.
- [20] Paul Horowitz and Hill Winfield. *The Art of Electronics*. Cambridge University Press, 2nd edition, 1989.
- [21] Warwick Paul Bowen. *Experiments towards a Quantum Information Network with Squeezed Light and Entanglement*. PhD thesis, 2003.
- [22] Dana Z. Anderson. Alignment of resonant optical cavities. *Appl. Opt.*, 23(17):2944–2949, Sep 1984.
- [23] Hiroshi Sakai, Yousuke Honda, Noboru Sasao, Sakae Araki, Yasuo Higashi, Toshiyuki Okugi, Takashi Taniguchi, Junji Urakawa, and Mikio Takano. Performance studies of a laser wire beam profile monitor. *Japanese Journal of Applied Physics*, 41(11R):6398, 2002.

Ringraziamenti

Il termine di questo lavoro rappresenta anche la fine di un lungo percorso, per il quale sono diversi i grazie da scrivere.

Vorrei come prima cosa ringraziare il mio professore Simone, per avermi guidato per tutto il periodo della tesi e per avermi insegnato moltissimo. Grazie anche a Gianluca, per avermi ospitato nel suo laboratorio presso il Politecnico di Milano. Grazie ai miei compagni di laboratorio Edoardo, Dario e Sanae, per il clima bellissimo in cui abbiamo lavorato.

Voglio poi ringraziare i miei genitori, Elisa e i nonni, che hanno sempre e costantemente fatto il tifo per me e mi hanno sostenuto in modo incredibile. Grazie anche a Federica, per la sua presenza preziosa. Infine, grazie ai compagni di questi anni Davide, Luca e Gabriele: è stato un semplicemente un piacere.